EFFECT OF BF-BASED CONTENT ON PHASE FORMATION, MICROSTRUCTURE, ELECTRIC AND MAGNETIC PROPERTIES OF BNKLT, KNLNTS AND BCTZ FERROELECTRIC CERAMICS

PICHITTRA THAWONG

A Thesis Submitted to the Graduate School of Naresuan University
in Partial Fulfillment of the Requirements
for the Doctor of Philosophy in Applied Physics - (Type 1.1)
2022

EFFECT OF BF-BASED CONTENT ON PHASE FORMATION, MICROSTRUCTURE, ELECTRIC AND MAGNETIC PROPERTIES OF BNKLT, KNLNTS AND BCTZ FERROELECTRIC CERAMICS

PICHITTRA THAWONG

A Thesis Submitted to the Graduate School of Naresuan University
in Partial Fulfillment of the Requirements
for the Doctor of Philosophy in Applied Physics - (Type 1.1)
2022

Thesis entitled "Effect of BF-based content on phase formation, microstructure, electric and magnetic properties of BNKLT, KNLNTS and BCTZ ferroelectric ceramics"

By PICHITTRA THAWONG

has been approved by the Graduate School as partial fulfillment of the requirements for the Doctor of Philosophy in Applied Physics - (Type 1.1) of Naresuan University

Oral Defense Committee

..... Chair
(Associate Professor Orawan Ritthidech, Ph.D.)

..... Advisor
(Associate Professor Theerachai Bongkarn, Ph.D.)

..... Co Advisor
(Associate Professor Tawat Suriwong, Ph.D.)

..... Co Advisor
(Assistant Professor Sasipohn Prasertpalichat, Ph.D.)

..... External Examiner
(Assistant Professor Jaru Jutimoosik, Ph.D.)

Approved

.....
(Associate Professor Krongkarn Chootip, Ph.D.)
Dean of the Graduate School

Title	EFFECT OF BF-BASED CONTENT ON PHASE FORMATION, MICROSTRUCTURE, ELECTRIC AND MAGNETIC PROPERTIES OF BNKLT, KNLNTS AND BCTZ FERROELECTRIC CERAMICS
Author	PICHITTRA THAWONG
Advisor	Associate Professor Theerachai Bongkarn, Ph.D.
Co-Advisor	Associate Professor Tawat Suriwong, Ph.D. Assistant Professor Sasipohn Prasertpalichat, Ph.D.
Academic Paper	Ph.D. Dissertation in Applied Physics - (Type 1.1), Naresuan University, 2022
Keywords	Lead-free, Ferroelectric, Dielectric, Magnetic, Combustion technique

ABSTRACT

In this study, the effect of Bi_2FeCrO_6 and $Bi_{0.8}Ba_{0.2}FeO_3$ on phase formation, microstructure, electric and magnetic properties of BNKLT, KNLNTS and BCTZ ferroelectric ceramics synthesized by the solid-state combustion technique using glycine as fuel has been investigated.

Firstly, lead free solid solution $Bi_{0.5}(Na_{0.68}K_{0.22}Li_{0.10})_{0.5}TiO_3$-xmol%$Bi_2FeCrO_6$ (BNKLT-xBFCO), with x=0, 0.004, 0.007, 0.013 and 0.019, ceramics were calcined at 750^{o}C and sintered at 1150^{o}C for 2 h using the solid state combustion technique. The effect of the x content on the phase formation, microstructure, electric and magnetic properties of the produced ceramics were investgated. All samples exhibited a pure perovskite phase with the co-existence of rhombohedral and tetragonal phases. The doping of BFCO enhanced the density and dielectric properties of the BNKLT ceramics. The BNKLT-0.013BFCO ceramics showed the highest density (5.87 g/cm^3), excellent dielectric properties (ε_R~1390, tan δ_R~0.039, ε_m ~4986 and tan δ_m~0.075) and the highest piezoelectric constant (d_{33}~194 pC/N). The sample with x=0 showed diamagnetic behavior, while the samples with 0.004-0.019 content exhibited paramagnetic behavior with higher magnetization at higher x content.

Secondly, (1-x)$Bi_{0.5}(Na_{0.77}K_{0.20}Li_{0.03})_{0.5}TiO_3$-x$Bi_{0.8}Ba_{0.2}FeO_3$ ((1-x)BNKLT-

xBBF) ceramics with x=0-0.4 were synthesized by the solid state combustion technique. The X-ray diffraction pattern of the ceramics showed a pure perovskite structure with the co-existence between the rhombohedral and tetragonal phases. From the Rietveld refinement, we observed that the unit cell volume increased as x increased due to the replacement of Bi^{3+} and Ti^{4+} ions by Ba^{2+} and Fe^{3+} ions at A-site and B-sites, respectively. The average grain size and measured density increased with increasing x. The resistivity of (1-x)BNKLT-xBBF ceramics decreased with increasing x. At room temperature, the (1-x)BNKLT-xBBF ceramics with x=0.2-0.4 exhibited multiferroic behavior characterized by ferroelectric and ferromagnetic hysteresis loops. The highest relative density (95.48%), the highest dielectric constant and low dielectric loss at room temperature (ε_R=1746 and tan δ_R=0.0296), good ferroelectric properties (P_r=6.46 μC/cm^2 and E_c=11.84 kV/cm) and good ferromagnetic properties (M_r=0.002 emu/g and H_c=110 Oe) were obtained from the 0.8BNKLT-0.2BBF ceramic, indicating that this sample has potential for applications in lead free, room temperature multiferroic systems.

Thirdly, (1-x)[$(K_{0.44}Na_{0.52}Li_{0.04})(Nb_{0.84}Ta_{0.10}Sb_{0.06})O_3$]-x$Bi_{0.8}Ba_{0.2}FeO_3$ [(1-x)KNLNTS-xBBF] lead-free ceramics, with different x content, were prepared by the solid-state combustion technique. The effect of $Bi_{0.8}Ba_{0.2}FeO_3$ content on the phase formation, microstructure, electric and magnetic properties of KNLNTS ceramics were investigated. The KNLNTS ceramic exhibited co-existing orthorhombic and tetragonal phases. When x increased, the samples demonstrated an increased tetragonal phase and unit cell volume. The average grain size, density and relative density deceased when x increased up to 0.06 and then continuously increased. For x=0, a well saturated P-E loop was found which the P_r and E_c values were about 21.27 μC/cm^2 and 12.38 kV/cm, respectively. While, x=0.02-0.2 exhibited round P-E loop because the leakage current were performed. For higher x, the leakage current of the samples decreased, suggesting that the samples exhibiting slim P-E loops. The KNLNTS ceramic exhibited diamagnetic behavior while the x=0.02-0.4 samples showed ferromagnetic behavior. At room temperature, multiferroic behavior, which exhibited fair ferroelectric and ferromagnetic hysteresis loops, were obtained from the samples with x=0.3-0.4 which means these ceramics can be applied in multifunctional

devices.

Finally, lead free (1-x)$Ba_{0.85}Ca_{0.15}Ti_{0.90}Zr_{0.10}O_3$-x$Bi_{0.80}Ba_{0.20}FeO_3$ [(1-x)BCTZ-xBBF] ceramics, with BBF content (x) between 0-0.4 [0, 0.02, 0.06, 0.1, 0.2, 0.3, 0.4], were prepared via the solid-state combustion technique. The effect of BBF content on the phase formation, microstructure, electric and magnetic properties of BCTZ was studied. From the Rietveld refinement analysis, the BCTZ ceramic showed co-existing orthorhombic and tetragonal phases, with a ratio of 35.4:64.6 and the percentage of the tetragonal phase continuously increased when x increased from 0.02 to 0.1, and became purely tetragonal at $x \geq 0.2$. When x increased, the average grain size, density and relative density continuously decreased while the unit cell volume enlarged. The dielectric constant at room temperature (ε_R) tended to decrease while the dielectric loss at room temperature (tan δ_R) increased with increased BBF content. For x=0, a pure BCTZ ceramic, a well saturated P-E loop was observed with a polarization (P_r) and coercive field (E_c) of 8.94 $\mu C/cm^2$ and 4.06 kV/cm, respectively. The ferroelectricity drastically decreased with x=0.02. For $x \geq 0.06$, the leakage current increased, which suppressed the ferroelectricity. With no BBF content (x=0) the ceramic had diamagnetic properties, that changed to paramagnetic properties with x=0.02-0.06 and finally to ferromagnetic properties when the BBF increased between 0.10-0.40. For x=0.10-0.40, the remnant magnetization (M_r) continuously increased.

In summary, the factor of chemical composition, phase formation, microstructure, and electrical property of each system are important to the induce magnetic property. The optimum composition of BNKLT-0.013BFCO, BNKLT-0.2BBF, KNLNTS-0.3BBF and BCTZ-0.1BBF ceramics were observed which is effective way to improve the properties of these ceramics for various applications such as reading/writing with magnetization, spintronic, energy harvesting or sensors.

ACKNOWLEDGEMENTS

I would like to express the deepest gratitude to my advisor, Associate Professor Theerachai Bongkarn, Ph.D, and co-advisor Assistant Professor Sasipohn Prasertpalichat, Ph.D. and Associate Professor Tawat Suriwong, Ph.D, for his initial idea, guidance, and encouragement which enable me to carry out my study successfully. I consider it as a great opportunity to do my doctoral program under his advice and to learn from his research expertise.

My sincere gratitude also goes to my thesis committee, Associate Professor Orawan Ritthidech, Ph.D, and Assistant Professor Jaru Jutimoosik, Ph.D. for their helpful advice, comments and suggestions.

My profound thanks to Department of Physics, Faculty of Science, Naresuan University for being warmest places to study since the researcher studied a Bachelor's degree and Doctoral degree here. I feel love and commitment with here. I would like to thank Science Lab Center and Miss Thanita Sutthatang for XRD analysis, Mr. Seangphet Boonpang and Miss Prakaithip Kitikhun for from SEM analysis for their assistance in the part of instrument.

I would like to acknowledge the Science Achievement Scholarships of Thailand (SAST) Ph.D. Program to Miss Pichittra Thawong all financial support during this study.

Finally, I would like to thank my family for their love and their understanding. They have been constantly providing me with encouragement, enjoyment during my life and enabled me to complete this thesis.

PICHITTRA THAWONG

TABLE OF CONTENTS

Page

LIST OF TABLES

Page

LIST OF FIGURES

Page

CHAPTER I

INTRODUCTION

Overview

Lead-based ferroelectric ceramics have been widely used in electronic devices such sensors, transducers, actuator and capacitors because of their excellent electrical properties (1-3). However, the evaporation of lead oxide during the sintering process brings serious environment harm. Therefore, it is necessary to studied develop lead-free ferroelectric ceramics such as $Bi_{0.5}Na_{0.5}TiO_3$ (BNT), $K_{0.5}Na_{0.5}NbO_3$ (KNN) and $BaTiO_3$ (BT) that are capable of replacing lead-based ceramics.

BNT ceramics is a one of kind lead-free ferroelectric ceramics which is discovered by Smolenski et al. (4) in 1960. It has high Curie temperature (T_C=320^{o}C) and high remnant polarization (P_r=32 μC/cm^2). However, it is well known that BNT ceramics have a limited practical usage due to its large coercive field (E_c=73 kV/cm), poor piezoelectric constant (d_{33}=64 pC/N) and high conductivity (5-7). To improve the electrical properties of BNT ceramics, some elements are substituted to prepare new solid solutions. R. Sumang et. al (8) substituted K^+ and Li^+ ions for Na^+ ions in BNT ceramics by the solid-state combustion technique. They reported coexisting rhombohedral and tetragonal phases, a high Curie temperature (T_C=313^{o}C) and excellent electrical properties (ε_m=4000, P_r=16.6 μC/cm^2, E_c=18.8 kV/cm and d_{33}=159 pC/N) obtained from $Bi_{0.5}(Na_{0.77}K_{0.20}Li_{0.03})_{0.5}TiO_3$ (BNKLT) ceramics.

In case of potassium sodium niobate ($K_{0.5}Na_{0.5}NbO_3$; KNN), having polymorphic phase boundary (MPB) at room temperature, has been reported to be the most promising candidates due to their high Curie temperature (9, 10). However, it has also been found that KNN ceramics exhibit poor density leading to low electrical properties. Because of the evaporations of Na_2O and K_2O of KNN-based ceramics at high temperature using conventional sintering process several techniques to improve the densification of KNN-based ceramics, such as the construction of phase boundary, ion substitution, new preparation techniques, and sintering aids are performed (9-12). Recently, K. Martmool et al. (12) prepared new solid solution of

$(K_{0.44}Na_{0.52}Li_{0.04})(Nb_{0.84}Ta_{0.10}Sb_{0.06})O_3$ (KNLNTS) via the solid-state combustion technique. They reported that the dense KNLNTS ceramic exhibits a high Curie temperature (T_C=265^{o}C), high dielectric constant at room temperature and T_C (ε_R=1042 and ε_C=6114) and good ferroelectric properties (P_r=22 μC/cm^2 and E_c=12.5 kV/cm). Moreover, it was found that this technique shows better sintering characteristics when compared with the conventional sintering process.

BT ceramics has gained more attention from many researchers because it has high dielectric constant. However, the disadvantage of BT ceramic is a low Curie temperature (T_C=120^{o}C) and low dielectric constant at room temperature (ε_r~2500)(13, 14). Therefore, the development of BT ceramics properties has attracted considerable attention in recent years. . The most popular method used to do this is the substitution of the isovalent Ca^{2+} at A-sites and Zr^{4+} at B-sites to create $(Ba_{0.85}Ca_{0.15})(Ti_{0.90}Zr_{0.10})O_3$ (BCTZ) ceramics, which has a morphotropic phase boundary (MPB) composition. W. Lui et. al (15) prepared BCTZ solid solutions by the solid-state reaction method and reported a high ramnant polarization (P_r ~14 μC/cm^2), low coercive field (E_c ~0.2 kV/cm), high permittivity (ε_R ~3000) and high piezoelectric coefficient (d_{33} ~600 pC/N). After that, C. Konphom et. al (16) studied the effect of the firring temperature on BCTZ ceramics prepared by the solid-state combustion technique. They reported that the solid-state combustion technique reduced the calcined temperature by 300^{o}C when compare with the solid-state reaction method. The reduction in the calcined temperature may be caused from the acceleration of the chemical reaction by the combustion energy of glycine, and the liquid phase formed by the melting of glycine during the calcined process. The ceramic showed a high ε_R>4485, ε_C>14897 and P_r ~18.47 μC/cm^2.

Nowadays, multiferroic material has attracted much attention because its exhibited ferroelectric and ferromagnetic orders; they can be both magnetized and electrically polarized (17-20). These properties make it a potential application in multifunctional material such as four-stage logic memory devices, magnetoelectric random access memory (MeRAM), magnetic field sensors, energy harvester, magnetoelectric resonator and read head. $BiFeO_3$ (BF) is one of the multiferroic material which it has more attention from many researchers. Because it possesses high Curie temperature (T_C) of about 820-850^{o}C and exhibits the co-existence of G-type

antiferroic magnetic (AFM) structure. However, a dense ceramic for BF is difficult to obtain by sintering process. Moreover, high leakage current, low spontaneous polarization and weak magnetism at room temperature are always obtained (20-23). In order to eliminate the disadvantages of BF ceramics, the doping of different ions in A-site or/and B-site is the best way due to its led to change of structure, electric and magnetic properties (24-28). For example, $Bi_{0.8}Ba_{0.2}FeO_3$ (BBF) ceramic exhibit the coexist between rhombohedral and tetragonal phases, high dielectric constant and the lowest dielectric loss at room temperature (ε_R=60 and tan δ_R=0.05 at f=100 MHz), and good magnetic properties (M_r~0.699 emu/g and H_c~5.16 kOe), reported by Chou Yang et al. (27). In addition, Bi_2FeCrO_6 (BFCO) is multiferroic material with a ferroelectric polarization of 80 $\mu C/cm^2$ and a magnetization of 160 emu/cm^3 at 110 K which was predicted from theoretical calculations (28). Riad Nechache et al. (28) reported the preparation of the BFCO thin films which demonstrated the very small saturation magnetization (5-6 emu/cm^3).

The formation of binary solid solutions of BF with other perovskite compounds such as $Bi_{0.5}Na_{0.5}TiO_3$ (BNT) and $BaTiO_3$ (BT) has been reported to be an effective way to enhance the magnetoelectric properties (27, 29-31). K. H. Ryu et al (29) studied the ceramics of the binary system (1-x)BNT-xBF with x=0-0.20 and found that all samples had a perovskite structure with no secondary phase. The ferroelectric phase transition temperature (T_C or T_m) increased from 322°C to 396°C when the x content increased. The 0.8BNT-0.2BF ceramic exhibited an ε_R ~500 and ε_m~1900 at 100 kHz. Next, Yongxing Wei et al. (30) fabricated 0.35BT-0.65BF ceramics via the conventional solid-state reaction method. They reported that the sample showed pseudo-cubic symmetry, P_r=30.6 $\mu C/cm^2$, E_c=27.9 kV/cm, M_r=0.07 emu/g and H_c=2.4 kOe. Meanwhile, Jing Yi et al. (31) prepared the (1-x)$(Ba_{0.85}Ca_{0.15})(Zr_{0.10}Ti_{0.90})O_3$-x$BiFeO_3$ ceramics with x=0.05-0.95 via the solid state reaction method, and found that the optimal ferroelectric and ferromagnetic properties were observed from $0.30 \leq x \leq 0.35$ which the P_r and M_r values were about 22.7-27.3 $\mu C/cm^2$ and 0.0394-0.0744 emu/g, respectively. After that, In previous work, Kavita Kaswan et al. (32, 33) prepared the (1-x)$Bi_{0.5}Na_{0.5}TiO_3$-x$Bi_{0.8}Ba_{0.2}FeO_3$ [(1-x)BNT-xBBF] with $0 \leq x \leq 0.80$ ceramics by conventional solid state reaction method. All the

obtained ceramics exhibited rhombohedral structure. This result showed the adding of BBF can produced the multiferroic material which remnant magnetization (M_r) and coercive field (H_c) increased with x increase. 0.8BNT-0.2BBF showed good magnetic properties (M_r~0.0077 emu/g and H_c~354.51 Oe). From literature review, it was found that the addition of multiferroic materials to ferroelectric ceramics is an effective method for increasing the densification and the magnetization in ferroelectric perovskite ceramics. Moreover, it is extremely important and challenging to find the optimum content between ferroelectric ceramic (BNT, KNN and BT) and multiferroic (BFCO and BBF) solid solution. Therefore, in this article we reported the effect of BFCO and BBF in BNKLT, KNLNTS and BCTZ ceramics on phase structure, microstructure, electric and magnetic properties synthesized by the solid-state combustion technique.

Objectives of this research

The objectives of this research are as follow:

1. To study the preparation of (1-x)BNKLT-xBFCO with x=0-0.019, (1-x)BNKLT-xBBF, (1-x)KNLNTS-xBBF and (1-x)BCTZ-xBBF ceramics with x=0-0.4 using the combustion technique.

2. To investigate the effect of BFCO and BBF contents on the crystal structure, microstructure, electric and magnetic properties of BNKLT, KNLNTS and BCTS ceramics for combustion preparation.

3. To inspect the correlation between phase structure, microstructure, electrical and magnetic properties of (1-x)BNKLT-xBFCO, (1-x)BNKLT-xBBF, (1-x)KNLNTS-xBBF and (1-x)BCTZ-xBBF ceramics with x=0-0.4.

4. To obtain the optimum x for multiferroic properties of BNKLT, KNLNTS and BCTZ ceramics.

Expectation outputs of this study

1. To comprehend the preparation of (1-x)BNKLT-xBFCO with x=0-0.019, (1-x)BNKLT-xBBF, (1-x)KNLNTS-xBBF and (1-x)BCTZ-xBBF ceramics with x=0-0.4 using the solid-state combustion technique.

2. To comprehend the effect of BFCO and BBF contents on the crystal structure, microstructure, electric and magnetic properties of BNKLT, KNLNTS and BCTS ceramics.

3. To comprehend the correlation between phase structure, microstructure, electrical and magnetic properties of (1-x)BNKLT-xBFCO with x=0-0.019, (1-x)BNKLT-xBBF, (1-x)KNLNTS-xBBF and (1-x)BCTZ-xBBF ceramics with x=0-0.4.

Research scope

1. The (1-x)BNKLT-xBFCO powder and ceramics were prepared by the solid-state combustion method. All samples were calcined at 750^{o}C and sintered at 1150^{o}C for 2 h.

2. The (1-x)BNKLT-xBBF powder and ceramics were prepared by the solid-state combustion method. All samples were calcined at 750^{o}C and sintered at 1025^{o}C for 2 h.

3. The (1-x)KNLNTS-xBBF powder and ceramics were prepared by the solid-state combustion method. All samples were calcined at 650^{o}C and sintered at 1100^{o}C for 2 h.

4. The (1-x)BCTZ-xBBF powder and ceramics were prepared by the solid-state combustion method. All samples were calcined at 1050^{o}C and sintered at 1450^{o}C for 2 h.

5. Inspection of the densification by Archimedes method, phase formation by X-ray diffraction (XRD) and Rietveld refinement method, morphology by scanning electron microscopy (SEM), average grain size by linear intercept method, dielectric properties by an inductance capacitance resistance (LCR) meter, ferroelectric hysteresis (P-E) loops by a computer controlled modified Sawyer-Tower circuit and

ferromagnetic by using a vibrating sample magnetometer (Versa Lab, Quantum Design) at room temperature (25^{o}C).

CHAPTER II

RELATED THEORY AND LITERATURE REVIEW

Fundamental theory

Dielectrics

Dielectrics are electrically insulating materials which a large gap. When they are placed in an electric field can be induced the polarization which characterized by the relationship between the applied electric field E, electrical polarization P and dielectric displacement D. In many materials, the polarization is proportional to the electric field; we can write

$$P = \chi \varepsilon_0 E \tag{1}$$

where ε_0 is the permittivity of vacuum, and χ is the dielectric susceptibility. In case of an isotropic, the relationship of relative permittivity (ε_r) is defined by

$$\varepsilon_r = \frac{(\varepsilon_0 E + P)}{\varepsilon_o E} = 1 - \chi \tag{2}$$

where $D = \varepsilon_0 E + P$ is the dielectric displacement (34, 35).

When consider in case of time dependent on electric field, frequency dependent phase shift between the field and the charge displacement arise from moving charges. Relative dielectric permittivity defined by the complex function,

$$\varepsilon_r(\omega) = \varepsilon^*(\omega) = \varepsilon'(\omega) - i\varepsilon''(\omega) \tag{3}$$

Where ε' and ε'' are the real and imaginary part of dielectric constant, respectively. The total polarization of dielectric in material is caused from five mechanism, as follows (34, 35):

- Electronic polarization is depending on the negatively charged electron shell against the positively charged nucleus in the displacement.
- Ionic polarization in ionic material because the displacement of the positive and negative sub lattices under an applied electric field.

- Orientation polarization is caused from alignment of the permanent dipoles under the electric field.
- Space charge polarization is performed in dielectric which showing spatial heterogeneities of charge carrier densities.
- Domain wall polarization is related to the only ferroelectric which arise from the movement of boundary.

The mechanism of electronic and ionic polarization are lattice contributions. Whereas, the result of orientation polarization, space charge and domain wall polarization are not caused by the lattice contributions. Moreover, the origin of each contribution cause from the response to applied electric field of a short-range movement of charges on different time scale. So, the Fourier transformation of this behavior must be transformed in different frequency. The characteristic dispersion of dielectric function of the real and imaginary part is shown in Figure 1.

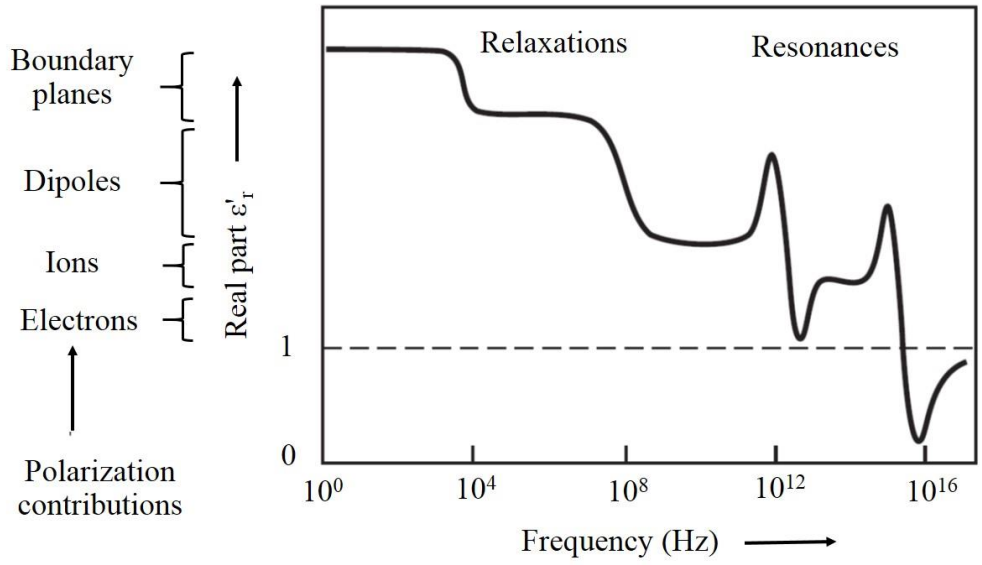

Figure 1 Frequency dependence of the real part of dielectric function (34)

Classification of dielectric

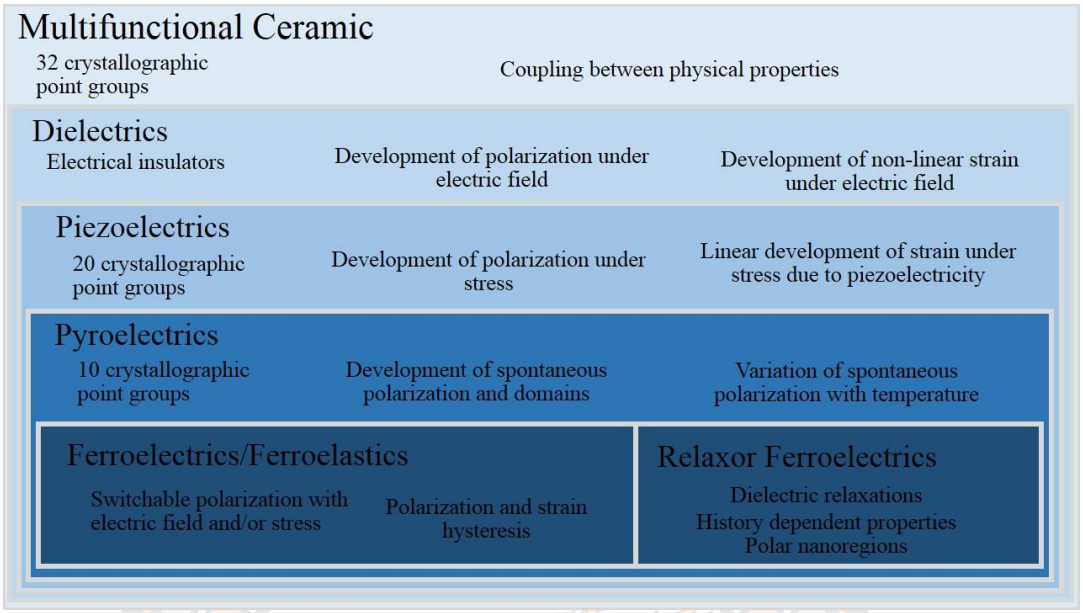

Figure 2 A classification of multifunctional ceramics indicating the subclasses of dielectric material (36)

The crystal class of 32 point groups can be classified into (a) 11 classes are centrosymmetric (cannot exhibit polar properties) and (b) 21 classes are noncentrosymmetric (can show one or more polar exist). Among these 21 classes, only 20 classes are piezoelectric and the one exception are being cubic class. From them, only 10 class have polar axis and can display a spontaneous polarization which are known as pyroelectric. Ferroelectric is a subgroup of the spontaneous polarized pyroelectric which the spontaneous polarized can be reversed by the external electric field. In the ferroelectric material, the perovskite structure is the most extensively studied and used for the electronic devices, namely cubic, tetragonal, orthorhombic, rhombohedral, hexagonal, monoclinic and triclinic. Table 1 introduced the geometric or crystal system which consist of the seven systems. Moreover, the lattice parameter and the unit cell volume are listed in Table 1.

Table 1 Geometrical characteristics of the seven crystal systems

System	Axial lengths	Angles	Unit cell volume
cubic	a=b=c	$\alpha = \beta = \gamma = 90^o$	a^3
tetragonal	a=b≠ c	$\alpha = \beta = \gamma = 90^o$	a^2c
orthorhombic	a≠ b ≠ c	$\alpha = \beta = \gamma = 90^o$	abc
Rhombo-hedral	a=b=c	$\alpha = \beta = \gamma \neq 90^o$	$0.866\ a^2c$
hexagonal	a=b≠ c	$\alpha = \beta = 90^o$, $\gamma = 120^o$	$a^3\sqrt{1-3\cos^2\alpha+2\cos^3\alpha}$
Monocle-nic	a≠ b ≠ c	$\alpha = \gamma = 90^o$, $\beta \neq 90^o$	$ab\sin\beta$
triclinic	a≠ b ≠ c	$\alpha \neq \beta \neq \gamma$	$abc\sqrt{1-\cos^2\alpha-\cos^2\beta-\cos^2\gamma+2\cos\alpha\cos\alpha\cos\gamma}$

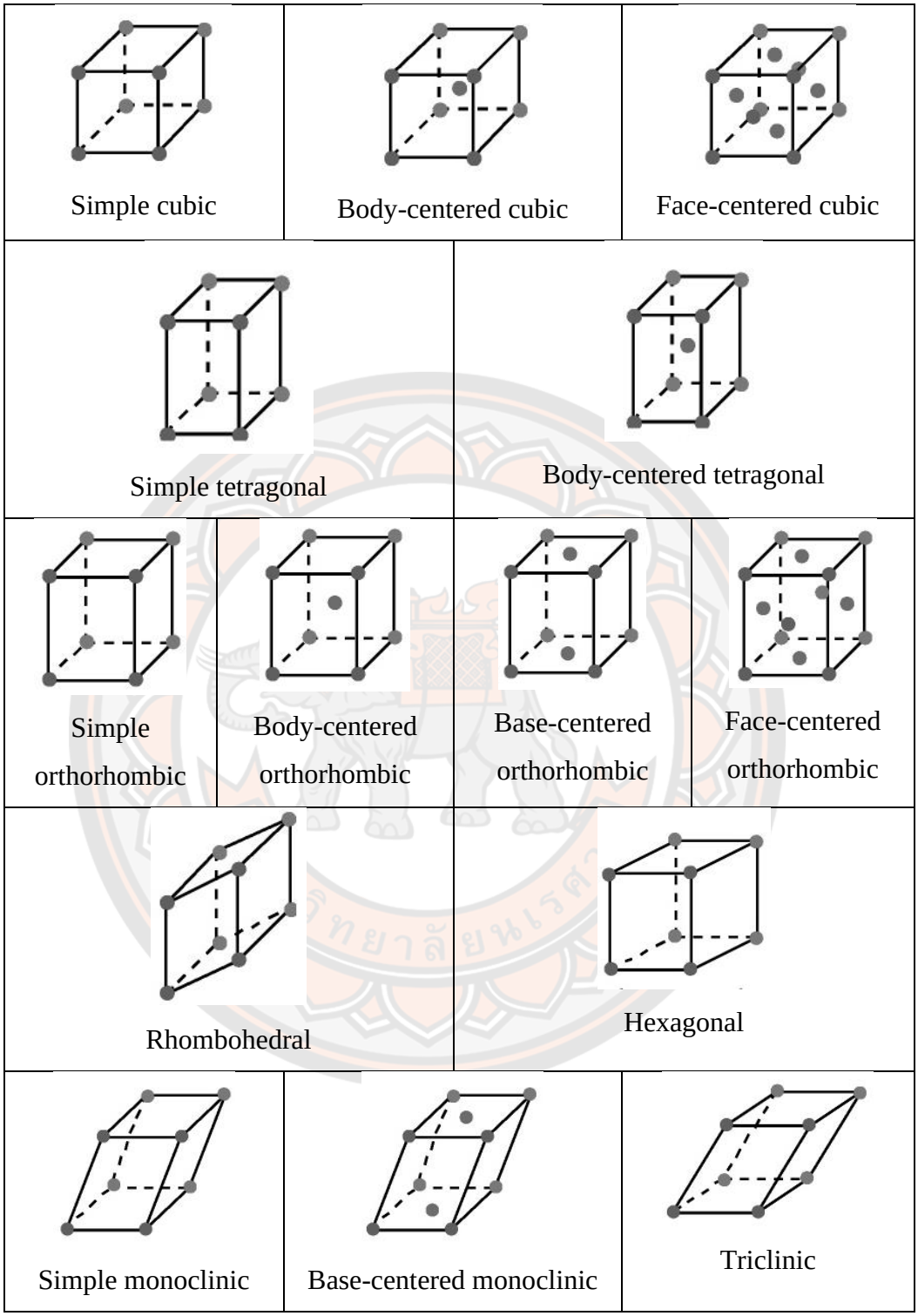

Figure 3 The 14 Bravais Lattices

Ferroelectricity (37, 38)

The ferroelectricity was discovered in the single crystal Rochelle salt in 1921 by Valasek (38) which this material exhibits ferroelectric properties such as spontaneous polarization on cooling below the Curie point and electric dipoles exist in structure even in the absence of electric field. In 1940s, the polycrystalline ceramics (barium titanate, $BaTiO_3$) was discovered and continuously studied for replacing the Pb-based material of industrial and commercial applications. Ferroelectrics are a type of materials with a permanent polar axis which this polarization can be aligned by an applied external electric field. The characteristic of first order phase transition are descripted about the discontinuous changes in physics properties. For example, the evolution of enthalpy is related to latent heat of the transformation which lead to thermal hysteresis in functional properties during phase transformation. Second order phase transitions are explained about the continuous change of enthalpy which is no latent heat of transformation. Both of first and second order phase transition can be improved the order-disorder or displacive. The formation of ferroelectric behavior must be depended on the temperature variation of dielectric constant of Curie temperature which is presented in Figure 4 for a first order phase transition (black) and a second order phase transition (red).

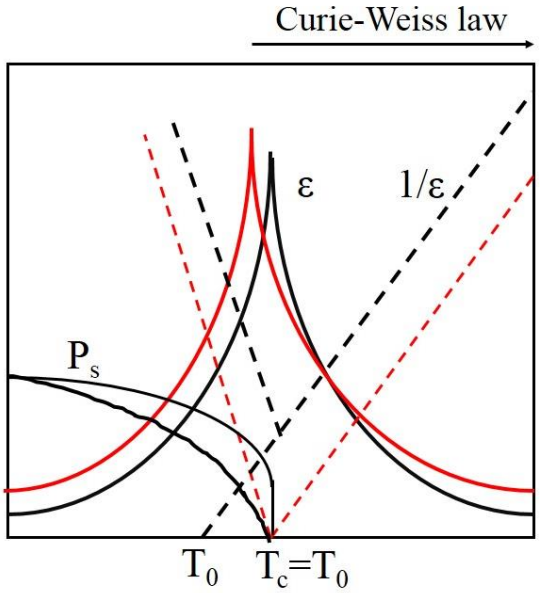

Figure 4 the temperature dependence on ε, 1/ε and polarization (P_s) for a ferroelectric. The first order phase transition from the paraelectric to the ferroelectric is defined by black line. When $T_C=T_0$, the phase transition is a second order (Red line)

The Curie-Weiss law can explain the high temperature ε above T_C which this as shown in equation 4

$$\varepsilon = \varepsilon_0 + \frac{C}{T - T_0} \approx \frac{C}{T - T_0} \qquad (4)$$

Where C is the Curie constant.

T_0 is the Curie-Weiss temperature which is obtained from the extrapolation of the high temperature $1/\varepsilon$ data with intersect the abscissa axis. $T_0 = T_C$ is only case for the second order phase transitions.

Ferroelectric is divided into four groups:

1 pylochlore group ($A_2B_2O_6$ or $A_2B_2O_7$)

2 tetragonal tungsten bronze group ($A1_2A2_4C_4B1_2B2_8O_{30}$)

3 bismuth-layer structure group ($A_{\eta-1}B_\eta O_{3\eta+1}$)

4 octahedral group (ABO_3).

In general, the octahedral group is called the perovskite group. The sequence of the phase transitions characters in perovskite structure present in Figure 5 which

one of the best example of ferroelectric is the barium titanate ($BaTiO_3$: BT) (39). At high temperature, the BT structure has cubic phase with $Pm\bar{3}m$ space group. It was found that the A-site cation has a 12 fold coordination, while the B-site cation has a 6 fold coordination. The O^{-2} is coordinated with 4 A-site cations and 2 B-site cations. When temperature decreased below T_C, the BT ceramic showed a non-centrosymmetric tetragonal phase (T) with a P4mm (commensurate) or P4bm (incommensurate) space group. Further decreasing temperature, the phase of BT ceramic was performed orthorhombic phase (O) with the space group Amm2. And finally, the cooling lead to the formation of a rhombohedral phase (R) with R3c space group.

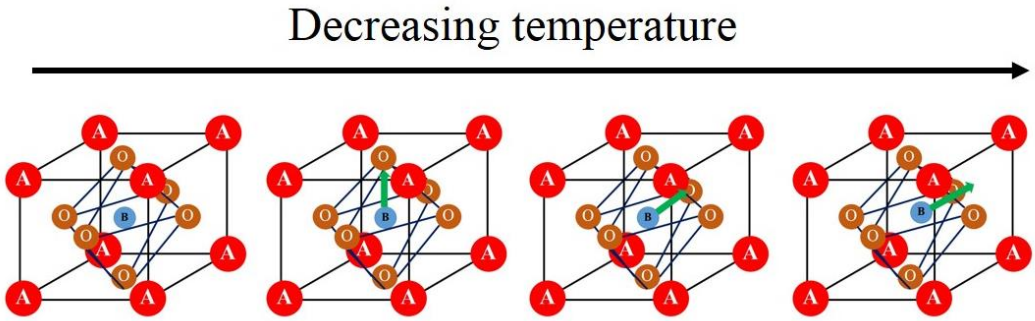

Figure 5 Unit cells of perovskite structure (ABO_3). Octahedral of O anions are denoted in brown and arrows are denoted polarization. When temperature decreased, the cubic perovskite structure distorts to tetragonal, orthorhombic and rhombohedral phase, respectively (37)

The origin polarization of A-site or B-site depended on Goldschmidt Tolelance Factor (4) as displayed in equation 5.

$$t = \frac{r_A - r_O}{\sqrt{2}\left(r_B + r_O\right)} \tag{5}$$

Where r_A, r_B and r_O is the ionic radii of A and B cations and O anions, respectively. The t value for the different structure displayed in Table 2.

Table 2 the t value for several structure

t	structure	Explanation	Example
>1	Hexagonal	A ion too big or B ion too small	$BaNiO_3$
0.9-1	Cubic	A and B ions have ideal size	$SrTiO_3$, $BaTiO_3$
0.71-0.9	Orthorhombic/ Rhombohedral	A ions too small to fit into B ion interstices	$GdFeO_3$, $CaTiO_3$
<0.71	Different structure	A ions and B have similar ionic radii	$FeTiO_3$

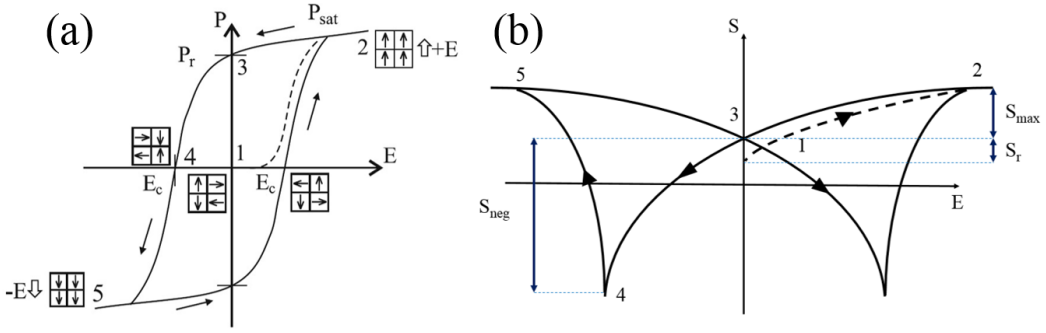

Figure 6 (a) P-E hysteresis loop and (b) S-E loop of a ferroelectric

The characteristic of polarization and strain hysteresis loops in ferroelectric material can occurred by the extrinsic contributions. The hysteresis loop of polarization vs. electric field (P-E) and strain vs. electric field (S-E) are presented in Figure 6 (a) and (b). Point "1" referred to the origin of the state characteristic by the random poly domain pattern with zero electric field, as see in Figure 6 (a). The polarization was increased when electric field was applied. At low electric field, the response is linear and slightly increased with the electric field become high which can be explained by the domain rotation in direction of the applied electric field. When increasing the applied electric field, all domain has possible switched and reached the saturation polarization (P_{max}), as see in point "2". In the same point, the material will

give a maximum strain (S_{max}). It is well known that the large signal piezoelectric coefficient (d_{33}^{*}) is important figure of merit for the actuator which can be defined by the equation 6.

$$d_{33}^{*} = \frac{S_{max}}{E_{max}} \quad (6)$$

Where, E_{max} is the field at the maximum strain S_{max}. At point "3", the applied electric field is removed, the remnant polarization (P_r) and remnant strain (S_r) were observed due to some domain will switch back. At point "4", opposite electric field was applied, the polarization will be switching to initial state of zero net polarization which is called coercive field (E_c). Moreover, the negative strain (Sneg) in the region (point 3-4), owning to the direction between applied electric field and spontaneous polarization is opposite. The spontaneous polarization will become parallel to the applied electric field while the strain become positive. Further increase of the applied electric field in the negative side until the maximum (point "5") and then removed to zero (point "6"), the results are shown hysteresis loops completely. In case of the ideal, P-E and S-E loops are perfectly symmetric which $+E_c = -E_c$ and $+P_r = -P_r$. However, we will consider the disturbance such as the charged defects, preparation condition, mechanical stresses and thermal treatment (40) which these disturbances are effect to the symmetric of the hysteresis loops.

Magnetism

Ferromagnetism can be explained by the three principal sources such (i) the spin of an electron, (ii) electron orbital angular momentum of the nucleus and (iii) a change in the orbital moment induced by an applied magnetic field. The first two effect provide the paramagnetic behaviors and the third provides a diamagnetic contribution (41).

In a crystal, the factors are affected to the magnetic properties include (i) the magnetic moment in each atom/ion and (ii) the interaction between the magnetic moments. In case of around each atom/ion has no unpaired electrons, there will no net magnetic moment concerned with them (keeping in mind that the in a fully filled

orbital, the both orbital moment and electron spin dismiss to zero) which the material will exhibit diamagnetic behavior. In case of unpaired electrons, the net magnetic moment of all atom/ion are depended on the interaction between the magnetic dipole, which induced the material will exhibit paramagnetism (PM), ferromagnetism (FM), antiferromagnetism (AFM) and ferrimagnetism (FIM). The detail of each type of magnetism are presented in next paragraph.

Diamagnetism (42)

In the magnetic property, electron spin is more important in defining of an atom. In electron, all of the electrons are paired and shared their orbital with another electron. Therefore, in each orbital the total spin is zero and the diamagnetic was found. When the magnetic field was applied, the diamagnetic atoms are not attracted but are slowly repelled. Moreover, a negative magnetization is created the negative magnetic susceptibility as showed in Figure 7 (a) and depended on the temperature as showed in Figure 7 (b).

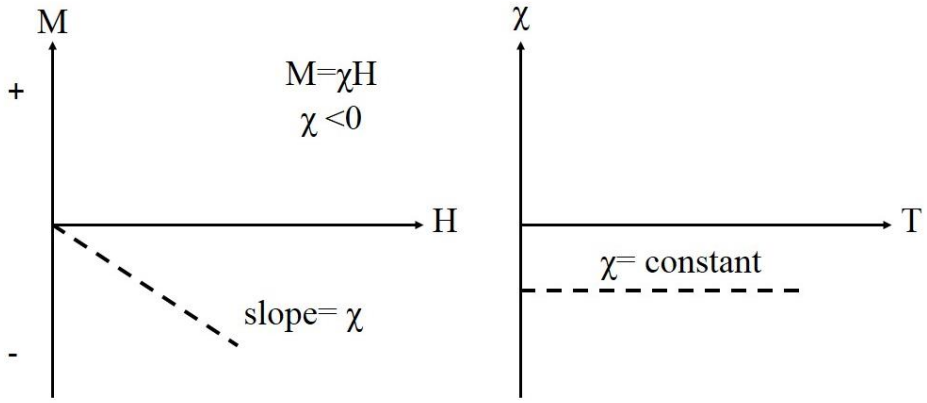

Figure 7 (a)-(b) Diamagnetism of material

Paramagnetism (43)

Paramagnetism was discovered by Michael Faraday in 1845 which this behavior was showed some elements and some compounds. For the paramagnetic, the orbital has alone electrons which was produced the net spin. In other words of the diamagnetism, paramagnetic atoms are slightly responded to a magnetic field due to the permanent magnet are aligned with the external magnetic field. Paramagnetic properties do not remain magnetization without the externally applied magnetic field,

because of the spin was randomizes orientations by thermal motion. The magnetization of the paramagnetic is the same diamagnetic (different direction) and the net positive magnetization created a positive susceptibility as showed in Figure 8 (a). The susceptibility of this behavior is backward by the temperature caused from the randomization as exhibited in Figure 8 (b).

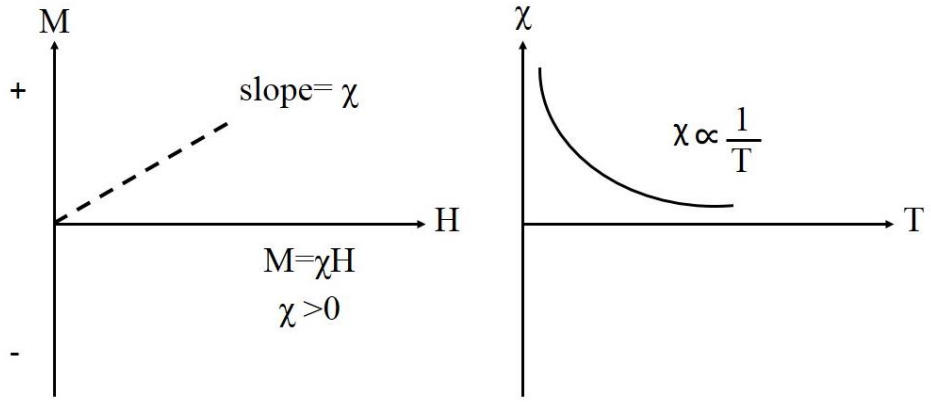

Figure 8 (a)-(b) Paramagnetism of material (44)

Ferromagnetism (45)

Ferromagnetism materials show strong magnetic when compared with the diamagnetic and paramagnetic. The ferromagnetic was found some elements have such as ion (Fe), cobalt (Co) and nickel (Ni) etc. The atomic moment of the ferromagnetic is very strong interaction which these interactions arise from the electronic exchange forces. Resulting, the atomic moments are align in a parallel or antiparallel as showed in Figure 9.

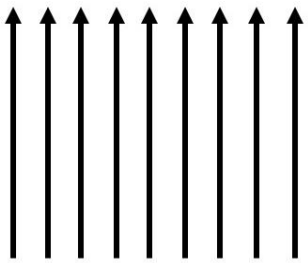

Figure 9 Parallel alignment

In ferromagnetic, the parallel alignment of moments lead to the large net magnetization even in the absence of a magnetic field. The characteristic of ferromagnetic materials are explained by the two distinct as

Spontaneous magnetization

In case of the absence of a field, spontaneous magnetization is the net magnetization that exists inside a uniformly magnetized microscopic volume. At 0 K, the magnitude of this magnetization is dependent on the spin magnetic moments of electrons. We can measure the saturation magnetization by the applied magnetic field as show in Figure 10. In in a magnetic field, the maximum saturation magnetization was induced by the magnetic moment. The saturation magnetization is an intrinsic property and dependent on temperature but independent of particle size. The ferromagnetic is orderly at below Curie temperature (T_c).

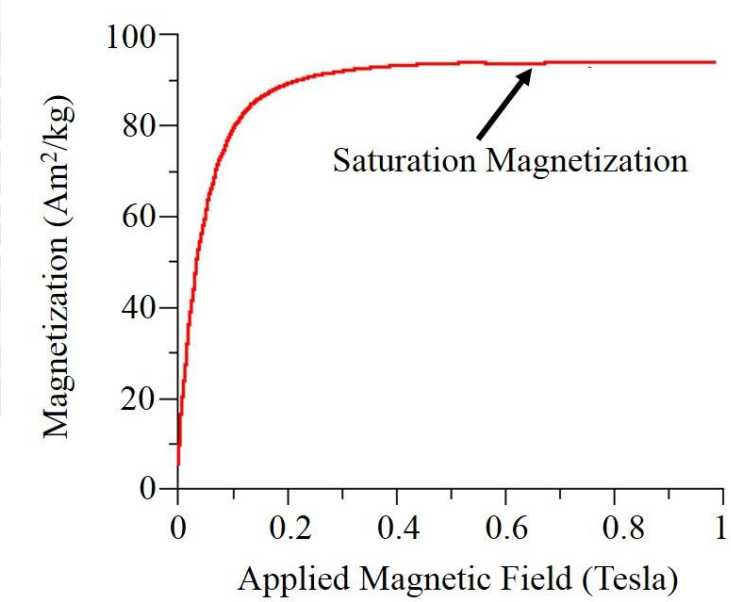

Figure 10 the Magnetization vs applied magnetic field of ferromagnetic material

The ferromagnetic are alighted at lower Curie temperature and then distorted with higher temperature. The saturation magnetization (M_S) of the ferromagnetic materials is continuously decreased with temperature increased and the M_S value is zero at the Curie temperature as showed in Figure 11.

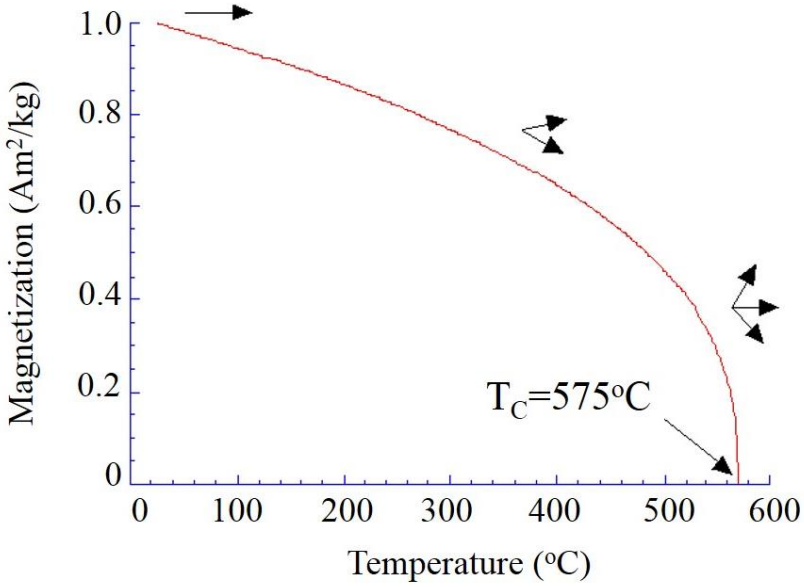

Figure 11 Curie temperature of the ferromagnetic materials

When a ferromagnetic material is induced in one direction, the magnetization will not back to zero when applied field is removed. By a field in the opposite direction, the magnetization can be driven back to zero. Under the magnetic field, its magnetization will trace out a loop which was call a hysteresis loop which related to the subsistence of the magnetic domains in the material as shown in Figure 12. The property of ferromagnetic material is useful as a magnetic memory including the audio tape recording and magnetic storage of data on computer disks.

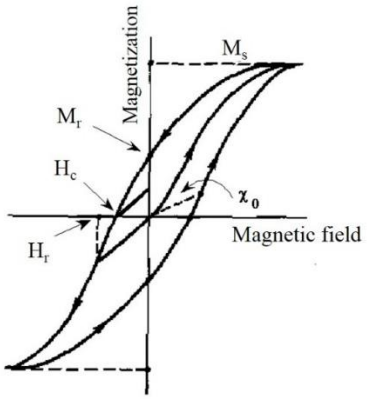

Figure 12 The hysteresis loop of ferromagnetic material

Antiferromagnetism (46)

Antiferromagnetic material at all temperature show the small positive susceptibility (χ), but are vary in a peculiar way with temperature. Figure 13 exhibit the susceptibility of the relationship between antiferromagnetic and temperature. χ increase with temperature increase.

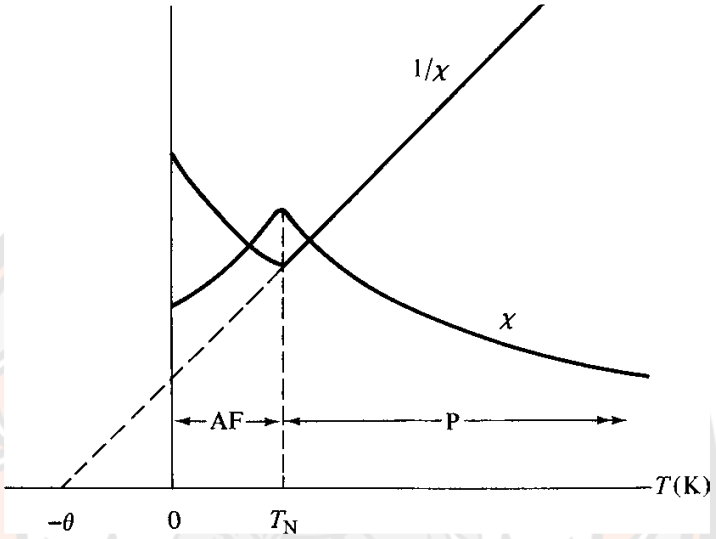

Figure 13 Temperature dependence of the susceptibility and inverse susceptibility for an antiferromagnetic material. AF= antiferromagnetic, P=paramagnetic

Ferrimagnetism (47)

The ferromagnetic is one of a kind of magnetic ordering which exhibit a substantial spontaneous magnetization at room temperature like to the ferromagnetic. The ferrites including the double oxide of ions and another metal are most important of the ferromagnetic substance. The magnetic ferrites was separated into two groups with different crystal structure:

1. Cubic. The $MO{\cdot}Fe_2O_3$ is the general formula of these type, where M is a divalent metal ion such as Mn, Ni, Fe, Co and Mg. All of the divalent metal ion are magnetically soft except cobalt ferrite is magnetically hard.

2. Hexagonal. Barium ferrites ($BaO{\cdot}6Fe_2O_3$) and strontium ferrites ($SrO{\cdot}6Fe_2O_3$) are the most important in this type and show magnetically hard.

Multiferroics material

Multiferroics are the one of a kind material which those materials have more than on of properties such as ferroelectric, ferromagnetic and ferroelasticity. P. Cuire (48), the crystal could be present ferroelectric and ferromagnetic which ferroelectric and magnetization was induced by the electric field, and vice versa. This interaction is called magneto electric coupling which refers to the magnetization by an electric field or polarization by a magnetic field. This effect is very interesting for a novel spintronic devices such as tunneling magnetoresistance (TMR) sensors, spin values with functionality which is tunable by an electric field and multi-state memories in which data are written electrically and read magnetically. The schematic diagram about the concepts of the ferromagnetic and ferroelectric presented in Figure 14. In this diagram, the ferromagnetic and ferroelectric are subset of the magnetically and electrically, respectively. In this diagram, the intersection between the ferroelectric and ferromagnetic materials are call the multiferroic material which showed by the smallest circle in the middle. This characterization would exhibit magneto electric coupling. The example of multiferroic material included the $BiFeO_3$ and $BiMO_3$.

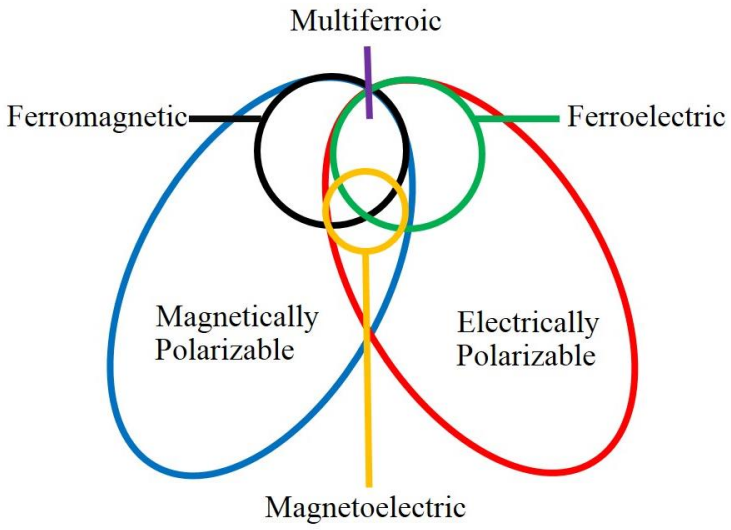

Figure 14 Multiferroic materials combine magnetic and ferroelectric properties (48)

Impedance Spectroscopy

In 1880s, Oliver Heaviside reported the first concept of electrical impedance and after that A. E. Kennelly and C. P. Steinmetz developed in term of vector diagrams and complex. The electrical impedance explains by a measure of opposition alternating current (AC) which extended the concept of the resistance to AC circuits. The description of this concept are not only the relative amplitude of the voltage but also the relative phase. Impedance is determined as the frequency domain ratio of the voltage to the current. Otherwise, for a single complex exponential, it is voltage current ratio at a particular frequency (ω). Generally, impedance will be a complex number Z(ω)=Z'+jZ" which composes of a real and imaginary part. Figure 15 shows to plot of the real part (X-axis) and imaginary part (Y-axis).

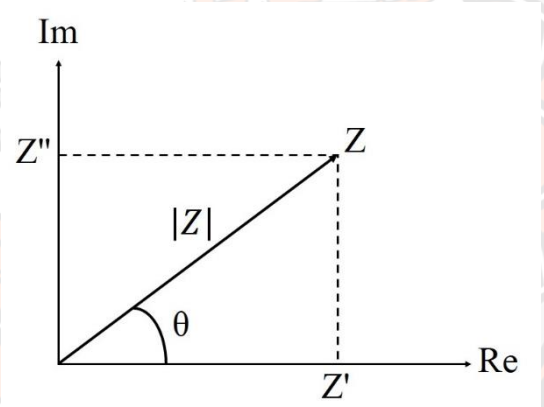

Figure 15 A graphical representation of the complex impedance plane

Hence, the two rectangular coordinate values are

$$\mathrm{Re}(Z)=Z'=|Z|\cos\theta \text{ and } \mathrm{Im}(Z)=Z''=|Z|\sin\theta \tag{7}$$

$$\theta = \tan^{-1}\left(Z''/Z'\right) \tag{8}$$

And the modulus

$$|Z| = \left[(Z')^2 + (Z'')^2\right]^{1/2} \tag{9}$$

In the polar form, the Z written as $Z(\omega)=|Z|\exp(j\theta)$ which $\exp(j\theta)=\cos(\theta)+j\sin(\theta)$.

To obtain the complex impedance (Z), the relationship of three other complex formalism such admittance (Y), permittivity (ε) and electric modulus (M). Hence, the impedance spectroscopy data can be analyzed by the four different formalism which the mathematical relation are showed below.

$$Z = Z' - jZ'' \tag{10}$$

$$\left.\begin{aligned} Y &= \frac{1}{Z} = \frac{1}{Z' - jZ''} = \frac{Z' + jZ''}{(Z')^2 + (Z'')^2} \\ Y' &= \frac{Z'}{(Z')^2 + (Z'')^2} \\ Y'' &= \frac{Z''}{(Z')^2 + (Z'')^2} \end{aligned}\right\} \tag{11}$$

$$\left.\begin{aligned} M &= j\omega C_0 Z = \omega C_0 (Z' - jZ'') = \omega C_0 Z'' + j\omega C_0 Z' \\ \mathrm{M}' &= \omega \mathrm{C}_0 Z'' \\ \mathrm{M}'' &= \omega C_0 Z' \\ C_0 &= \varepsilon_0 \frac{A}{d} \end{aligned}\right\} \tag{12}$$

$$\left.\begin{aligned} \varepsilon &= \frac{1}{M} = \frac{1}{M' + jM''} = \frac{1}{\omega C_0} \bullet \frac{Z'' - jZ'}{(Z')^2 + (Z'')^2} \\ \varepsilon' &= \frac{1}{\omega C_0} \bullet \frac{Z''}{(Z')^2 + (Z'')^2} \\ \varepsilon'' &= \frac{1}{\omega C_0} \bullet \frac{Z'}{(Z')^2 + (Z'')^2} \end{aligned}\right\} \tag{13}$$

Where Z' and Z'' are the real and imaginary parts of complex impedance, $j = \sqrt{-1}$, $\omega = 2\pi f$ is the angular frequency and C_0 is capacitance of vacuum in the measuring cell.

The capacitance can be directly calculated from the M or ε. While, the resistance can be calculated indirectly from $\omega RC = 1$. Likewise, Z or Y can be used to calculate resistance directly and hence capacitance can be calculated from $\omega RC = 1$. For the Z and M formalism, a parallel RC circuit exhibited a single semicircle as showed in Figure 16

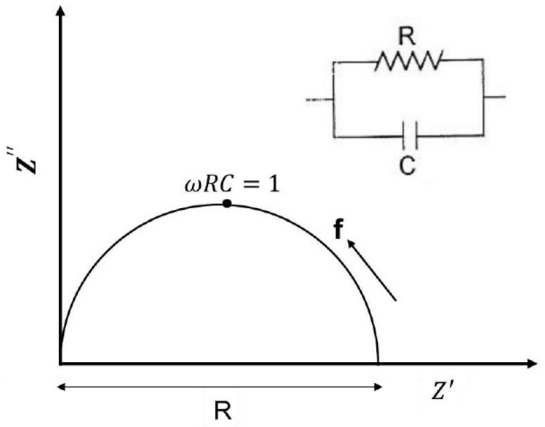

Figure 16 the complex plane plot of impedance formalism for electrically homogenous dielectric

In case of the material has more than one electro-active parts, the another parallel RC circuit was introduced. The complex plane plot of two parallel RC elements concerned in series are presented in Figure 17.

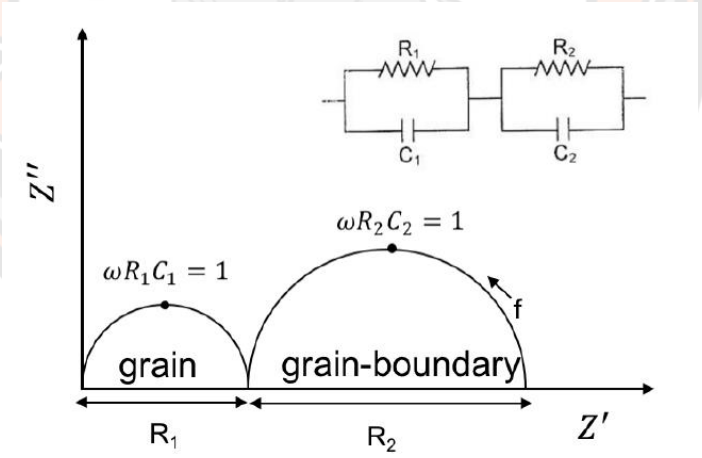

Figure 17 the plot of complex impedance for a dielectric with difference responses from grain and grain boundary

Where, R_1 is resistance of the grain and R_2 is the resistance of grain boundary. Generally, grain boundary has more resistive than grain because the void, secoundary phase and crystal anisotropic etc. The total resistance of the material are given by equation 14

$$R_{total} = R_{grain} + R_{grain-boundary} \quad (14)$$

Due to the capacitance is depended on the geometry, its scale is a good factor of separating between different electro-active regions. For instant, a grain boundary must have high capacitance due to this sample have vary less thickness when compared with the grain. The possible interpretations of capacitance value are listed in Table 3 (49, 50).

Table 3 Capacitance value in each phenomenon

Capacitance (F)	Phenomenon
10^{-12}	bulk
10^{-11}	secondary phase(s)
10^{-11}-10^{-8}	grain boundary
10^{-10}-10^{-9}	bulk ferroelectric
10^{-9}-10^{-7}	surface layers
10^{-7}-10^{-5}	sample-electrode interface
10^{-4}	electrochemical reaction

Electrical circuit elements

The analysis of electrochemical impedance spectroscopy data can obtain from the fitting of an equivalent electric circuit model. The model of circuit elements are the electrical elements such resistors, capacitors and inductors. In the impedance of the standard circuit components, the knowledge of the common electrical elements are the most important in this chapter. Table 4 show the list of the common circuit element, the equation of the relationship between the current and voltage and impedance.

Table 4 Common electrical elements

Component	Current vs. voltage	Impedance
resistor	E=IR	Z=R
Inductor	E=L di/dt	Z=jωL
capacitor	I=C dE/dt	Z=1/jωC

Elementary analysis of impedance spectra

Physical models for equivalent circuit elements

All the process of physic electrical model may occur in examination on an electrode-material system which initial use might be unavailable, premature or perhaps too complicated. In experiment of impedance data $Z_e(\omega)$ can be approximated by the impedance of an equivalent circuit $Z_{ec}(\omega)$ in ideal resistors, capacitors, perhaps inductances, and possibly various distributed circuit elements. The bulk conductivity of the material or the chemical step corresponded with an electric reaction are often determined by the resistance represents a conductive path and a given resistor in the circuit. Generally, capacitance and inductances will be related with space charge polarization region and with specific adsorption and the process of electro-crystallization at an electrode. The ordinary circuit elements including the resistors and capacitors are always considered as quantities with lumped-constant which correspond ideal properties. However, the real resistors are finite size and distributed in space; thus, they always associated with inductance, capacitance and time delay of response similar to resistance.

The impedance spectra can be divided two types of distributions. (i) The nonlocal process such a diffusion can occur even though in a completely homogeneous material, the charge mobility which is the physical properties and are the same as everywhere. (ii) The another types, the constant-phase element (CPE) are the good example, generating due to the distribution of the microscopic material properties. In the microscopic level, the solid electrode-solid electrolyte interface are not often assumed smooth and uniform surface since it is containing of a large number of surface such kinks, jags and variability in composition and stoichiometry.

Perovskite crystal structure

Perovskites are large family of crystalline ceramics which have general formula are ABO_3 such as barium titanate ($BaTiO_3$), lead titanate ($PbTiO_3$), lead zirconate titanate (PZT), lead lanthanum zirconate titanate (PLZT), bismuth sodium titanate ($Ba_{0.5}Na_{0.5}TiO_3$) and potassium niobate ($KNbO_3$). The name of perovskite are defined by the specific rare mineral calcium titanate ($CaTiO_3$) which have a cubic structure with a point group of m3m. The simple cubic structure composed of the oxygen at the corner is shared in the octahedral (BO_6) arranged in 3D with smaller ionic radios and high charged cations (B: Ti^{4+}, Zr^{4+}, etc.) which located in the center of the body. The schematic diagrams of the perovskite structure are displayed in Figure 18.

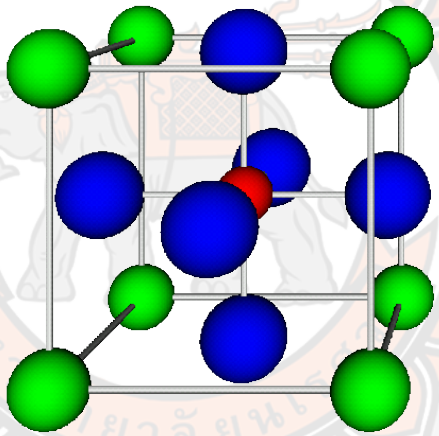

Figure 18 the perovskite structure with A site at the corner of unit cell (green spheres), B site at the center of unit cell (red sphere) and oxygen at face-center of unit cell (blue spheres) (51)

Microstructure of Ceramics

Microstructure is playing an important factor for the properties of a material. For ceramics, the crystalline are demonstrate both of single crystals and polycrystalline solids. A single crystal is a solid in which an orderly and arrangement of the atoms, ions, or molecules which is repeated throughout the entire volume. While, a polycrystalline solid is included of a small single crystals (the grains), which separated by grain boundaries and normally have random crystallographic orientations as seen in Figure 19. In general, the grains of ceramic are in the range of

1 to 50 μm and can be investigated with microstructure term and are visible only microscope such as Scanning electron microscope (SEM) (52). Many properties of ceramics are dependent on microstructure which is defined by the shape and size of the grains, existence of porosity, second phases, and other properties, as well as their distribution.

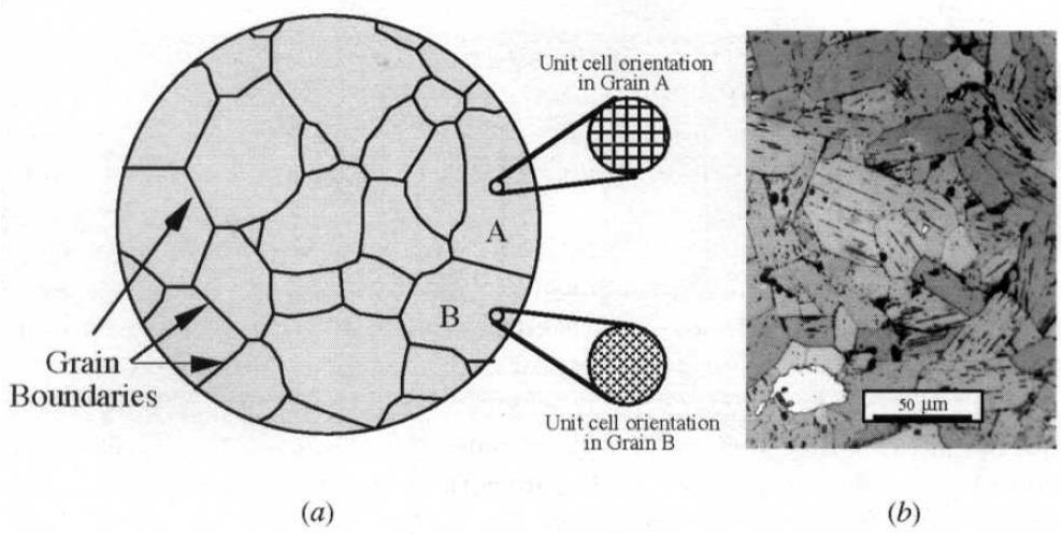

Figure 19 (a) Diagram of a polycrystalline sample. A polycrystal is consist of numerous grains separated from one another by areas of disorder called grain boundaries and (b) Normal microstructure as seen via an optical microscope

Methodology of fabrication ceramics

Solid-state reaction method

The solid-state reaction method is wildly used to prepare the polycrystalline solid from a mixture of solid starting material. This technique is related to the chemical decomposition which the solid reactants are heated producing a new solid and simple oxides powders are used such as carbonates, hydroxides, nitrates, sulfates, acetates, oxalates, alkoxides and other metal salts fabrication. Normally, the reaction of solid do not occurred at room temperature but are often occurred in the temperature range 1000 to 1500^{o}C. Such as the reaction between barium carbonate and titanium oxide produce barium titanate at high temperature by solid state reaction method.

$$BaCO_3\ (s) + TiO_2\ (s) \text{ ------> } BaTiO_3\ (s) + CO_2\ (g) \quad \text{heat to } 1200^{o}C \quad (15)$$

The advantages of solid-state reaction are easier, convenient and low cost. However, it is well known that the solid state reaction method are required compulsory grinding of different oxide mixtures for long periods of time as well as sintering. In addition, the powders were obtained from this method show low purity and large particle size.

Sol-Gel processing

Sol-Gel processing was used to synthesis various oxide materials (53). Generally, this method can control the texture, the chemical and the morphological properties of the solid. This method has several advantages such as allowing impregnation or coprecipitation. Moreover, the advantage of the sol-gel method is including molecular scale mixing, high purity of the precusors and homogeneity of the sol-gel products with a high purity of physical, morphological and chemical properties (54). In a sol-gel process, a colloidal suspension or a sol is formed by the hydrolysis and polymerization reactions of the precursors which are normally inorganic metals salts or metal organic compounds (55). Afterward, the gel were obtained from the drying process, resulting product is readily converted to Xerogel, Aerogel or Cryogel based on the mode of drying. The flowchart of the sol-gel method is shown in Figure 20. The summary of the key steps in a sol-gel method, including the aim of each step along with experimental parameters are showed in Table 5.

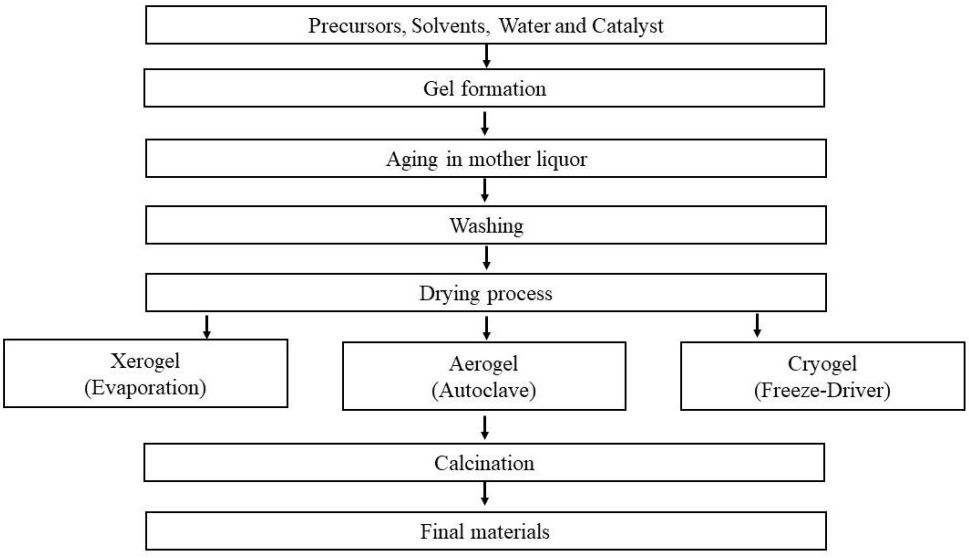

Figure 20 Sol-Gel and drying flowchart

Table 5 Important parameters in the various steps of the sol-gel method (56, 57)

Step	aim	Important parameters
Solution chemistry	To form gel	Type of raw materials, type of solvent, water content, raw material concentration, temperature, pH
Aging	To allow a gel undergo changes in properties	Time, temperature, composition of the pore liquid, aging environment
Drying	To remove solvent from a gel	Drying method, temperature and heating rate, pressure and pressurization rate, Time
Calcination	To change the chemical properties of the solid, resulting in crystallization and densification.	Temperature and heating rate, time, gaseous environment (insert, reactive gases)

Hydrothermal synthesis method

Hydrothermal synthesis is processed to perform as crystal synthesis or crystal growth in hot water under high pressure condition in aqueous solution. This method can be useful to control grain size, particle morphology, crystalline phase and surface chemical by the regulation of the solution composition, reaction temperature, pressure, solvent properties, additives and aging time (58). However, this method has disadvantage that the high cost and the inability to investigate crystals during the process their growth.

Combustion technique

Combustion technique is related to the energy released from the reaction of oxidation and reduction. This technique is an important for the synthesis and processing. Due to, this technique relates a self-sustained reaction between material and fuel such as urea, citric acid, glycine, alanine or carbohydrazide which led to lower firing temperature and shorter dwell time. Moreover, the benefits of this

technique are inexpensive raw materials, simple preparation process, and resulting good electrical properties (59-61).

I. Types of organic compounds

Hwang et al (62) studied the decomposition o the five fuels with thermogravimetric analysis. The fuel such as glycine, urea, alanine, citric acid or carbohydrazide are chosen which some properties of these fuels are listed in Table 6. The thermal analysis of these organic fuels has different weight losses. Using carbohydrazide as organic fuel, the chemical reaction varies rapidly occurred. However, the remaining weight is 22% of its original weight. In case of glycine and alanine, the results of both thermogravimetric demonstrations are similar. The reactions are very rapidly, and the remaining weights are lower than 10%. In case of urea and citric, the chemical reaction of the both organic fuels was not rigorous comparing with glycine and alanine.

II. Influence of fuels and development of novel synthesized combustion technique of powders and ceramics

The crystal structure and microstructure of Ni-Zn ferrites prepared by the combustion technique with various organic fuels was investigated by Hwang et al. [4]. The pure phase of Ni-Zn was obtained from the sample using glycine, alanine and carbohydrazide as a fuel as show in Figure 22. The nanocrystalline size is in the range of 20.2-43.7 nm as listed in Table 7. It can be clearly seen that the nanocrystalline size can be produced by the combustion technique.

Table 6 Some properties of organic compounds (62)

properties	Organic component				
	Alanine	Glycine	Carbohy-drazide	Urea	Citric acid
Structure formula	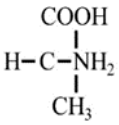	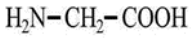	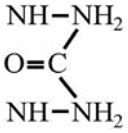	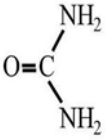	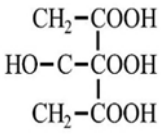
Molecular weight (g/mol)	80.1	90.1	75.1	60.1	192.1
Heat of combustion (kJ/g)	18.2	13.0	12.6	10.5	10.2
Decompo-sition temperature (°C)	314	262	153	135	175

Table 7 Effect of various fuels of the Ni-Zn ferrites prepared by the combustion technique

Fuel	T_m[a] (^oC)	Amount of gas produced (mole)	Crystallite size[b] (nm)	Surface area (m^2/g)	Carbon content (wt.%)	Ni^{2+}:Zn^{2+}:Fe^{3+}	M_s[c] (Am^2/kg)
Alanine	1245	20.7	38.6	24.7	1.64	0.500:0.467:1.920	60.8
Glycine	1150	26.2	32.7	31.2	1.53	0.500:0.471:1.922	62.4
Carbohydrazide	1380	24.0	43.7	20.6	1.87	0.500:0.462:1.917	58.5
Urea	785	30.7	20.2	3.82	3.82	0.500:0.483:1.936	57.2
Citric acid	725	26.2	22.7	5.75	5.75	0.500:0.490:1.947	55.8

Note: [a]T_m the maximum combustion temperature, measured by Pt-Pt-Rh thermocouple.

[b]Crystalline size of the as-synthesized Ni-Zn ferrite powders calculated from the line broadening of the (311) XRD peak by Sherrer formula.

[c]Ms the saturation magnetization of the sintered Ni-Zn ferrite samples (950^{o}C/2h)

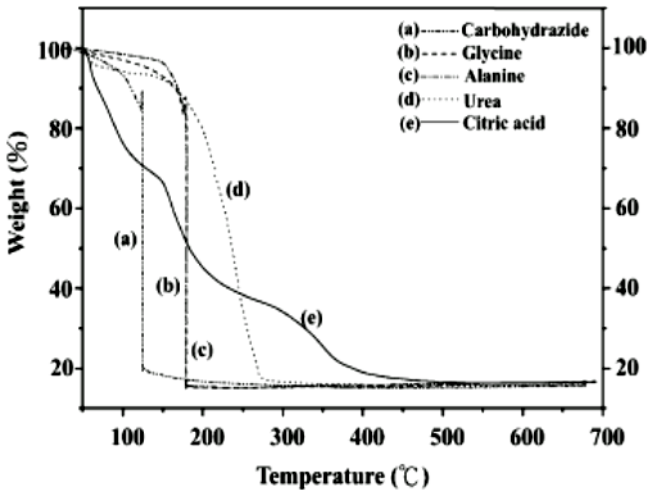

Figure 21 Thermogravimetric of fuel

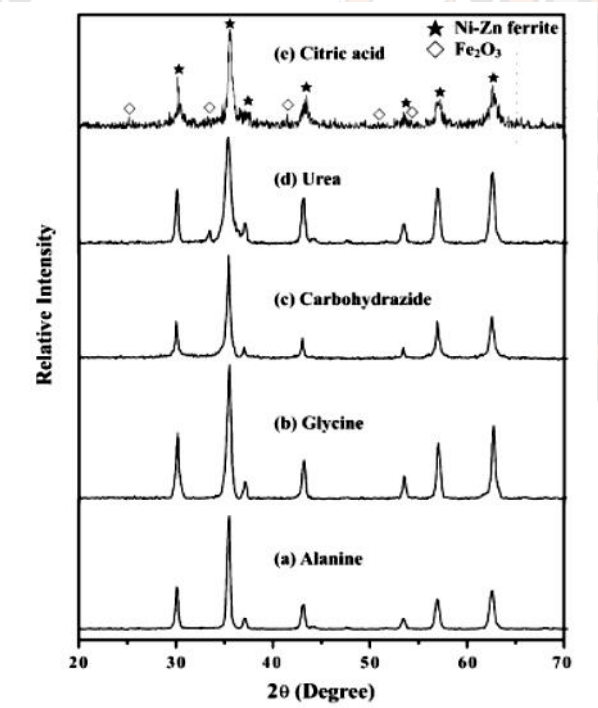

Figure 22 XRD patterns of the Ni-Zn ferrites with various organic fuels: (a) alanine (b) glycine (c) carbohydrazide (d) urea and (d) citric acid (62)

The literature of this research

Lead-based piezoelectric materials are important for technological application in electronic devices such as sensors, actuators and transducers. Due to their excellent piezoelectric and ferroelectric properties. However, the volatilize of lead oxide (PbO) during high temperature sintering process is very harmful health and environment. Moreover, the evaporation of raw material lead to unstable compound. Therefore, lead-free piezoelectric ceramics with a perovskite structure, such as $Bi_{0.50}Na_{0.50}TiO_3$ (BNT), $BaTiO_3$ (BT), $K_{0.50}Na_{0.50}NbO_3$ (KNN) etc. are very interesting for many researchers as their base materials are not environmental pollutants (10, 63-68).

Bismuth Sodium Titanate; $((Bi_{0.5}Na_{0.5})TiO_3$ (BNT)) ceramics

$(Bi_{0.5}Na_{0.5})TiO_3$ or (BNT) is one of the important lead-free piezoelectric materials with perovskite which discovered by Smolenskii et al. in 1960 (69, 70). For the BNT system, Bi^{3+} and Na^{+} ions occupied in A-site while Ti^{4+} occupied in B-site of unit cell. It has high Curie temperature (T_C=320^{o}C) and strongly ferroelectric properties which showed a large remanent polarization at room temperature (P_r=32 $\mu C/cm^2$) (71). However, the BNT ceramics have the drawbacks of a poor piezoelectric constant (d_{33}~90 pC/N) and a high coercive field (E_c~73 kV/cm) which causes difficulty in poling. Moreover, BNT ceramics also displayed high conductivity which cause from the high leakage current (72). The information of a structure phase in BNT-based ceramics was investigated by many researchers (70, 73-76). The result of crystal structure of BNT ceramics exhibited a perovskite structure ferroelectric with rhombohedral symmetry, space group R3c at room temperature (293 K) which studied by X-ray diffraction. Rietveld refinements were used to analyze the lattice parameters of BNT ceramic. These results are good agreement with the Joint Committee on Powder Diffraction Standards (JCPDS) number 36-0340. The lattice parameters of BNT ceramics are a= 5.4887 Å, b= 5.4887 Å and c= 13.5048 Å. The parameters obtained from Reitveld refinement for the BNT ceramics showed in Table 8.

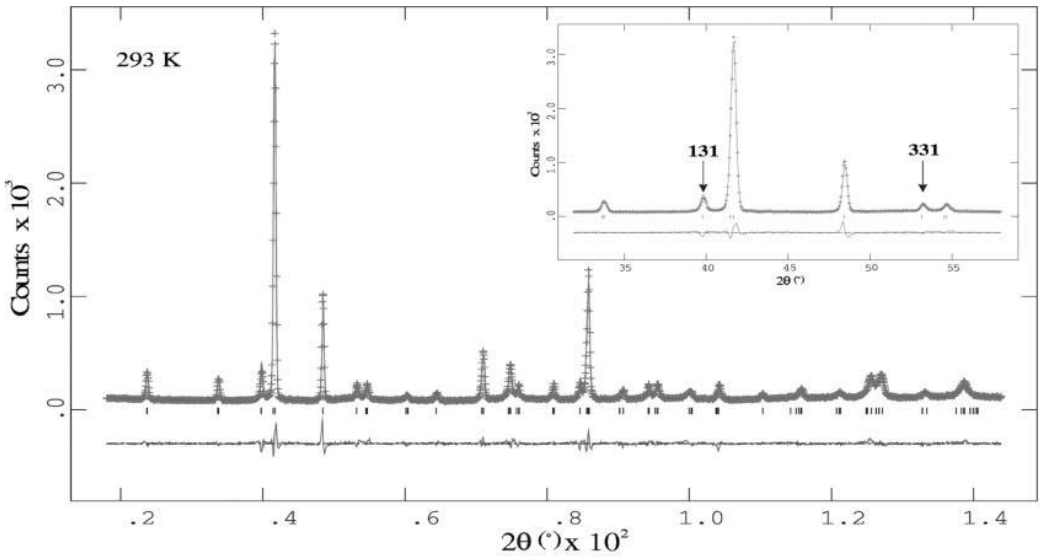

Figure 23 The observed, calculated and difference curves from the Rietveld refinement of $Na_{0.5}Bi_{0.5}TiO_3$ ceramics

Table 8 Refined structure parameters of BNT ceramics

Sample	Refine parameters	Phase structures	Atoms information			
			Label	x	y	z
$Bi_{0.5}Na_{0.5}TiO_3$	χ^2=0.323	R3c	Bi	0	0	0.2627
	R_p=0.059		Na	0	0	0.2627
	R_{wp}=0.078		Ti	0	0	0.0063
			O	0.126	0.336	0.0833

Bismuth Potassium Titanate; ($Bi_{0.5}K_{0.5}TiO_3$ (BKT)) ceramics

BKT is a typical lead-free ferroelectric ceramic which was determined by Smolenskii et al. (77), It is a perovskite structure with tetragonal symmetry at room temperature and high Curie temperature (T_C=380°C). The lattice parameters of BKT ceramics are a=3.913 Å and c=3.990 Å at room temperature as reported by Ivanova et al. (78). Hou et al. (79) studied the SEM images of BKT powder and they reported that the particle size was very small and relatively uniform which the average grain size was between 100 and 200 nm as seen in Figure 24. Moreover, BNK powders

were investigated by Lencka et al. (80) and they reported that the particles exhibited a uniform spherical with the diameter range from 40 to 150 nm as shown in Figure 25.

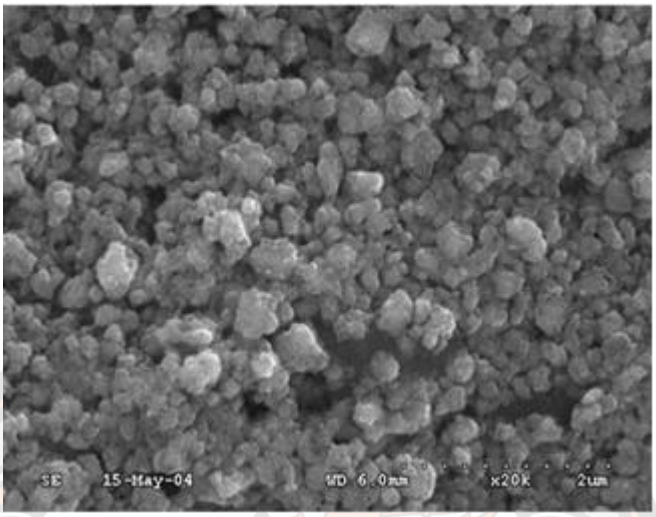

Figure 24 FESEM micrograph of the BKT powders was studied by Hou et al. (79)

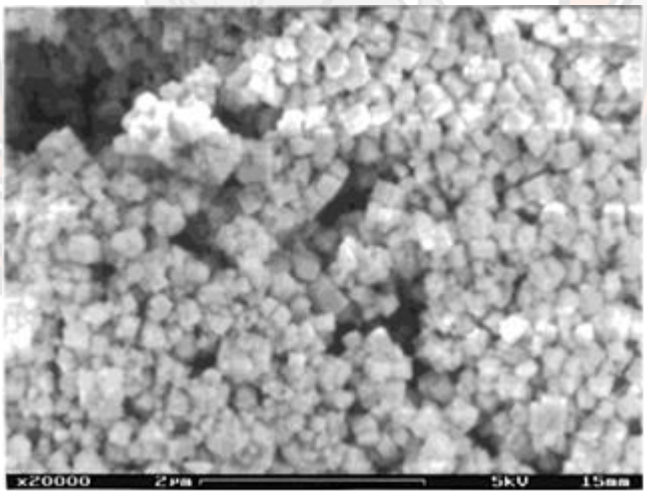

Figure 25 FESEM micrograph of the BKT powders was studied by Lencka et al. (80)

For the dielectric properties of BKT ceramics, Hiruma et al. (81) reported the dielectric constant (ε_r) and dielectric loss (tan δ) of BKT ceramics are 524 and 6.8% at 1 MHz, respectively. Other authors showed the ε_r and tan δ at room temperature of BKT ceramics at 1 kHz are 733 and 4.8%. The dielectric relaxor properties of

ferroelectric BKT single crystal prepared via the molten salt method were investigated by Yang et al. (82). They reported that the highest in ε_r is diffusive at around 357°C which related to a strong dispersion of dielectric maximum temperature (T_m) with temperature. With increasing the field frequency, the ε_r value decreases, while T_C value increases from 337°C to 362°C when frequency increased from 1 kHz to 1000 kHz. This behavior related to the relaxor ferroelectric properties, as seen in Figure 25.

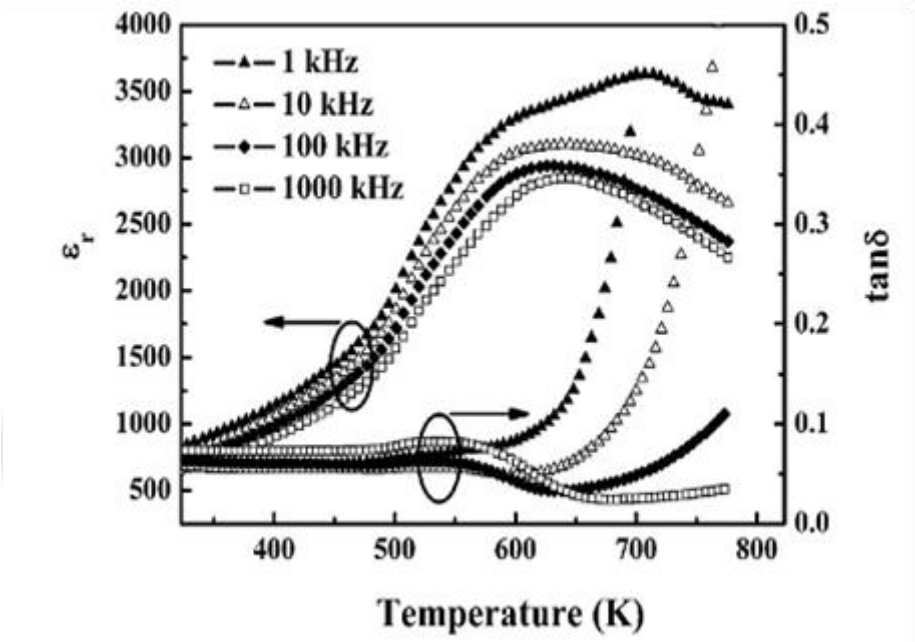

Figure 26 Temperature dependence of dielectric constant ε_r and loss tan δ at various frequencies for $(K_{0.5}Bi_{0.5})TiO_3$ ceramics (82)

The polarization hysteresis loops of BKT ceramics measured at various temperature was also reported by Hiruma et al. (83), as shown in Figure 28. It was found that the remnant polarization and coercive field continuously deceased with increasing temperature. At room temperature, BNT ceramics exhibited well shape hysteresis loop with small leakage current. The remnant polarization (P_r=22.2 $\mu C/cm^2$) and coercive field (E_c=52.5 kV/cm) were obtained from HP1080°C specimen, as shown in Figure 29.

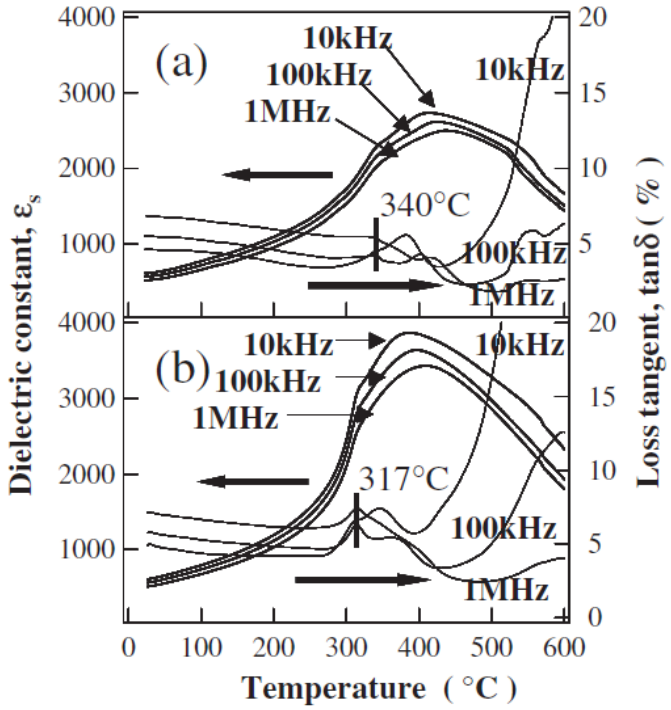

Figure 27 Temperature dependences of dielectric constant ε_s and dielectric loss tangent tan δ for hot-pressed BKT ceramics sintered at (a) 1060ºC and (b)1080ºC (83)

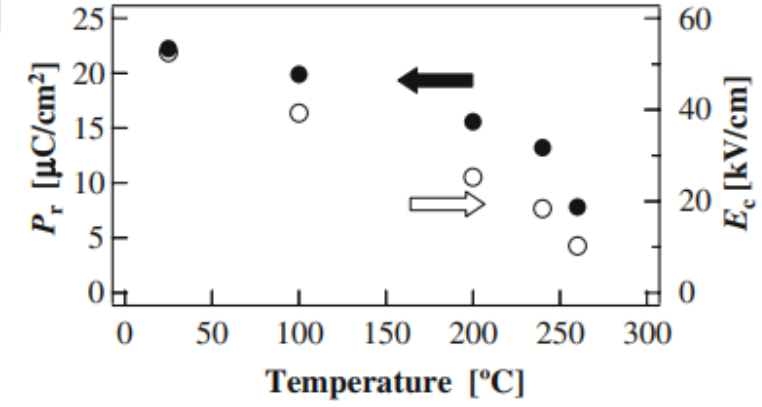

Figure 28 Temperature dependence of P_r and E_c for BKT HP1080 °C (83)

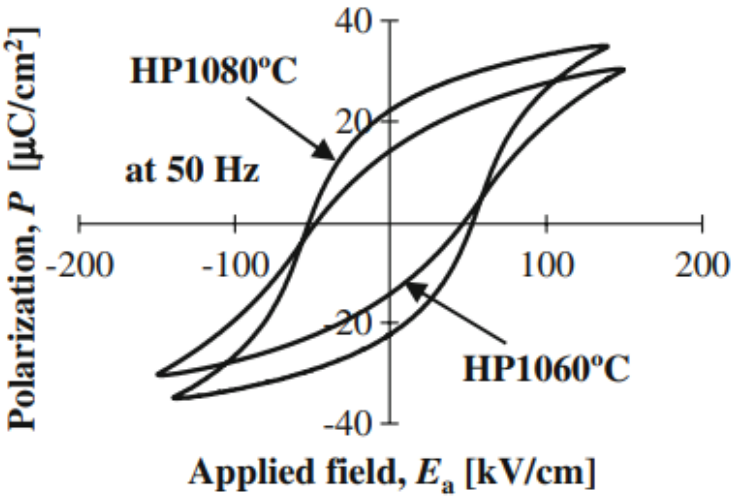

Figure 29 hysteresis loops of BKT-HP1060°C and BKT-HP1080°C (83)

To substitution and addition of some solid solutions into BNT-based ceramics can improve electrical properties. Yang et al. (84) prepared the (1-x)BNT-xBKT ceramics by were synthesized by conventional mixed-oxide method. They reported that the (1-x)BNT-xBKT ceramics exhibited morphotropic phase boundary (MPB) between rhombohedral and tetragonal with $0.16 \leq x \leq 0.22$. The density increased with x content increased up to 0.18 and then dropped, as shown in Figure 30. The optimum values of ε_r, tan δ d_{33} and K_p were 893, 0.037, 144 pC/N and 0.29, respectively which was obtained from 0.82BNT-0.18BKT ceramics.

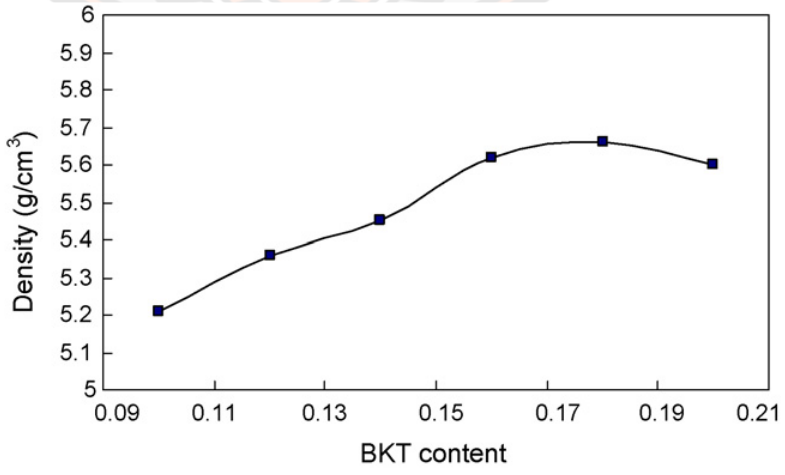

Figure 30 Density of (1-x)BNT-xBKT ceramics with different compositions

Z.P. Yang et al. (85) prepared the $Bi_{0.5}(Na_{0.68}K_{0.22}Li_{0.10})_{0.5}TiO_3$ ceramics by conventional oxide-mixed method. They reported that the $Bi_{0.5}(Na_{0.68}K_{0.22}Li_{0.10})_{0.5}TiO_3$ ceramics exhibited pure perovskite phase with rhombohedral structure, high piezoelectric constant (d_{33}~203 pC/N) and good ferroelectric properties (P_r~31.91 μC/cm^2 and E_c~32.4 kV/cm). It was found that the piezoelectric constant and ferroelectric properties of $Bi_{0.5}(Na_{0.68}K_{0.22}Li_{0.10})_{0.5}TiO_3$ ceramics represented better than BNT ceramics. In 2015, the effect of firing temperature on phase formation, microstructure and dielectric property of $Bi_{0.5}(Na_{0.68}K_{0.22}Li_{0.10})_{0.5}TiO_3$ ceramics by solid state combustion technique using glycine as a fuel were studied. It was found that the pure $Bi_{0.5}(Na_{0.68}K_{0.22}Li_{0.10})_{0.5}TiO_3$ powders were calcined at temperature of 750^{o}C for 2 hours and $Bi_{0.5}(Na_{0.68}K_{0.22}Li_{0.10})_{0.5}TiO_3$ ceramics were sintered at temperature of 1025^{o}C for 2 hours. Moreover, the $Bi_{0.5}(Na_{0.68}K_{0.22}Li_{0.10})_{0.5}TiO_3$ ceramics showed coexistence phase between rhombohedral and tetragonal, a highest density (5.79 g/cm^3), a high Curie temperature (T_C= 304^{o}C) and a highest dielectric constant at T_m (ε_m=4,340). However, the other properties could not be study. Therefore, the optimum content of K^+ and Li^+ on phase formation, microstructure and electrical properties were studied as a composition of $Bi_{0.50}(Na_{0.9-x}K_xLi_{0.10})_{0.50}TiO_3$ and $Bi_{0.50}(Na_{0.8-x}K_{0.20}Li_y)_{0.50}TiO_3$ ($0.18\leq x\leq 0.26$ and $0\leq y\leq 0.12$) via solid-state combustion technique by R. Sumang et al. (8). They reported that all sample exhibited a coexistence of rhombohedral ® and tetragonal (T) phases which the tetragonality increased with the x and y contents increased as seen in Figure 2.24 and 2.25. At x=0.20 and y=0.03, this composition exhibited high Curie temperature (T_C=313^{o}C), good ferroelectric properties (P_r=16.6 μC/cm^2 and E_c=18.8 kV/cm), the largest strain (~0.36%) and the highest normalize strain (d_{33}^*=729 pm/V).

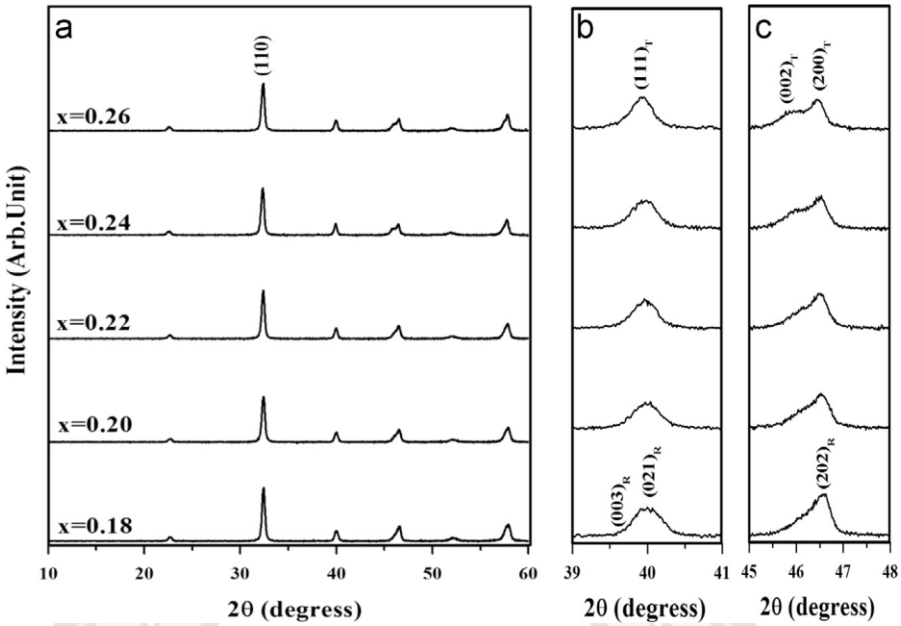

Figure 31 X-ray diffraction patterns of $Bi_{0.50}(Na_{0.9-x}K_xLi_{0.10})_{0.50}TiO_3$ ceramics

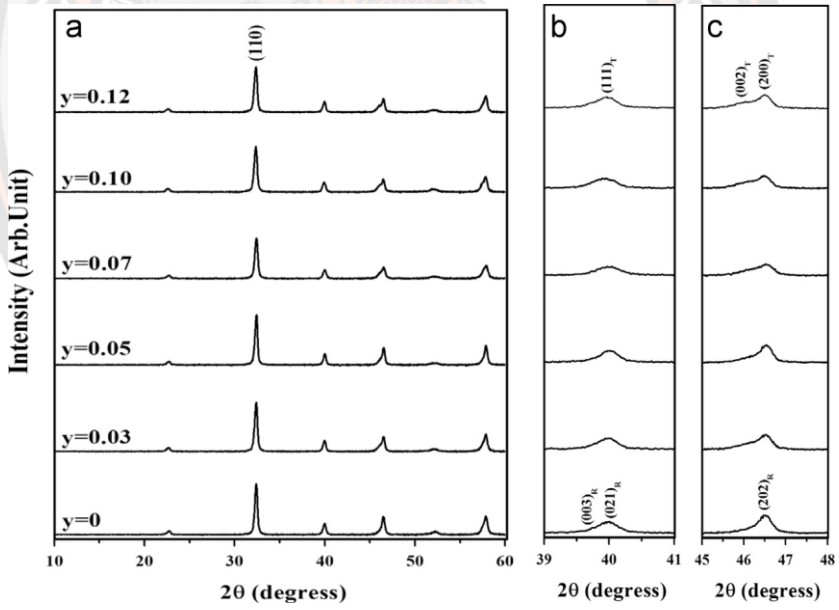

Figure 32 X-ray diffraction patterns of $Bi_{0.50}(Na_{0.8-x}K_{0.20}Li_y)_{0.50}TiO_3$ ceramics.

Potassium sodium niobite ($K_{0.5}Na_{0.5}NbO_3$; (KNN)) ceramics

Potassium sodium niobate ($K_{0.5}Na_{0.5}NbO_3$; (KNN))

KNN solid solution is arise from the combination of ferroelectric potassium niobite ($KNbO_3$ or KN) and antiferroelectric sodium niobite ($NaNbO_3$ or NN) at room temperature and both compositions showed orthorhombic phase. Generally, KN

ceramics is a good candidate to replace PZT ceramics because of its show a high Curie temperature (T_C~420^{o}C) and good piezoelectric property (d_{33}~160 pC/N). However, KNN ceramics has a poor remnant polarization (P_r~11 μC/cm^2). Moreover, the pure KNN ceramics are very difficult to prepare KNN ceramics with high density because of the evaporation of K^+ and Na^+ during sintering process (86, 87). This behavior led to the low electrical properties of KNN ceramics. Thus, many researchers developed the densification and electrical properties of KNN ceramics by the doping and substituting some ions or addition the solid solutions in the system for the preparation new solid solution with optimum content.

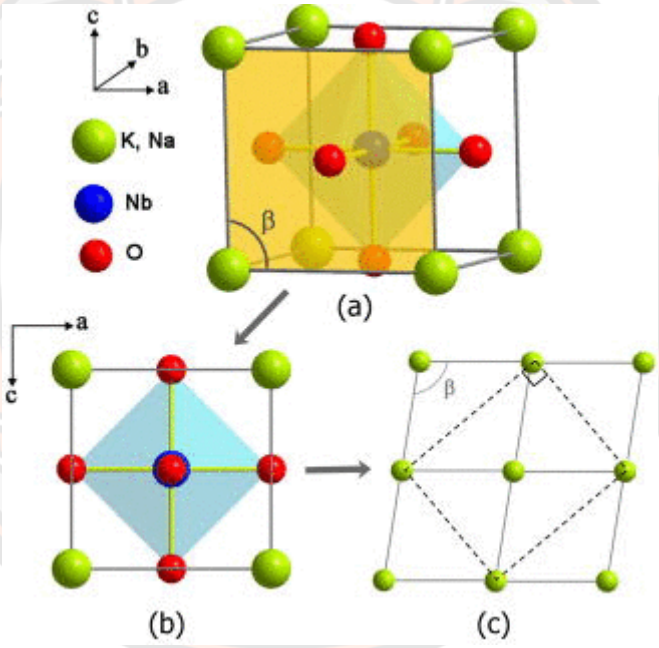

Figure 33 KNN orthorhombic perovskite structure at room temperature (86)

Yiping Guo et al. (87) prepared (1-x)($Na_{0.5}K_{0.5}$)NbO_3-x$LiTaO_3$ ((1-x)NKN-xLT)with x=2, 4, 5, 6, 7, 8, 10 and 20 mol.% ceramics via solid-state conventional mixed oxide route. The effect of cations substitution of lithium in the A-site and tantalum in the B-site for ($Na_{0.5}K_{0.5}$)NbO_3 (KNN) ceramics were studied. They reported that the morphotropic phase boundary (MPB) between orthorhombic and tetragonal phases were obtained from the solid solution range 5<x<6 mol.% LT. At x=5 mol.%, this sample showed excellent piezoelectric and electromechanical

properties (d_{33}~200 pC/N and k_p~36%). Saito et al. (88, 89) studied the $((K_{0.5}Na_{0.5})_{1-x}Li_x)(Nb_{1-y}Ta_y)O_3$ (KNN-L_xT_y) ceramics with x contents ranging from 0 to 0.2 and y contents ranging from 0 to 0.6. They reported that the sample at x=0.03 and y=0.2 presented the MPB composition, high piezoelectric constant (d_{33}=230 pC/N) and high Curie temperature (T_C=323^{o}C). After that, M. Jiang et al. (90) prepared the $(K_{0.44}Na_{0.52}Li_{0.04})(Nb_{0.94}Ta_{0.1}Sb_{0.06})O_3$ (KNLNTS) lead-free piezoelectric ceramics by the conventional ceramic processing. The powders were calcined at 880^{o}C for 6 h and the pellets were sintered at 1135^{o}C for 3 h. This sample showed pure perovskite structure with orthorhombic phase. For the electrical properties, this samples exhibited high the temperature transition from orthorhombic phase to tetragonal phase (T_{o-t}=115^{o}C), high Curie temperature (T_C=320^{o}C), good dielectric constant at room temperature (εr=1096). However, this sample exhibited poor piezoelectric constant (d_{33}=92 pC/N) and high dielectric loss at room temperature (Tan δ=4.62).

Afterwards, K. Mathrmool et al. (12) were succeed for the fabrication the KNLNTS ceramics by the solid-state combustion method with using glycine as a fuel. The XRD pattern in Figure 34 demonstrated the perovskite phased of KNLNTS powders with different calcined temperature. The pure KNLNTS powder were obtained from samples at calcined temperature of 650-800^{o}C for 2 h. This technique can reduce the calcination temperature ~200^{o}C and dwell time ~4 h when compared with the conventional mix-oxide technique. For KNLNTS ceramics, the XRD pattern presented the coexistent phase between orthorhombic and tetragonal with sintered temperature between 1000 and 1100^{o}C, as showed in Figure 35. At a sintered temperature of 1150^{o}C, the sample was mixed with cubic phase.

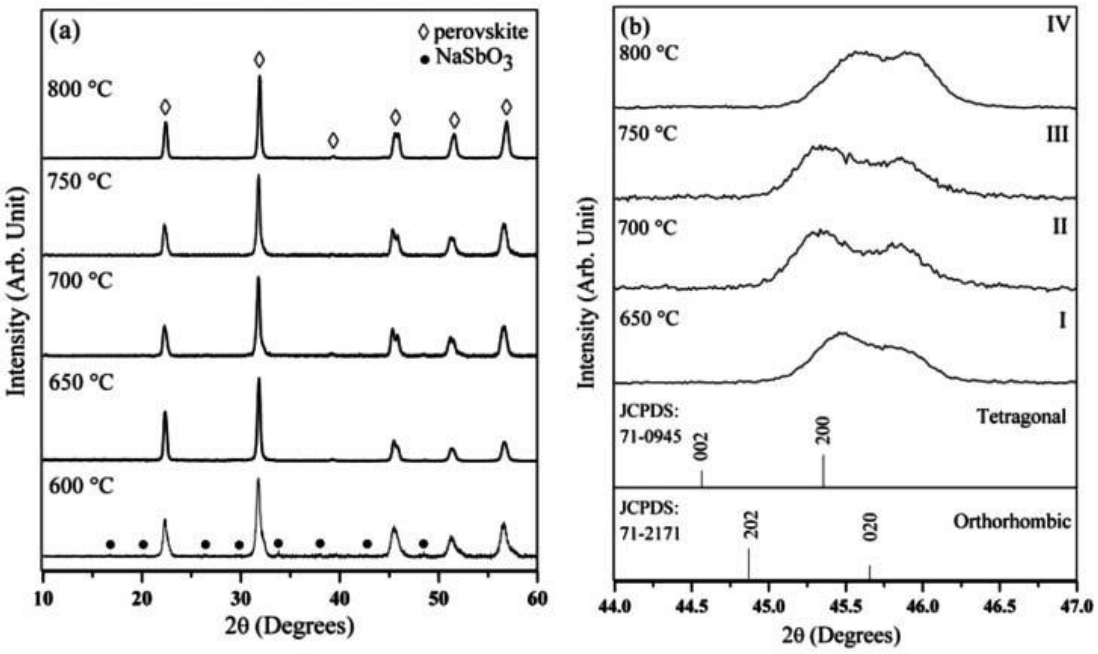

Figure 34 XRD patterns of KNLNTS powders at different calcined temperatures (a) at 2θ between 10º and 60º; (b) at enlarged of 2θ around 45º

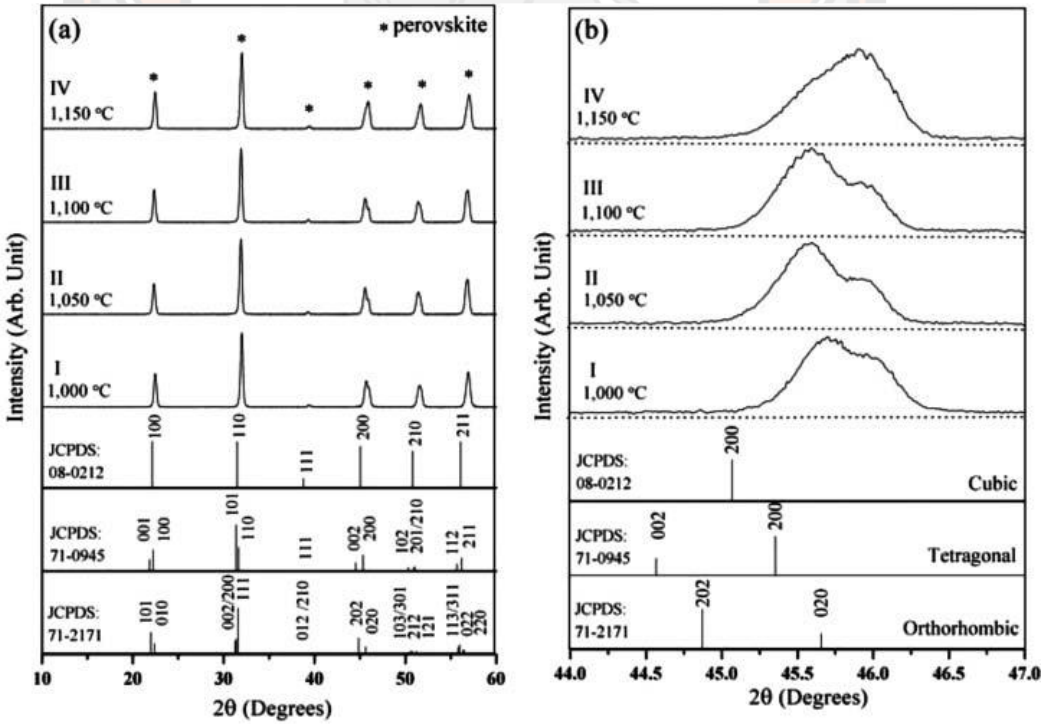

Figure 35 XRD patterns of KNLNTS ceramics at a function of sintering temperatures (a) at 2θ between 10º and 60º; (b) at enlarged of 2θ around 45º (*) perovskite

The microstructure of KNLNTS powders and ceramics were investigated by scanning electron microscopy (SEM) and transmission electron microscopy (TEM) as presented in Figure 36 and 37, respectively. These powders exhibited a rather spherical morphology with a large agglomerated form. The average particle size of all samples was about 0.22 μm. The TEM micrograph of the KNLNTS powder prepared at 650^{o}C for 2 h are exhibited the exact crystalline size about 130 nm. This result confirms that the solid-state combustion technique can synthesize the KNLNTS ultrafine powders. The surface morphology of KNLNTS ceramics sintered at various temperature (1000-1150^{o}C for 2 h) are showed in Figure 36 (d)-(f). the average grain size increased with increasing sintering temperature.

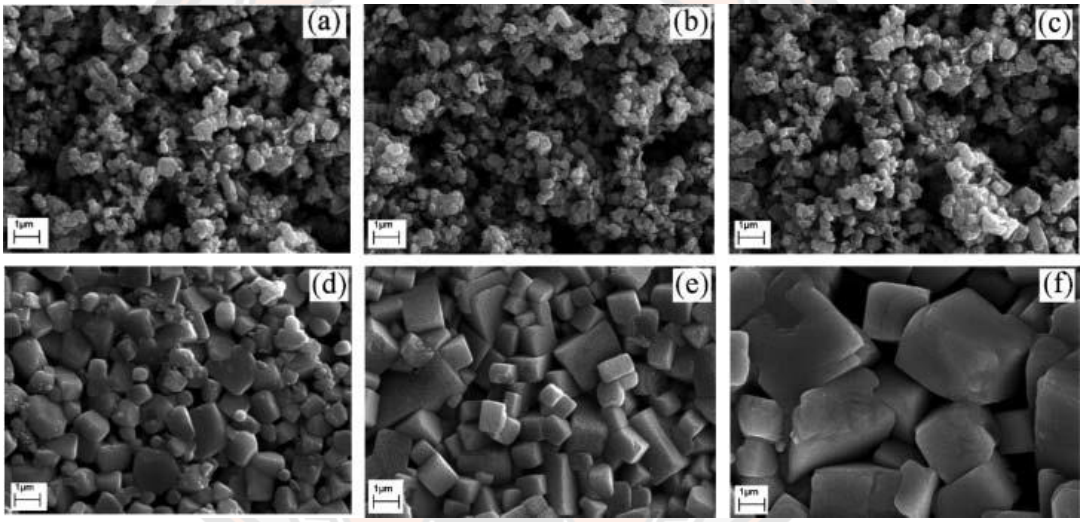

Figure 36 SEM images of the powders calcined at (a) 600^{o}C, (b) 650^{o}C and (c) 800^{o}C for 2 h and the samples sintered at (d) 1,000^{o}C, (e) 1,100^{o}C and (f) 1,150^{o}C for 2 h

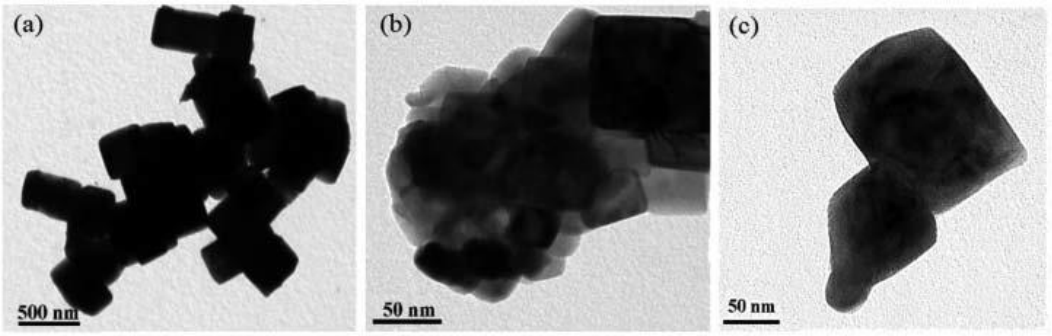

Figure 37 TEM images of KNLNTS powders calcines at 650ºC for 2 h (a) the low magnification image (x18,500), (b) the high magnification image (x195,000) and (c) the very high magnification image (x235,000)

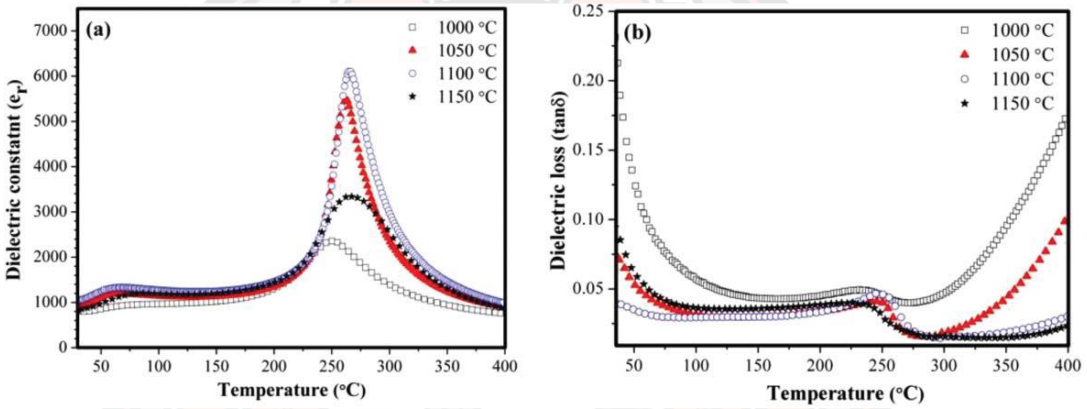

Figure 38 Temperature dependence of (a) dielectric constant and (b) dielectric loss of the KNLNTS ceramics with different sintered temperature measured at 1 kHz

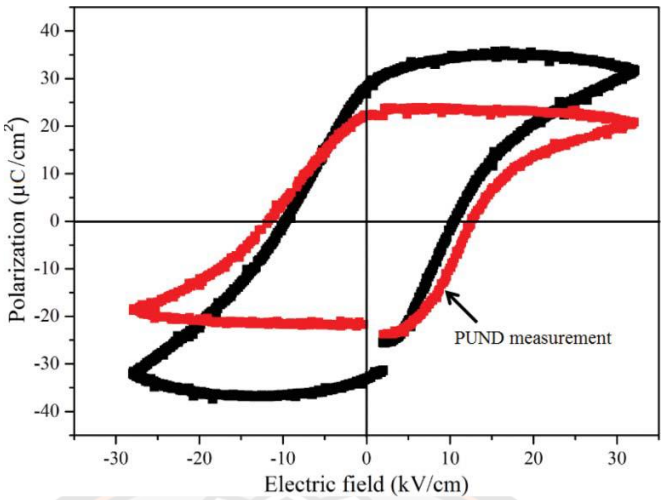

Figure 39 P-E hysteresis loops of KNLNTS ceramics at room temperature

Figure 38 exhibited the temperature dependence of dielectric properties of KNLNTS ceramics with various the sintering temperature. For the dielectric constant (Figure 38 (a)), two dielectric anomalies were observed. The first peak was observed around 60°C which related to the phase transition temperature of orthorhombic ferroelectric phase to tetragonal ferroelectric phase (T_{o-t}). The second peak was observed around 250°C which called Curies temperature (T_C). The T_{o-t} decreased from 70 to 55°C with sintered temperature increased from 1000 to 1100°C and then increased, while T_C continuously increased with sintered temperature increased. The dielectric constant at room temperature (ε_r) and maximum dielectric constant at T_C (ε_m) tended to increase with sintering temperature increased and then dropped. The sample sintered at 1100°C exhibited the densest ceramic, the highest dielectric constant, excellent ferroelectric properties and piezoelectric coefficient (D=4.42 g/cm^3, ε_m= 6114, P_r=30.63 μC/cm^2, E_c=8.56 kV/cm and d_{33}=203 pC/N).

Barium Titanate ($BaTiO_3$; (BT)) ceramics

Barium titanate ($BaTiO_3$) is very important and has been extensively exploited both for academic science and for technological utilization over the past decades. BT has a perovskite crystalline structure presented in Figure 40 with Ba^{2+} ions to the vertices, O^{2-} ion to face center and Ti^{4+} ion in a body centered position. Above Curie temperature (~130°C), the lattice structure of the unit cell is cubic which is no

spontaneous polarization. While, below Curie temperature, the lattice structure stats distorting and changes from cubic crystal structure to the tetragonal crystal structure which is occurred spontaneous polarization. Moreover, the other transformation of BT ceramic is occurred at temperature close to 0^{o}C and -80^{o}C. Below 0^{o}C, the lattice structure is orthorhombic whereas below -80^{o}C it exhibits rhombohedral crystal structure with polar axis along body diagonal as presented in Figure 41. In this case, the polarization arises from the shift of axially elongated Ti^{4+} ions crystal in the unit cell which this type of polarization occurs without any application of external electric field or pressure.

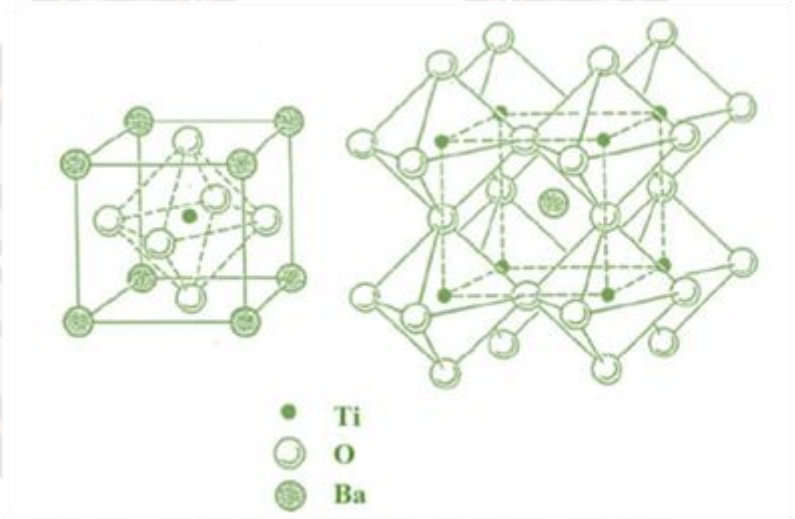

Figure 40 the perovskite ABO3 unit cell for cubic BaTiO3 ceramic (91)

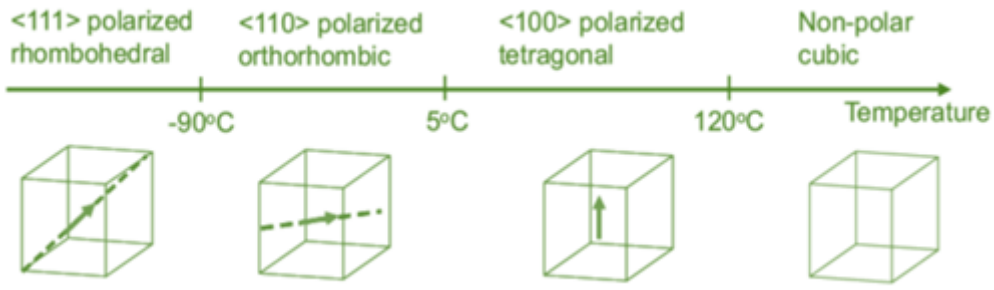

Figure 41 the structure transformation of $BaTiO_3$ (4)

BT ceramics are very important lead-free piezoelectric ceramic and widely studied owing to its show high dielectric constant, low dielectric loss and excellent piezoelectric coefficient (4, 91). However, BT ceramics has relatively low T_C which limits its use as high-power transducers and low electromechanical coupling factor when compared with PZT ceramics. Thus, low Tc is the big disadvantage of pure barium titanate because the high-temperature coefficient of capacitance near the Curie temperature. At Curie temperature of BT ceramics, the phase transition from the tetragonal to the cubic phase occurs which led to restricts the temperature range of application. To improve the electrical properties of BT ceramics, the co-doping of Ca^{2+} and Zr^{4+} in system was earlier applied in capacitor composition (92, 93).

D. Hennings and H. Schreinemacher (92) prepared the $Ba_{1-x}Ca_x(Ti_{1-y}Zr_y)O3$ ceramics by mixed oxide technique. The powders were calcined at temperature of 1200^{o}C and the pellets were sintered at temperature of 1430^{o}C for 15 h. They reported that the reduction of ε may cause from the second phase of $CaTiO_3$. After that, Pan Wang et al. (93) studied effect of firing temperature on phase formation, microstructure and electrical properties of $(Ba_{0.85}Ca_{0.15})(Ti_{0.90}Zr_{0.10})O_3$ piezoelectric ceramic by conventional oxide-mixed method. The powders were obtained from calcined temperature of 1300^{o}C for 2 h. The excellent properties of d_{33}=650 pC/N, d_{31}=74 pC/N, K_p=0.53, k_t=0.38, k_{31}=0.309, $s_{11}^E = 14.0\times10^{-12}$ m^2/N, ε_r=4500, tan δ=0.009, TC=85^{o}C, P_r=11.69 μC/cm^2 and E_c=190 V/mm were obtained from the sintered sample at temperature of 1540^{o}C. Another point of interest in piezoelectric ceramics is the preparation technique, which is one of the main factors for production of high-quality lead-free piezoelectric ceramics. Recently, C. Kornphom et. al (16) fabricated the $Ba_{0.85}Ca_{0.15}Ti_{0.90}Zr_{0.10}O_3$ ceramics by the combustion technique. The powders were calcined at temperature in the range of 900 to 1200^{o}C for 2 h. At low calcined temperature (900-1000^{o}C), the impurities phases were observed as shown in Figure2.35. The single orthorhombic perovskite phase of the BCTZ powders was obtained from the specimens calcined at ≥1050^{o}C for 2 h (Figure 42). Figure 43 presented the X-ray patterns of BCTZ ceramics as a function of sintering temperature. All specimens exhibited the coexistent of a rhombohedral and orthorhombic phases.

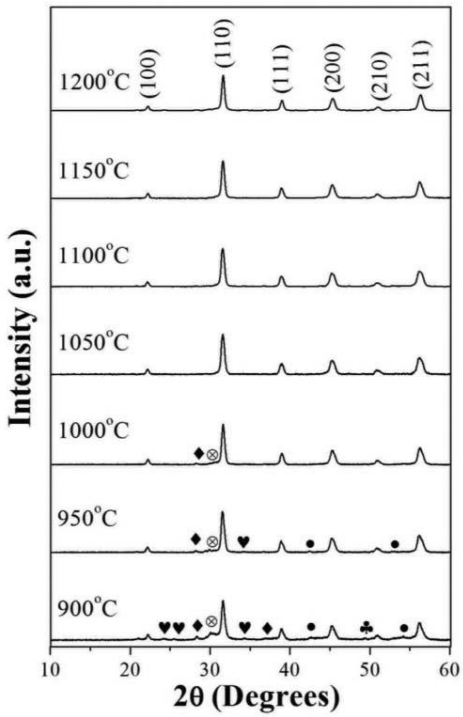

Figure 42 X-ray diffraction patterns of BCTZ powders calcined between 900 and 1200ºC for 2 h. (♣) $BaCO_3$, (♥) $BaZrO_3$, (●) $BaTiO_3$, (⊗) CaO and (♦) TiO_2

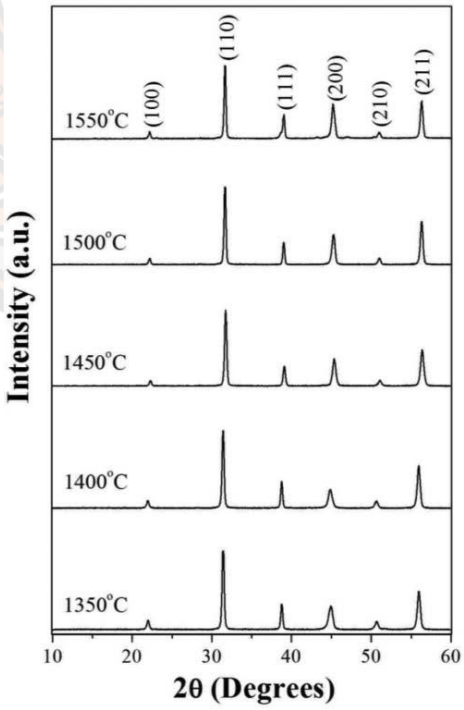

Figure 43 X-ray diffraction patterns of BCTZ ceramics sintered at different temperature

SEM images of BCTZ powders calcined at a temperature between 900 and 1200^{o}C for 2 h show in Figure 44 (a)-(c). It was found that the powders consisted of fine particles with a large agglomerated form. The average particle size increased with the calcination temperature increased. For the BCTZ sintered samples at various temperature is shown in Figure 44 (d)-(f). The grain morphology presented a cornered cubic shape and the average grain size increased with the increase of sintering temperature.

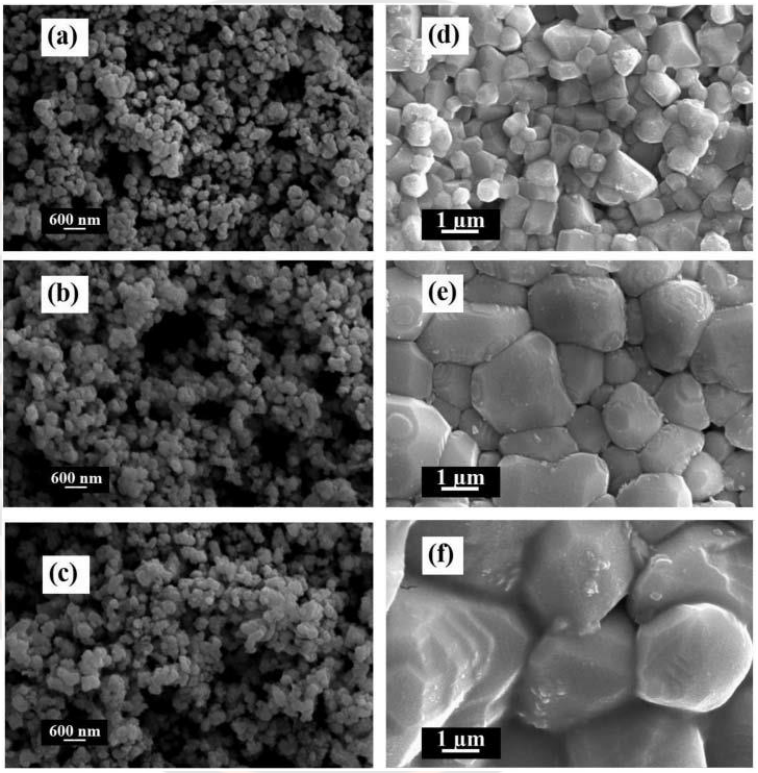

Figure 44 The SEM micrographs of BCTZ powders calcined at: (a) 900, (b) 1050, (c) and (d) 1200^{o}C and the pellets surface sintered at: (d) 1350, € 1450 and (f) 1550^{o}C for 2 h

For the electrical properties of BCTZ ceramics at different sintered temperature, the dielectric curve showed two peaks in all samples, which related to the phase transition temperature of the coexistence of the rhombohedral and orthorhombic ferroelectric phase to the tetragonal ferroelectric phase (T_p) at ~45^{o}C and the tetragonal ferroelectric phase to the cubic paraelectric phase (T_c) at ~93^{o}C, respectively as seen in Figure 45. It was found that the T_p and T_c shifted to lower

temperature with increasing sintering temperature. The dielectric constant at room temperature (ε_r) and the maximum dielectric at T_C (ε_{max}) increased with increasing sintering temperature up to 1450°C and then dropped. Figure 46 exhibited the P-E loops of BCTZ ceramics at various sintered temperatures. All samples demonstrated a slim and saturated P-E loops. The remnant polarization (P_r) increased from 7.66 $\mu C/cm^2$ to 18.47 $\mu C/cm^2$ when the sintering temperature increased from 1350°C to 1450°C. while, the coercive field (Ec) tended to increased.

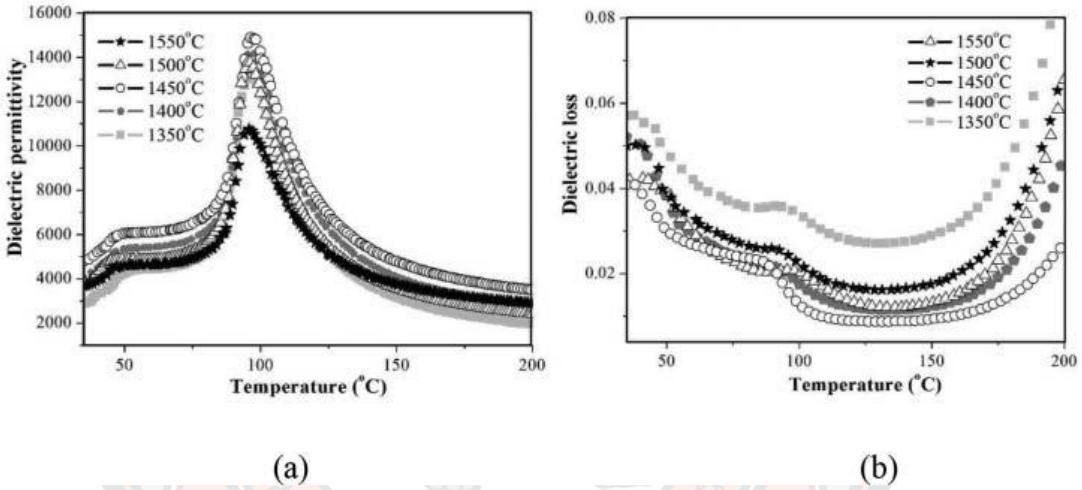

Figure 45 temperature dependence of dielectric properties of BCTZ ceramics sintered at various temperatures

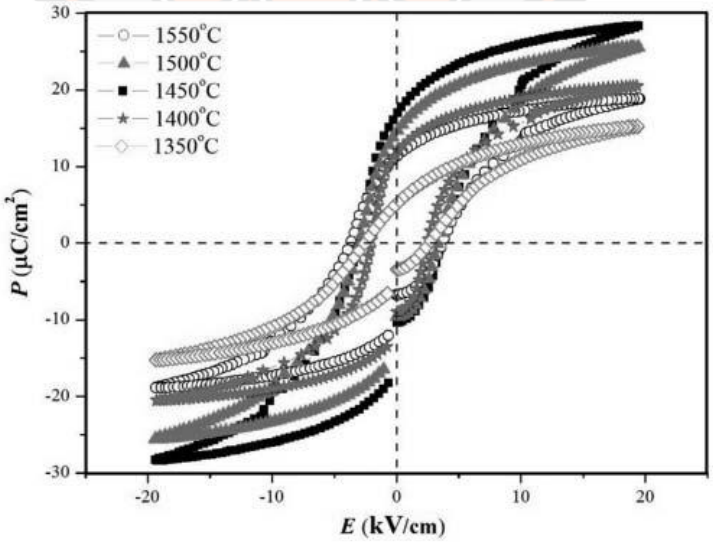

Figure 46 P-E hysteresis loops of BCTZ with difference sintered temperature

Bismuth ferrite base ceramics ($BiFeO_3$; BFO)

BFO ceramics are of main interest because their multiferroic material. It is shown magnetic order (T_N=634 K) and ferroelectric order (ferroelectric transition temperature T_C FE=1103 K) at room temperature. BFO ceramics exhibit a rhombohedral perovskite structure with R3c space group. The lattice parameters are a=5.6343 Å and a=59.438° with ferroelectric polarization along the [111] axes (94). Bi^{3+} is on a 12-fold coordinated, cubo-octahedral A site and Fe^{3+} on a 6-fold coordinated octahedral B-site (95, 96). The tolerance factor of BFO is 0.88 which is calculated by Shannon radii (97). It is well known that the t<1 the oxygen octahedral has to tilt in order to fit into the unit cell. This tilt of the BFO system is $a^-a^-a^-$ indicating an antiphase rotation of FeO6 octahedral along $[111]_{psudocubic}$ axis, as seen in Figure 47. At room temperature, BFO is an obvious choice for application. The polarization of BF is reported to be vary high (ca. 90-100 $\mu C/cm^2$) (98, 99). However, BFO is high leakage current which affects the measurement of dielectric/ferroelectric properties. The high leakage current of BFO is descripted to oxidation reduction of Fe ions ($Fe^{2+} \rightarrow Fe^{3+} + e^-$) which led to the creation of oxygen vacancies for charge compensation (22, 100).

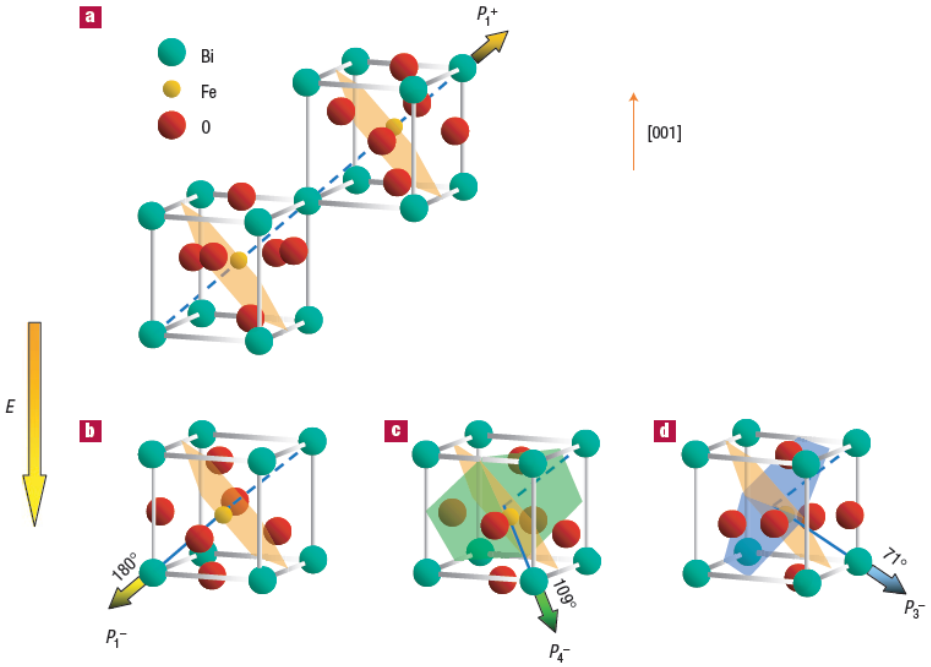

Figure 47 Schematic diagram of BFO crystal structure, with polarisation along [111] axis indicated by bold arrow (22)

Improvement in the properties of BFO ceramics, the doping of BFO in A-site has been wildly studied such as Ca, Sr and Ba and reported to exhibited enhanced magnetization (24, 25, 27). C. Yang et. al (27) prepared the Bi1-xBaxFeO3 (BBFO) with x=0.05, 0.10, 0.15, 0.20, 0.25 and 0.30 by a sol-gel method. They reported that the Ba substitution for Bi in BFO led to change the structure of the nanocrystalline from rhombohedral to tetragonal as seen in Figure 48. Figure 49 exhibits the variation of dielectric constant and loss of BBFO samples as a function of frequency (f). The dielectric constant of BBFO increased while the dielectric loss decreased with x content increased from 0.05 to 0.15. For magnetic properties, the M-H hysteresis loops of BBFO at room temperature are shows in Figure 50. the remnant magnetization increased with Ba content increased. At x=0.20, this sample exhibited the coexistence phase between rhombohedral and tetragonal, the highest dielectric constant and the lowest dielectric loss.

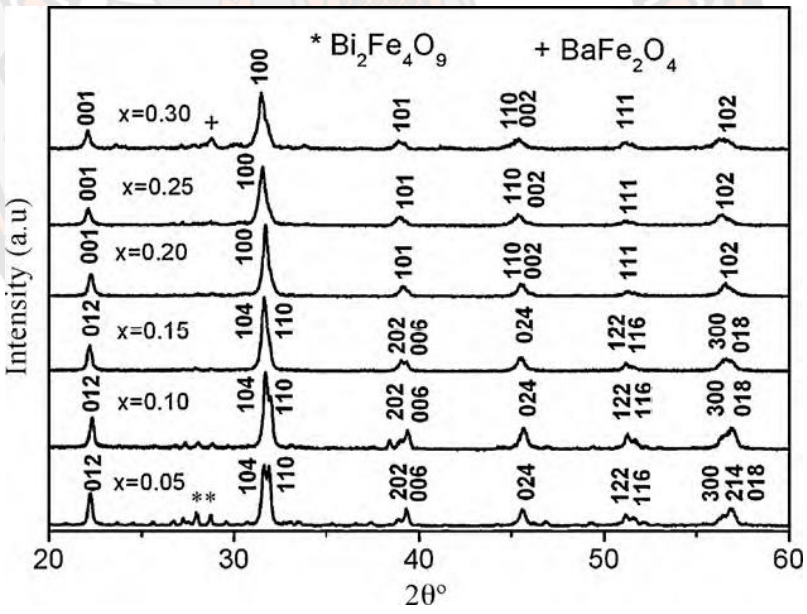

Figure 48 XRD patterns of BBFO samples with difference x content

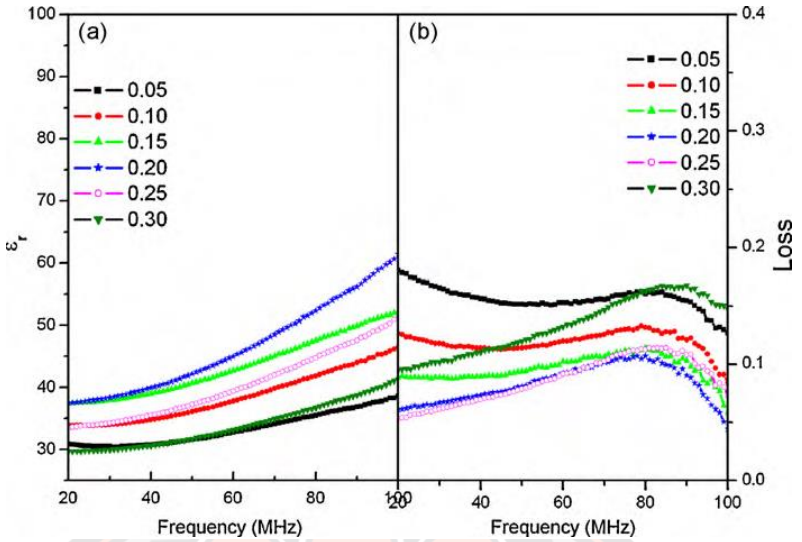

Figure 49 Frequency dependence of (a) the dielectric constant and (b) loss for BBFO nanocrystalline at RT

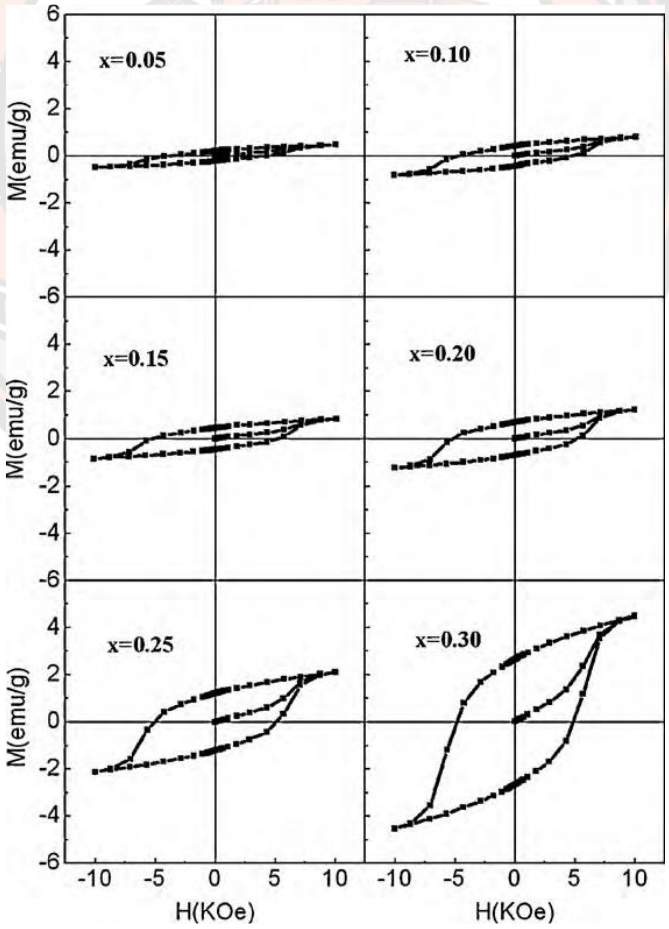

Figure 50 M–H hysteresis loops of BBFO nanocrystalline at RT

The binary systems of multiferroic material.

(1-x)BNT-x$BiFeO_3$ (BNT-BFO) ceramics preparation via the conventional solid-state reaction were investigated by K. H. Ryu et. al (29). Figure 51 showed X-ray diffraction patterns of BNT-BFO samples. All ceramics showed the pure perovskite with on secondary phase. The maximum dielectric constant was observed at 322°C assigned to be T_C or T_m which T_m increased from 322°C to 396°C. The summarization of the effects of BF in BNT were showed in Figure 52. The highest d_{33} value were obtained from the sample with 5 mol% doping while the highest k_p value were obtained from the sample with 2 mol% doping. It was found that the doping BFO can improved the piezoelectric properties of BNT ceramics.

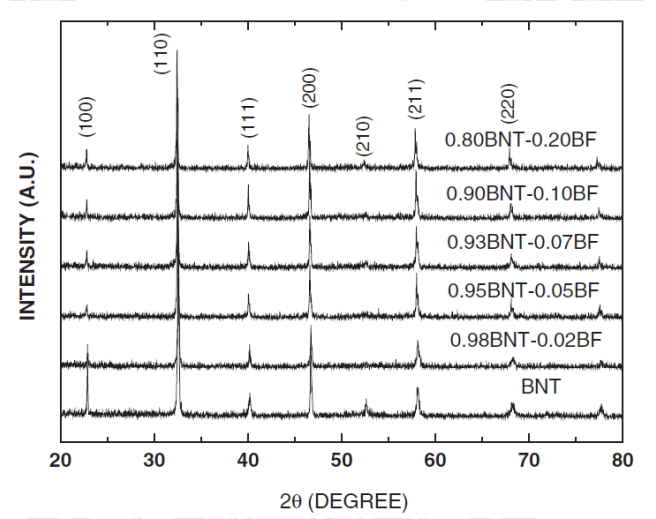

Figure 51 XRD patterns of BNT-BF systems

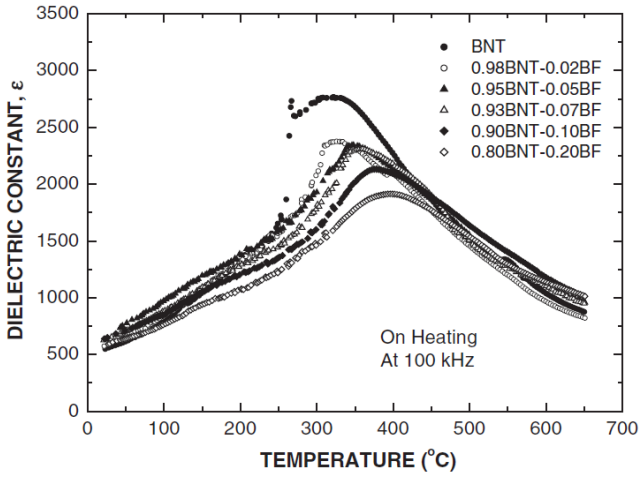

Figure 52 Temperature dependences of dielectric constant of BNT-BF systems

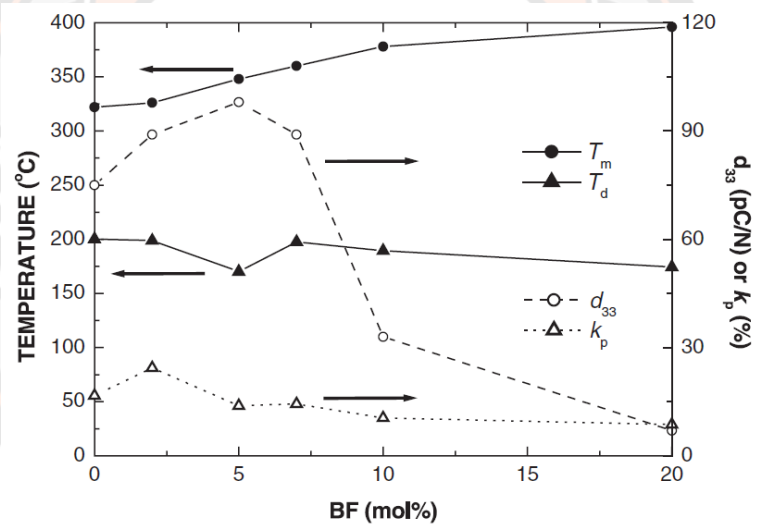

Figure 53 Transition temperatures and piezoelectric properties as functions of BF concentration

Recently, K. Kaswan et. al (32) studied (1-x)$Na_{0.5}Bi_{0.5}TiO_3$-x$Bi_{0.8}Ba_{0.2}FeO_3$ ceramics with $0 \leq x \leq 0.4$ by solid state reaction technique. All samples demonstrated pure perovskite with rhombohedral symmetry (space group R3c), as shown in Figure 54. With the increase of BBFO content, the main peak shifts to lower angle, indicating enhancement in the dimension of unit cell. Due to the larger ionic radii of Ba^{2+} and Fe^{3+} ions as compared to Bi^{3+}/Na^{+} and Ti^{4+} ions, respectively. After that, the magnetic properties were investigated. They reported that the magnetic hysteresis

loops for x≤0.10 exhibited a linear magnetization with narrow hysteresis loop, indicating the typical antiferromagnetic nature (AFM). For sample with 0.20≤x≤0.40, the magnetic hysteresis loops were observed which the remnant magnetization and coercive field continuously increased, as seen in Figure 55.

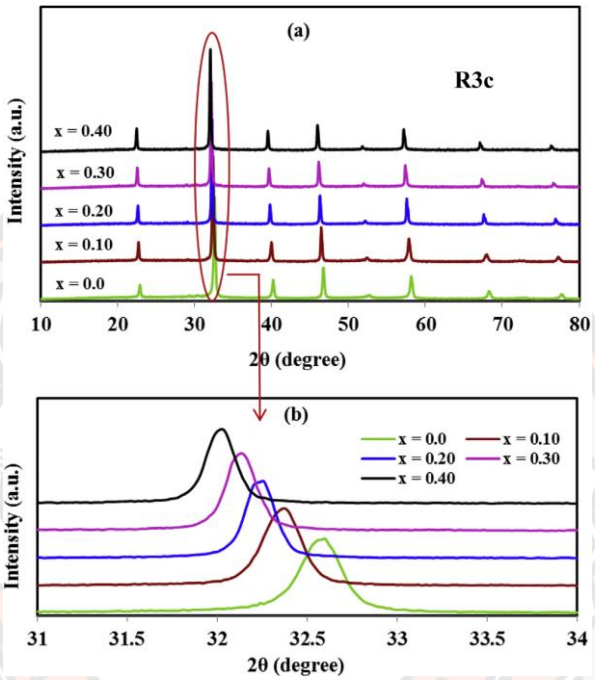

Figure 54 XRD patters of (1-x)BNT-xBBFO ceramics

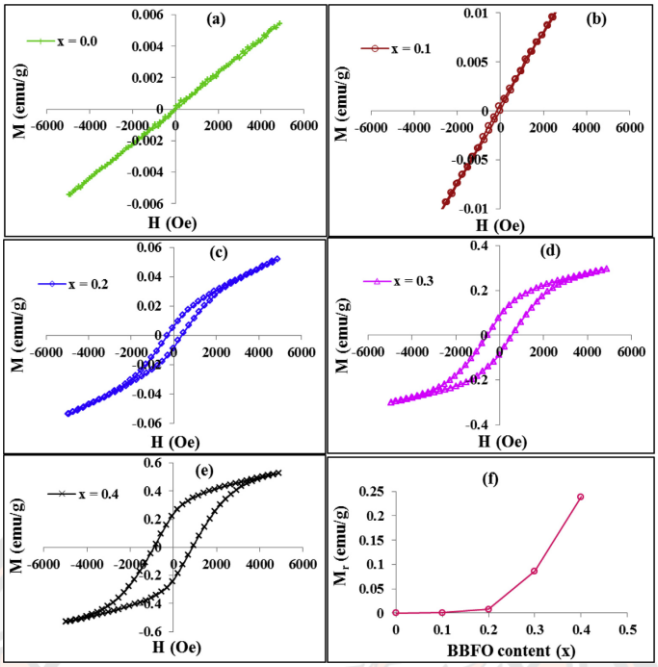

Figure 55 (a)-(e) Magnetic hysteresis loops for (1-x)$Na_{0.5}Bi_{0.5}TiO_3$-x$Bi_{0.8}Ba_{0.2}FeO_3$; x=0.0, 0.10, 0.20, 0.30 and 0.40 ceramics recorded at room temperature (f) concentration (x) dependence of remnant magnetization (M_r)

CHAPTER III

RESEARCH METHODOLOGY

This chapter explained about the fabrication and characterization of

1. The binary system of BNKLT-xBFCO ceramics
2. The binary system of (1-x)BNKLT-xBBF ceramics
3. The binary system of (1-x)KNLNTS-xBBF ceramics
4. The binary system of (1-x)BCTZ-xBBF ceramics

All samples were fabricated by the solid state combustion technique. The information of the detail fabrication and characterization are present in next section.

The binary system of BNKLT-xBFCO ceramics

$Bi_{0.5}(Na_{0.77}K_{0.20}Li_{0.03})_{0.5}TiO_3$-xmol%$Bi_2FeCrO_6$ (BNKLT-xBFCO) with x=0-0.019 ceramics were fabricated using the solid-state combustion method. $Bi(NO_3)_3 \cdot 5H_2O$, $NaNO_3$, KNO_3, Li_2CO_3, TiO_2, $Fe(NO_3)_3 \cdot 9H_2O$ and $Cr(NO_3)_3 \cdot 9H_2O$ were used as the raw material. All the raw materials were weighed according to the formulation and ball milled in ethanol for 24 h. After drying, the powders were mixed with glycine at a ratio of 1:0.238 and calcined at 750^oC for 2 h [9]. The calcined powders were mixed with 3wt% polyvinyl alcohol (PVA) and ball milled again for 12 h. After that, the mixed solution was dried and pressed into disks of 15 mm in diameter by a pressure of 80 MPa. The green pellets were sintered at a temperature of 1150^oC for 2 h. The phase structure of all samples was checked using X-ray diffraction (XRD, Philip PW 3040/60 X'Pert Pro). A scanning electron microscope (SEM, Leo 1455VP) was used to investigate the surface morphology of these samples, which were polished and thermally etched in air below the sintering temperature by 100^oC for 20 min. The density of the samples was measured by Archimedes' method. To measure the electrical properties, the sintered samples were coated with silver paste on both surfaces and fired at 600^oC for 30 min in order to form electrodes. The temperature dependence behavior of the sintered samples at 1, 10 and 100 kHz was measured by an LCR meter (HP, 4284A). The piezoelectric

constant (d_{33}) was measured by a quasi-static d_{33}-meter (Sinocera, YE2730A). The ferroelectric property was obtained using a computer-controlled modified Sawyer-Tower circuit (Radiant, PLC2-The P-E loop). The magnetic properties was observed with a vibrating sample magnetometer (Versa Lab, Quantum Design).

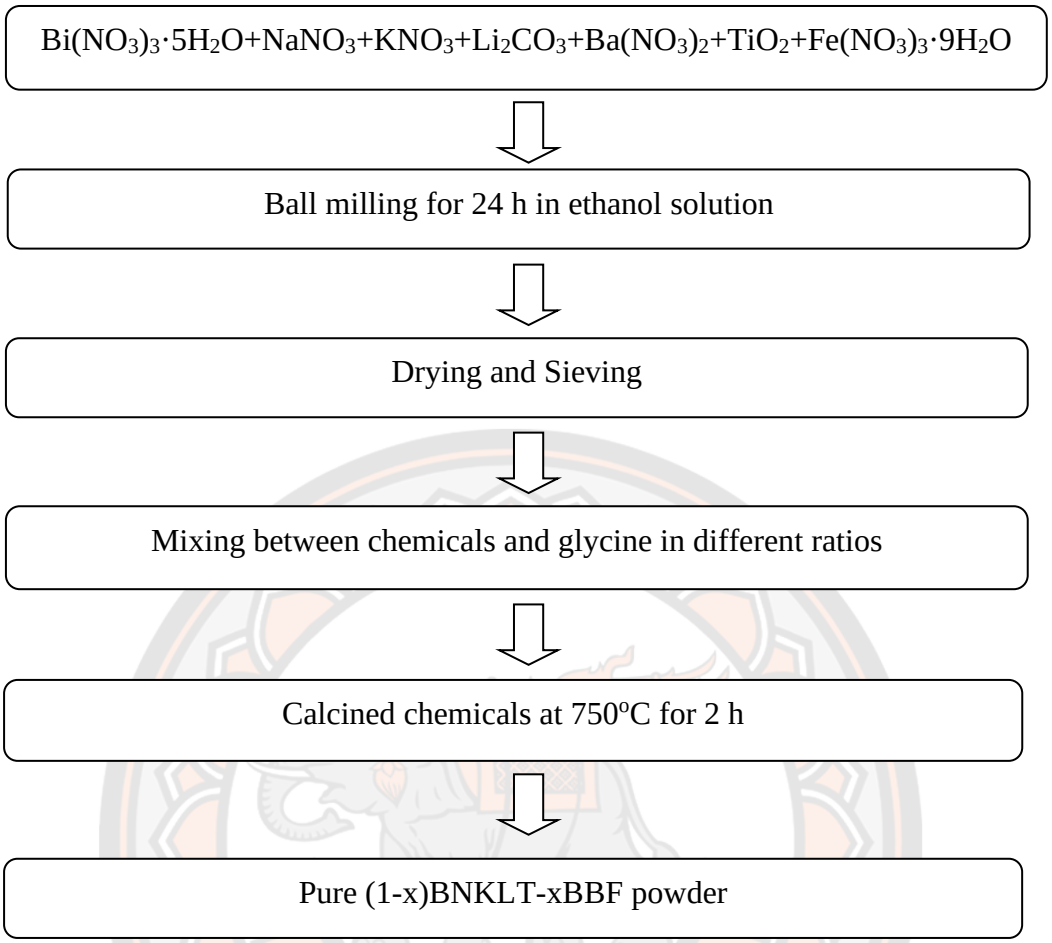

Figure 56 Flowchart of BNKLT-xBFCO powder preparation using combustion method

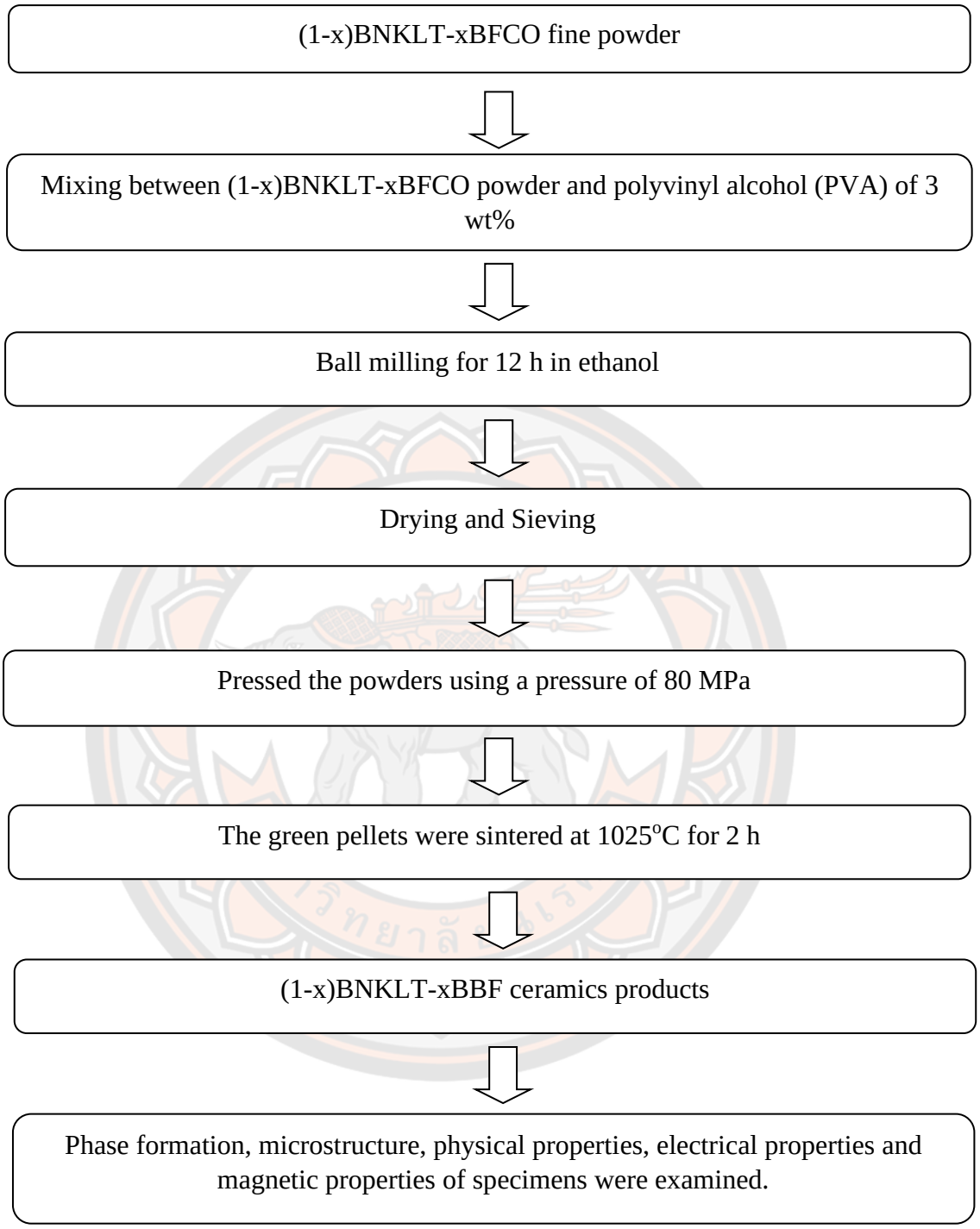

Figure 57 Flowchart of BNKLT-xBFCO ceramics preparation using combustion method

The binary system of (1-x)BNKLT-xBBF ceramics

$Bi(NO_3)_3 \cdot 5H_2O$, $NaNO_3$, KNO_3, Li_2CO_3, $Ba(NO_3)_2$, TiO_2 and $Fe(NO_3)_3 \cdot 9H_2O$ were used as raw materials. The nitrates oxides and carbonates chemical powders were dried in an oven at 120°C for 8 h before weighting. Then, all weighed powders were mixed by using ball-milling technique with stabilized zirconia balls for 24 h in ethanol solution. The mix powder were dried on a hot plate with magnetic stirring and then, baked at 120°C for 6 h in oven. After that, the dried powder were mixed with glycine ($C_2H_5NO_2$) with calculated by the concept of propellant ratio. The propellant chemistry are the ratio between the metal nitrates (oxidizing agent) and fuel (reducing agent). The name and valence of elements for oxidizing agent and reducing agent, including Bi = +3, N = 0, O = -2, H = 1, Na = +1, K = +1 Ba=+2 and Fe = +3 have been considered to calculate for combustion technique. The total oxidizing valences of $Bi(NO_3)_3 \cdot 5H_2O$, $NaNO_3$, KNO_3, $Ba(NO_3)_2$ and $Fe(NO_3)_3 \cdot 9H_2O$ are -15, -5, -5, -10 and -15 respectively. For the total reducing valences of glycine ($C_2H_5NO_2$) is -9. So, the quantity of glycine was obtained from the calculation by moles and valences of an oxidizing agent and the reducing agent which the BNKLT powder were mixed with glycine in the ratio of 1:1.10278 mole. The calculation of glycine quantity was obtained from the equation (16)

$$(0.5\times15) + (0.385\times5) + (0.1\times5) / 9 = 1.10278 \text{ mole} \quad (16)$$

In other composition, the glycine quantity would be increased with x increasing according to the equation (17)

$$(0.5\times15) + (0.385\times5) + (0.1\times5) + (x\times10) + (x\times15) / 9 = y \quad (17)$$

When y is the glycine quantity in mole unit.

After drying, the mixed powders were mixed with glycine in an agate mortar and then calcined at 750 °C for 2 h (8). Next, the calcined powders were mixed with polyvinyl alcohol (PVA) of 3% and ball milled again for 12 h in ethanol solution. After that, the mix solution was dried, then crushed and sieved to obtained fine powder. Finally, the mixture powders were molded at a pressure of 80 MPa in a diameter mild and all pellets were sintered at 1025°C for 2 h in air (8). For characterization of all ceramics, phase formation of all composition samples was characterized by using an X-ray diffraction (XRD) analysis (XRD, X'pert MPD 3040, Phlips, Netherland). The microstructure of all samples were observed by a scanning

electron microscope (SEM, Leo1455VP). The average grain size were determined by using the linear interception method. Density of the sintered samples were measured by the Archimedes method. Dielectric constant and dielectric loss of all composition samples were measured by using a LCR meter (Agilent 4263B) at temperature in the range of 30 ºC to 400 ºC with different frequencies (1, 10 and 100 kHz). The computer-controlled modified Sawyer-Tower circuit (Radiant, PLC2-The P-E loop) was used to measure the ferroelectric properties at room temperature. The electric field vs strain curve (S-E curve) were obtained from an optical displacement sensor (Fotonic sensor, MTI-2100) combined with a Radiant ferroelectric test system. Magnetic property was observed by a vibrating sample magnetometer (Versa Lab, Quantum Design). Figure 59 and 60 presented the flowchart of (1-x)BNKLT-xBBF powders and ceramics fabrication, respectively.

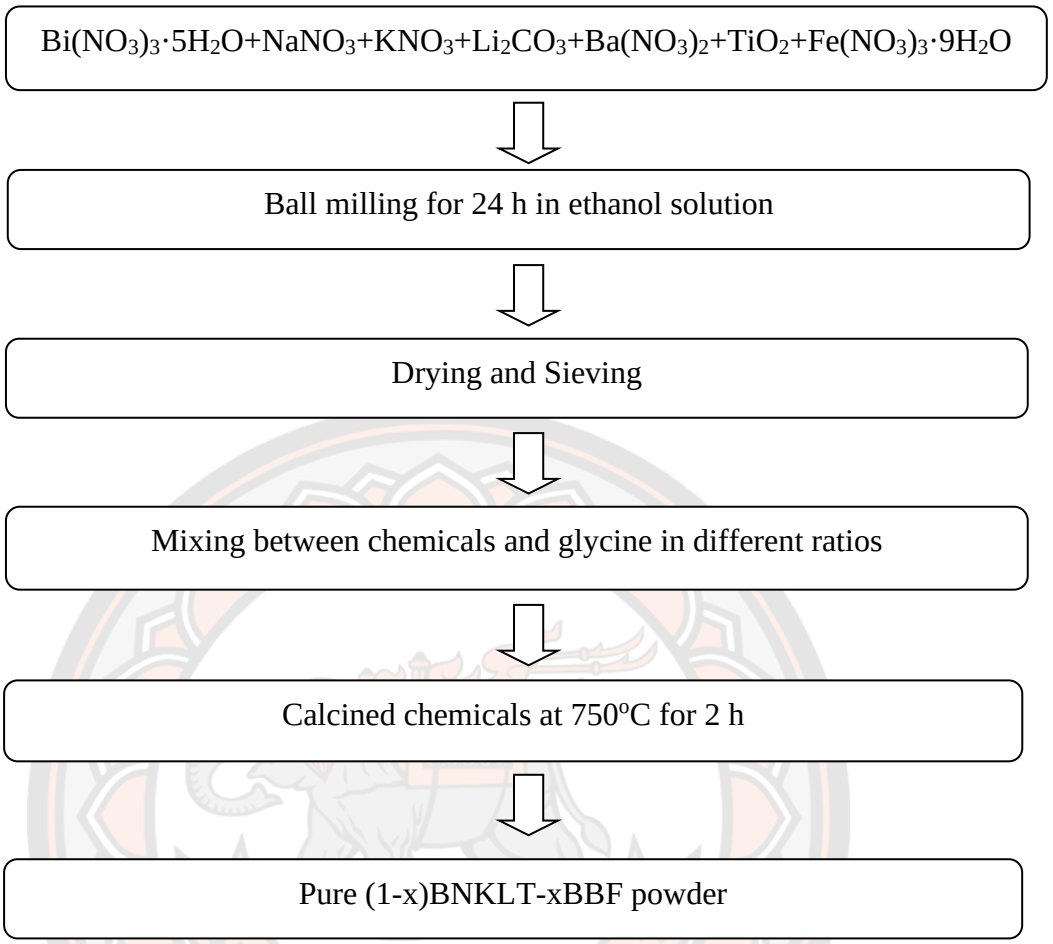

Figure 58 Flowchart of (1-x)BNKLT-xBBF powder preparation using combustion method

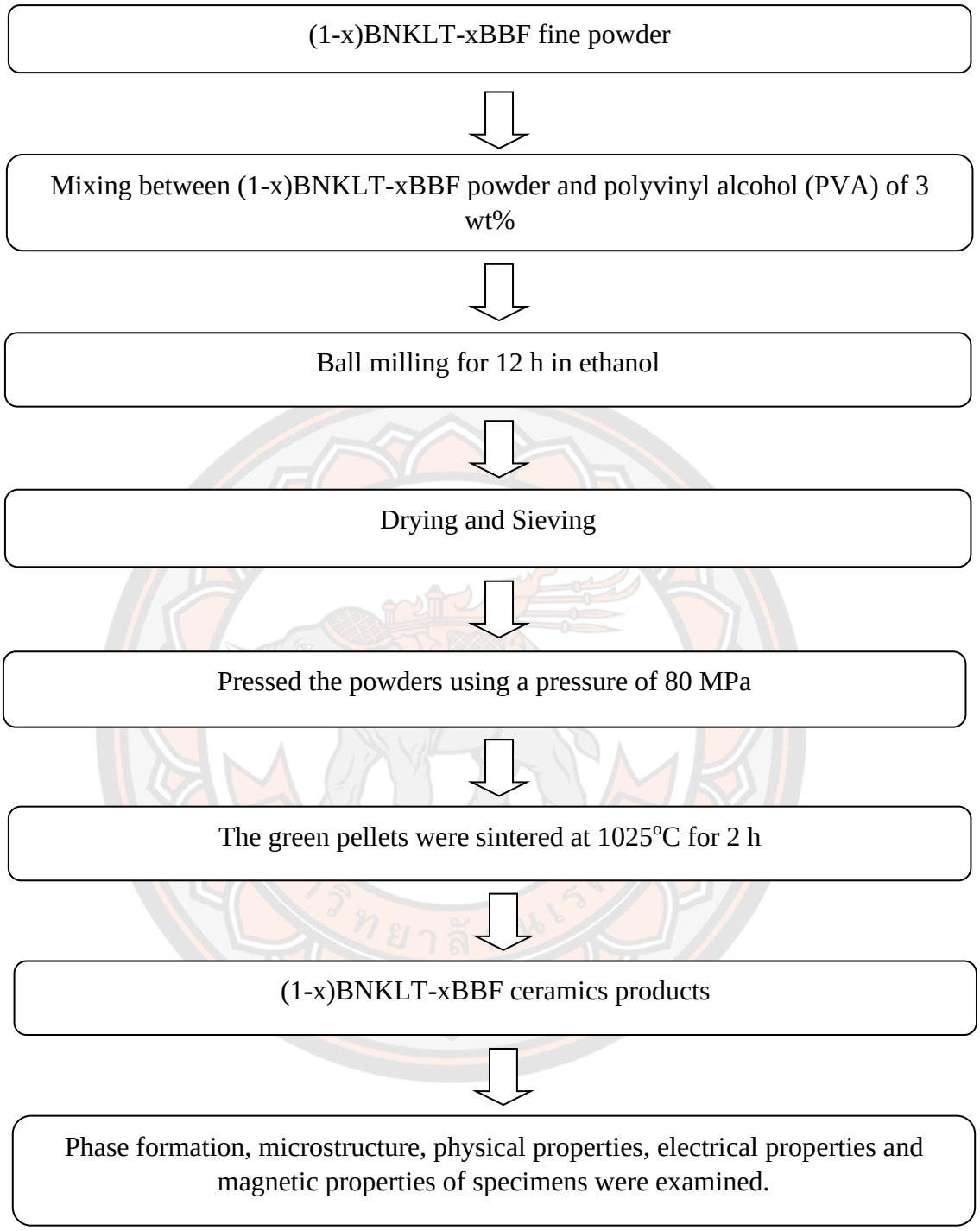

Figure 59 Flowchart of (1-x)BNKLT-xBBF ceramics preparation using combustion method

The binary system of (1-x)KNLNTS-xBBF ceramics

(1-x)KNLNTS-xBBF ceramics with x=0-0.4 were prepared by the solid-state combustion technique using $KHCO_3$, $NaNO_3$, Li_2CO_3, Nb_2O_5, Ta_2O_5, Sb_2O_3, $Bi(NO_3)_3*5H_2O$, $Ba(NO_3)_2$ and $Fe(NO_3)_3*9H_2O$ as starting materials. Each ingredient was weighed according to the stoichiometric ratio and then ball milled for 24 h using ethanal as a grinding media. The mixtures were dried, sieved and mixed with glycine in a ratio of 1:2 by weight (12). The mixed powders were calcined at 650^oC for 2 hours (12). The calcined powders were mixed with 3% polyvinyl alcohol (PVA) as the binder and then ball milled again for 12 hours. The dried powders were pressed into disks, 15 mm in diameter and 2 mm in thickness under 80 MPa. The green pellets were sintered at 1100^oC for 2 hours and the the binder was burnt out at 600^oC for 1 hour (12). The phase structure was analyzed by the X-ray diffraction (XRD, Bruker D2 PHASER) for all the samples. The XRD data was analyzed with Rietveld refinement using the Fullprof program. To observe the microstructure using scanning electron microscope (SEM, Leo1455VP), the sintered samples were polished and thermally etched at 1000^oC for 15 minutes. The determine the average grain size, the linear interception method was used on more than 300 grains. The density of all samples was evaluated by Archimedes' method. To characterize the electrical properties, the sintered samples were polished, coated on both sides with silver paste and fired at 500^oC for 30 minutes. The dielectric properties were measured in the temperature range between 30 and 400^oC. The polarization-electric field (P-E) hysteresis loops were studied at room temperature, using a computer-controlled modified Sawyer-Tower circuit. The magnetic properties was measured by a vibrating sample magnetometer (Versa Lab, Quantum Design).

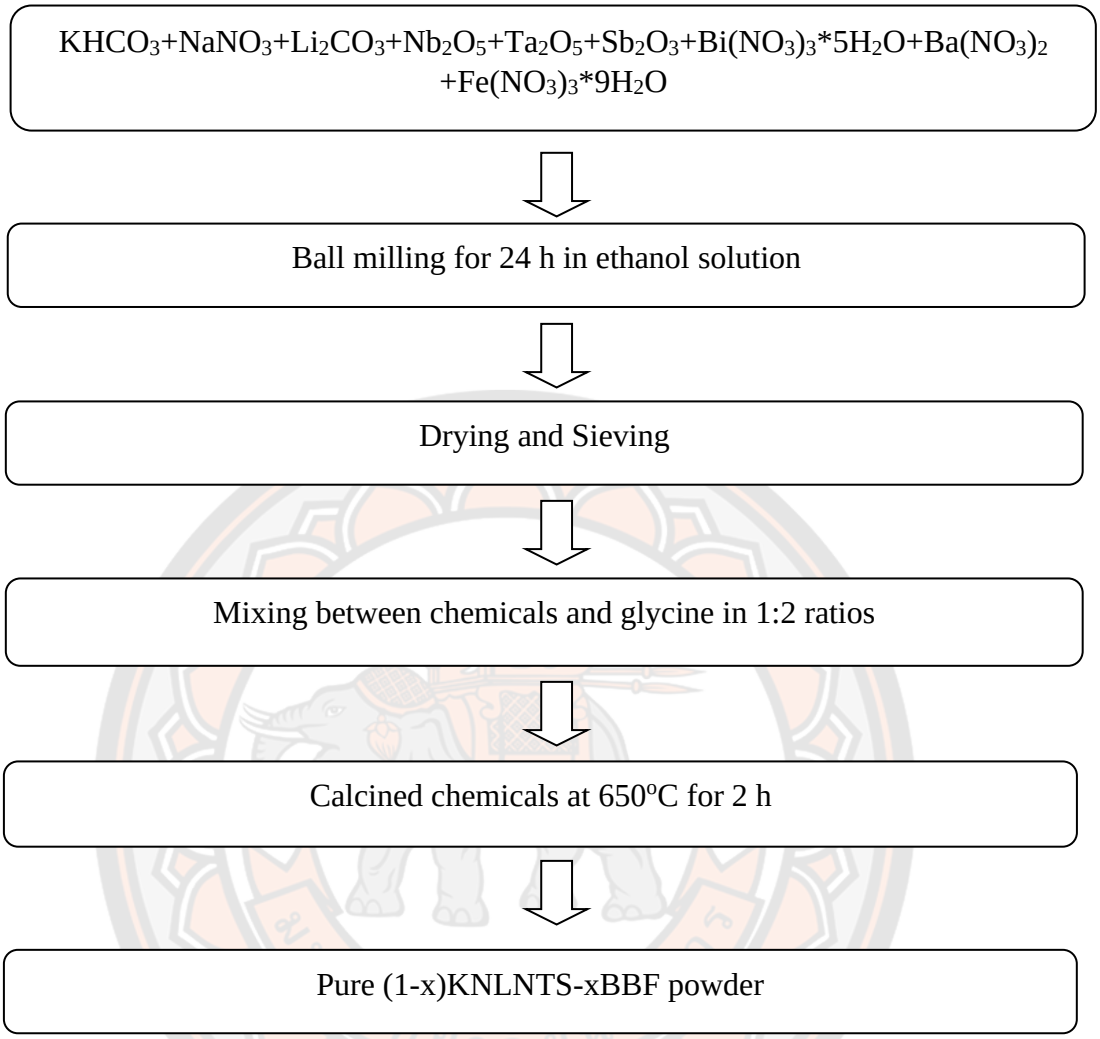

Figure 60 Flowchart of (1-x)KNLNTS-xBBF powder preparation using combustion method

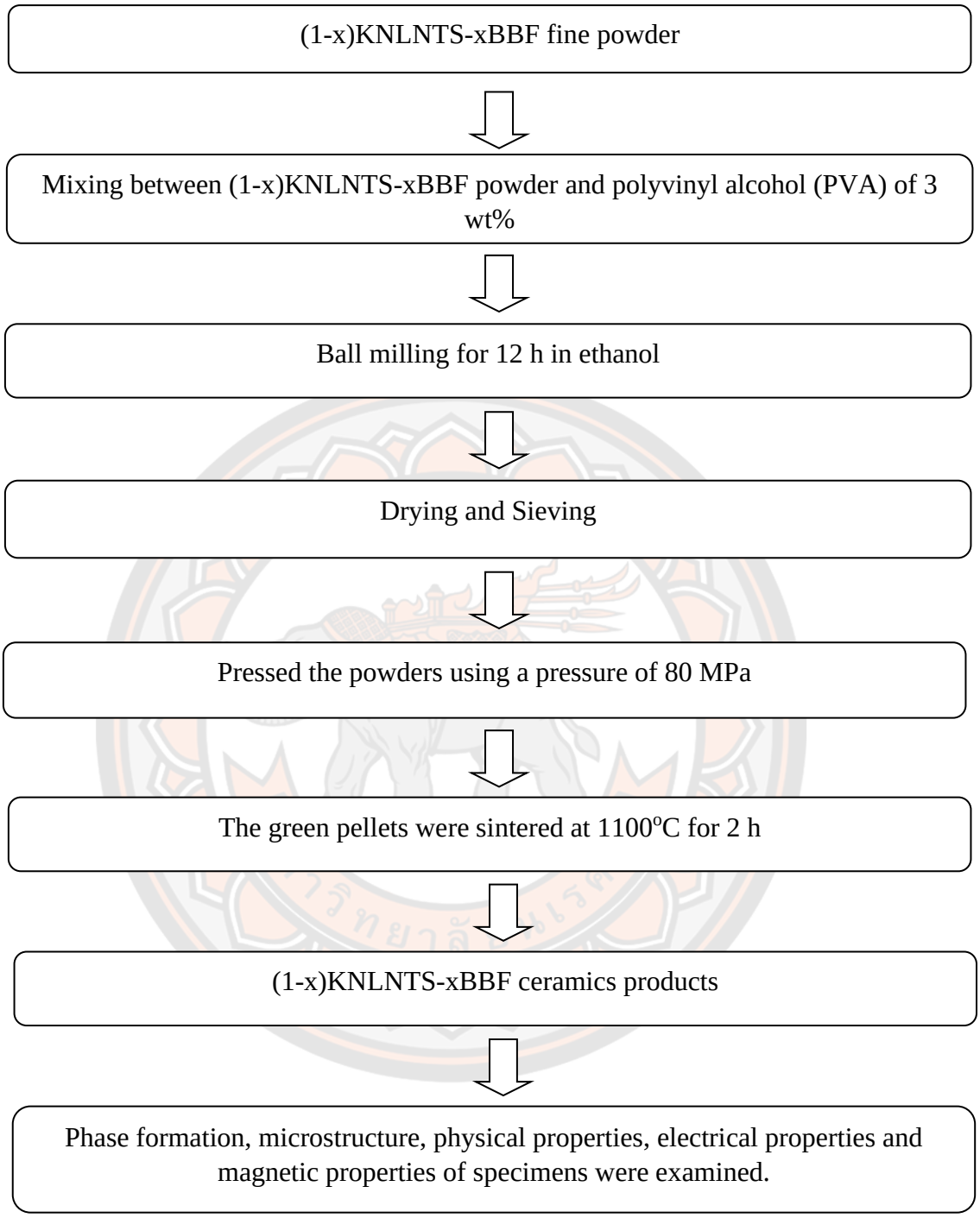

Figure 61 Flowchart of (1-x)KNLNTS-xBBF ceramics preparation using combustion method

The binary system of (1-x)BCTZ-xBBF ceramics

(1-x)$Ba_{0.85}Ca_{0.15}Ti_{0.90}Zr_{0.10}O_3$-x$Bi_{0.80}Ba_{0.20}FeO_3$ [(1-x)BCTZ-xBBF] ceramics with x=0-0.4 were prepared via the solid-state combustion technique using glycine as fuel. The stoichiometric qualities of $Ba(NO_3)_2$ (99%, Himedia), $Ca(NO_3)_2$*$4H_2O$ (99-103.0%, Ajex Finechem), TiO_2 (99.0-100.5%, Ajex Finechem), ZrO_2 (99%, Cerac), $Bi(NO_3)_3$*$5H_2O$ (98.50%, Ajex Finechem) and $Fe(NO_3)_3$*$9H_2O$ (98.0-101.0%, Ajex Finechem) were used as raw materials, weighed and then ball milled in ethanol for 24 h. After that, the slurry was dried and mixed with glycine ($C_2H_5NO_2$, >98.5%, Fluka Swit) at the ratio of 1:2, in an agate mortar and then calcined at 1050^{o}C for 2 h in air (16). The calcination heating rate was 2^{o}C/min from room temperature to 300^{o}C, 5^{o}C/min from 300 to 1050^{o}C and allowed to cool down naturally (16). The calcined powders were ball milled with 3 wt.% PVA for 12 h. After that, the mixed solutions were dried, sieved and pressed into pellets at a pressure of 80 MPa, with a diameter of 15 mm and a thickness of 1.2 mm. The pellets were sintered at 1450^{o}C for 2 h in air with a heating rate of 2^{o}C/min from room temperature to 600^{o}C, then 5^{o}C/min from 600^{o}C to 1450^{o}C and allowed to cool down naturally (16).

The phase formation of the samples was observed using X-ray diffraction (XRD, Bruker, D8 Discover) and analyzed by the Rietveld refinement method. To prepare the SEM samples, the sintered pellets were polished with sandpaper and alumina abrasive, and then thermally etched at 100^{o}C lower than the sintering temperature for 20 min with a heating rate of 5^{o}C/min and allowed cool down. The surface morphology was observed by a scanning electron microscope (SEM, Leo1455VP). The average grain size was obtained from the linear interception method on SEM images. Archimedes' method was used to measurement the density of the sintered samples. To measure the electrical properties, the pellets were polished to a thickness less than 0.8 mm and silver paste was painted onto both pellet surfaces. Then, the pellets were fired at 500^{o}C for 30 minutes. The dielectric constant and dielectric loss were measured with a LCR meter (HP4284A) in the temperature range of room temperature to 200^{o}C. The ferroelectric hysteresis (P-E) loops were measured by a computer-controlled modified Sawyer-Tower circuit (Radiant, PLC2-1014346) at room temperature. The ferromagnetic property were characterized using a vibrating sample magnetometer (Versa Lab, Quantum Design).

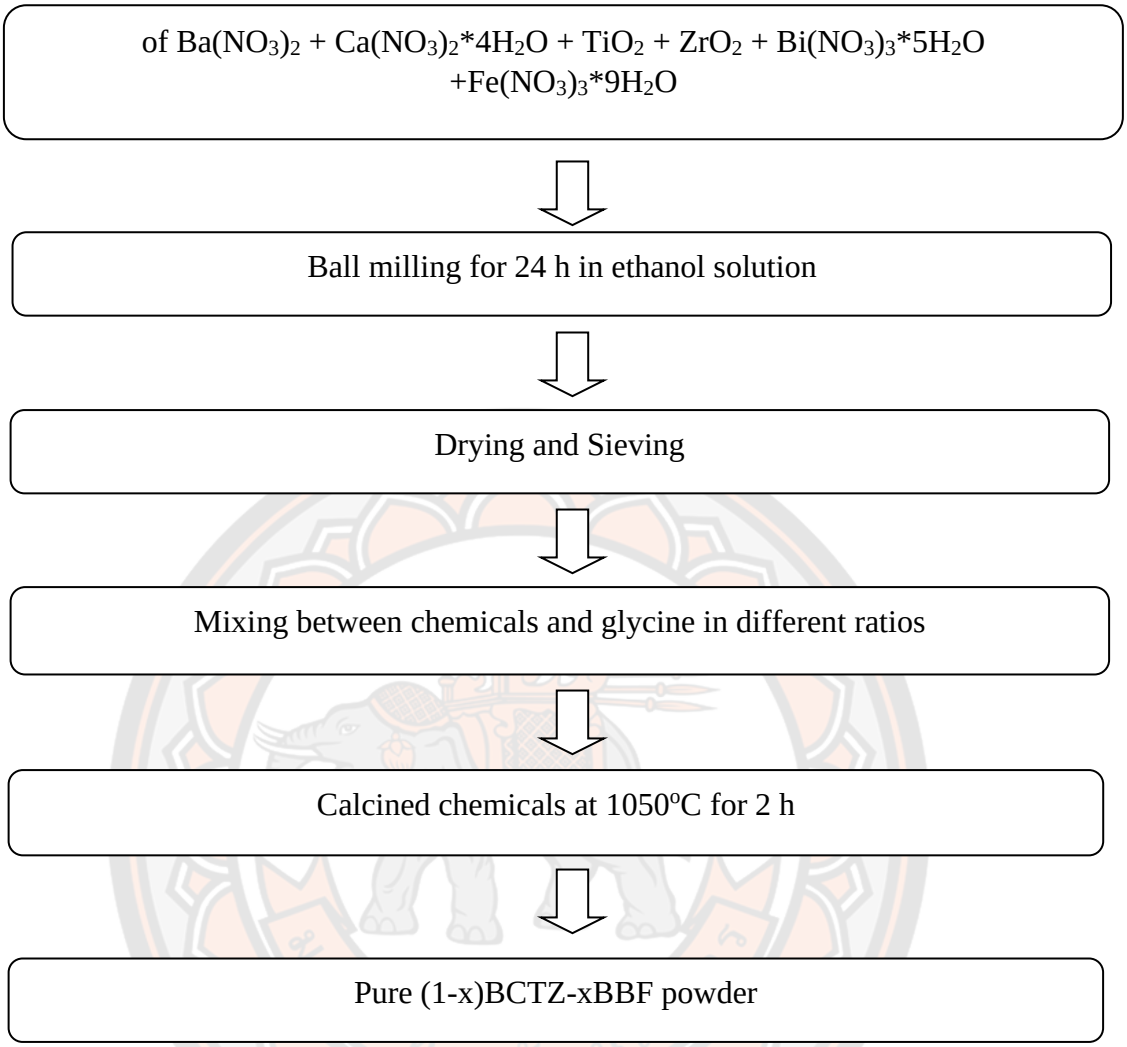

Figure 62 Flowchart of (1-x)BCTZ-xBBF powder preparation using combustion method

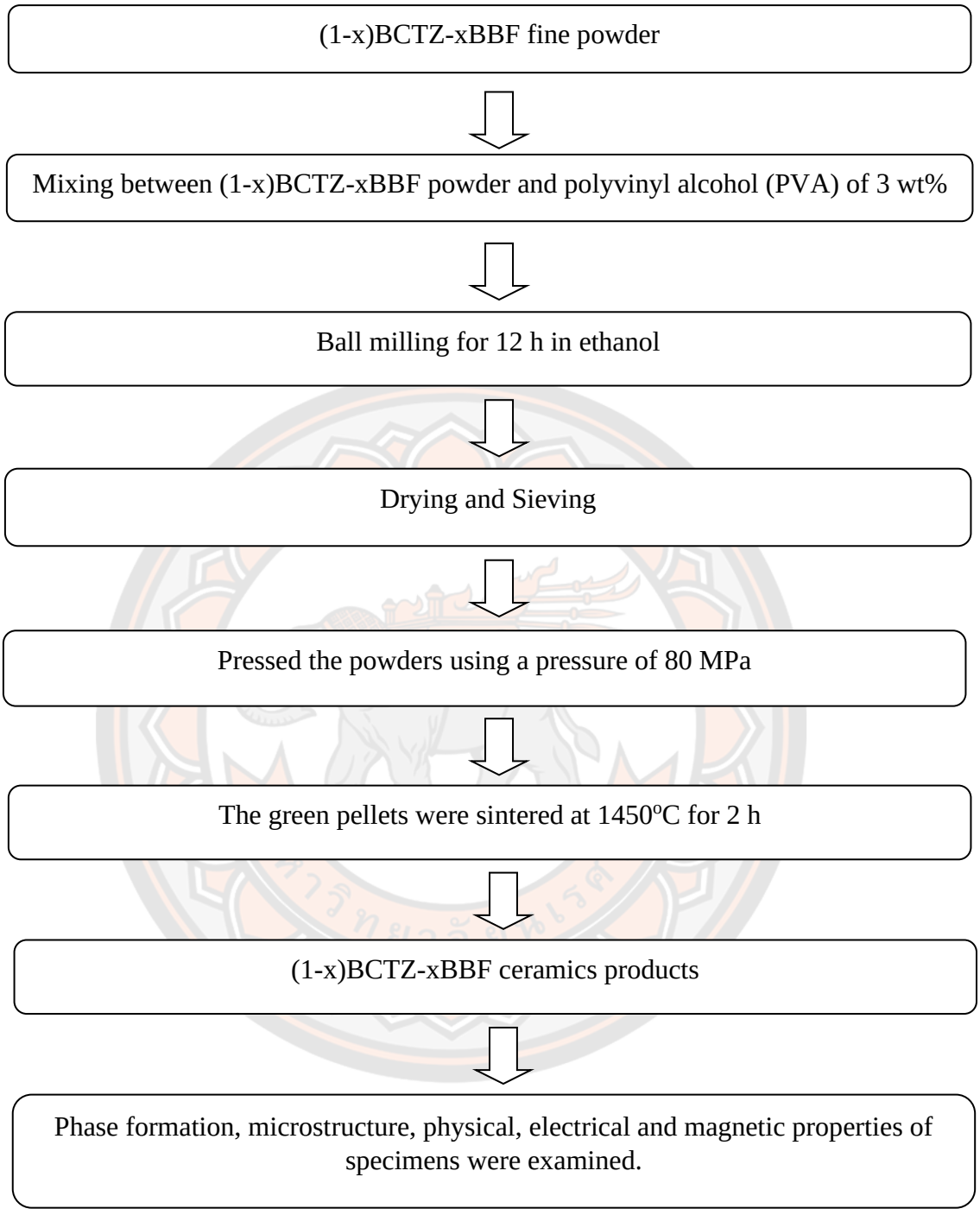

Figure 63 Flowchart of (1-x)BCTZ-xBBF ceramics preparation using combustion method

Characterization technique

X-ray diffraction (XRD)

X-ray diffraction is the one of the most important to analyze all type of matter ranging including the fluids, powders and crystals. In the research, XRD is the essential technique for the characterization of material and quality control. Generally, the XRD technique were widely used for the identification of the crystalline phases of powders and ceramics which can be explained the three-dimensional atomic structure of crystalline solids. For the simplest instance, the scattering of the x-ray is occurred by the atom in the plane of periodic in phase and diffraction which defined by the angle θ as presented in equation 18. Moreover, the experimental of x-ray diffraction also related to the diffraction intensities.

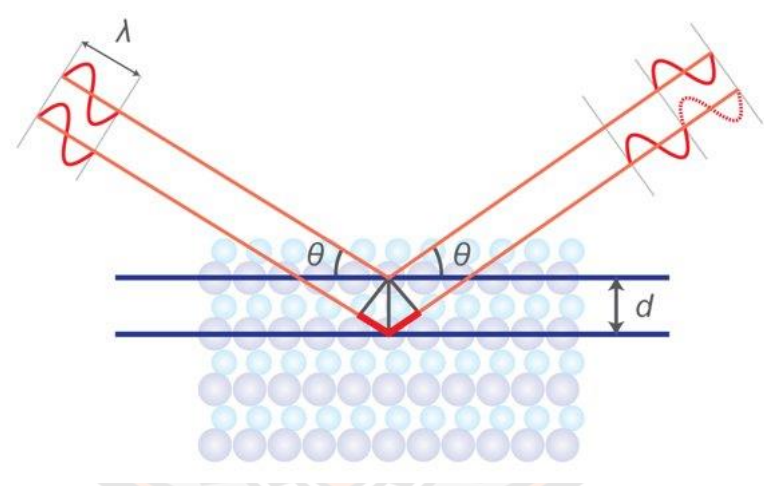

Figure 64 X-ray diffraction

The Bragg equation are

$$n\lambda = 2d \sin \theta \qquad (18)$$

where n is the integer

λ is the wavelength of the incident X-ray beam

d is distance between atomic layers in a crystal

θ is the reflect X-ray beams at certain angles of incidence

For this purpose, the samples were fabricated following the same experimental process explained in section 3.1. Subsequent, this sample were analyzed by the X-ray

diffraction (XRD) analysis (XRD, X'pert MPD 3040, Phlips, Netherland) with Cu K_α (λ=1.5406 Å) in the angular range from 10° to 70° with a step size of 0.012°.

For advance XRD analysis, the Reitveld refinement is wildly used to analyze the structural analysis and accepted to be an exceptionally valuable method. For the method of Rietveld refinement, user can select various parameter such lattice parameters, peak width and shape and preferred orientation to minimize the difference between experimental patterns and a crystallographic model which depend on the crystal structure and instrumental parameters. As the parameters mentioned above, the accurate quantitative information and site occupancy factors were obtained from the refinement. In this study, the Fullprof program was used with the crystallographic model from the literature. After the refinement, the quality of the agreement between experiment and calculated profiles were considered which the agreement factors included the profile factor (R_p), weighted profile factor (R_{wp}), expected weighted profile factor (R_{exp}) and chi-square (χ^2) as showed in equation 19-22, respectively.

Profile factor:

$$R_p = 100\frac{\sum_{i=1,n}\left|y_i - y_{c,i}\right|}{\sum_{i=1,n} y_i} \tag{19}$$

Weighted profile factor:

$$R_{wp} = 100\left[\frac{\sum_{i=1,n} w_i\left|y_i - y_{c,i}\right|^2}{\sum_{i=1,n} w_i y_i^2}\right]^{1/2} \tag{20}$$

Expected weighted profile factor:

$$R_{\exp} = 100\left[\frac{n-p}{\sum_i w_i y_i^2}\right]^{1/2} \tag{21}$$

Goodness of fit indicator:

$$S = \frac{R_{wp}}{R_{\exp}}$$

Reduced chi-square:

$$\chi^2 = \left[\frac{R_{wp}}{R_{\exp}}\right]^2 = S^2 \qquad (22)$$

When y_i is the observed intensity.

w_i is the statistical weight based on counting statistic.

$y_{c,i}$ is the calculated intensity at a diffraction angle of 2θ

After refinement, the values of χ^2 are less than 4. While, the R_p, R_{wp} and R_{exp} should be less than 15% which confirm the goodness of refinement.

Scanning electron microscopy (SEM)

Scanning electron microscopy (SEM) is a technique for highly energetic electron beam. Electron gun are produced electron by the thermionic emission which electron was accelerated in vacuum by the application of electric field. When the specimen was interacted by the electron beam, it can occur the several phenomena such as the secondary electron emission, back scattering and emission of characteristic X-rays. The secondary electrons (SEs) are originated from atoms near the surface of a sample which are ejected by the primary electrons. SEs can be classified by the type of bonding into (i) slow SEs (loosely bound), (ii) fast SEs (strongly bound) and (iii) auger electrons (outer electrons emitted in place of characteristic x-ray). Generally, the SEM image was received from the slow SEs which this image is referred to as secondary electron image. In case of fast electron, they are not used to analyze the specimen due to the emission of another characteristic destructive to resolution and chemical analysis. Finally, the auger electrons was only used for Auger spectroscopy which no relevant in this study.

It is well known that the primary electrons is scattered by the nucleus at angle approach 180^o which is backscattered electrons. Backscatter electron was used to study chemical vibration in sample surface which this intensity of backscatter is proportional to the atomic number of the atom. Although the wavelength of X-ray characteristic is rather specific, however, the element with low concentration or atomic number are difficult to detect. For the chemical or element analysis of sintered

samples, the samples were polished by the sandpaper with different grit (150, 400, 600, 1000, 1200, 2400 and 4000). The polished samples were thermally etched at lower 100^{o}C of sintered temperature for 20 min. The samples were coated with gold using a sputter coater. SEM images were performed by the scanning electron spectroscopy (SEM, Leol455VP). The average grain size was calculated using the linear interception method on SEM images of samples.

Figure 65 scanning electron microscopy

Density measurement

Density of all sintered samples can be determined by Archimedes method which this method is a measurement of the dry, saturated and suspended weight. The calculation of Archimedes principle is showed in equation 23.

$$\rho_{bulk} = \left(\frac{W_d}{W_{sat} - W_{susp}} \right) \cdot \rho_{water} \qquad (23)$$

Where ρ_{bulk} is the density of sample, W_d is dry weight of sample in air, W_{sat} is the saturate weight of sample in air, W_{susp} is the suspended weight in water and ρ_{water} is

the density of water at measurement temperature. The precise results for dense samples are given by the Archimedes method.

Shrinkage measurement

The changing diameter of the samples were calculated the percentage of shrinkage as presented in equation 24.

$$\text{Shrinkge}(\%) = \left(\frac{I_b - I_a}{I_a} \right) \times 100 \qquad (24)$$

Where I_a is diameter of pellet after sintering (mm) and I_b is diameter of pellet before sintering (mm).

Electrical measurement

Dielectric constant and dielectric loss tangent measurements

The LCR (L=Inductance, C=Capacitance and R=resistance) meter (Agilent 4263B) was used to measure the dielectric constant and dielectric loss tangent of the sintered samples. The equation 25 can be calculated the dielectric constant.

$$\varepsilon_r = \frac{Ct}{\varepsilon_0 A} \qquad (25)$$

where ε_r is the relative permittivity or dielectric constant, ε_0 is the permittivity of free space (8.854×10^{-12} F/m), C is the capacitance (F), t is the sample thickness (mm), A is the sample area (m^2). When computer connected to the LCR meter, the dielectric constant and dielectric loss tangent value were measured during the experiment. The both of dielectric behavior were measured as a function of temperature in the range of 30 to 450^{o}C at different frequencies (1, 10 and 100 kHz).

Figure 66 LCR meter (Agilent 4263B)

Impedance spectroscopy

The impedance spectroscopy (IS) was used to interpret the electrical microstructure which was measured by the Keysight impedance gain/phase analyzer (model 4194A) as showed in Figure 65 For the measurement, the complex impedance (Z) in a temperature range of 480-540°C and the frequency range of 20 Hz to 1 MHz was performed. The obtained impedance data was analyzed by utilizing a combination of the impedance complex plane plot (Z* plot) and the spectroscopic plot of the imaginary part of the impedance (Z″ spectroscopic plot).

Figure 67 the Keysight impedance gain/phase analyzer (model 4194A) at Mae Fah Luang University

Ferroelectric

Ferroelectric properties (P-E hysteresis loops) and mechanical properties (S-E strain loops) can be carried out using a computer controlled modified Sawyer Tower circuit principle with high voltage amplifier (Trek), precision High Voltage Interface (HVI, Radiant Technologies), precision LC (Radiant Technologies) and computerized control and data acquisition. The sintered sample were polished to ~0.7 mm and then silver electrode on both sides. In the measurement process, the electric field of 10-50 kV/cm was applied to a sample with immersed in the silicone oil. The obtained results are given from the automatic device system which induced for measuring the polarization of material with a single triangle wave.

Figure 68 the computer controlled modified Sawyer Tower circuit

Magnetic properties

The measurement of magnetic properties of all samples were used Vibrating Sample Magnetometer (Versa Lab, Quantum Design) at Khon Kaen University (Figure 69). The magnetic property was measured at the temperature of 50 K and 300 K. The relationship between the magnetization (abbreviation; M show in Y axis of graph) and magnetic field (abbreviation; m show in x axis of graph) were presented in graph which the magnetic characteristic (diamagnetic, paramagnetic and ferromagnetic) can be observed from M-H hysteresis loops.

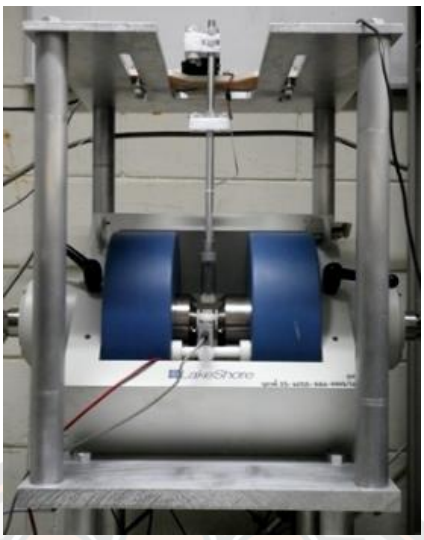

Figure 69 Vibrating Sample Magnetometer (VSM) at Khon Kaen University

CHAPTER IV

RESULTS AND DISCUSSION

Effect of BFCO doping on phase structure, microstructure, electric and magnetic properties of BNKLT ceramics prepared by the combustion method

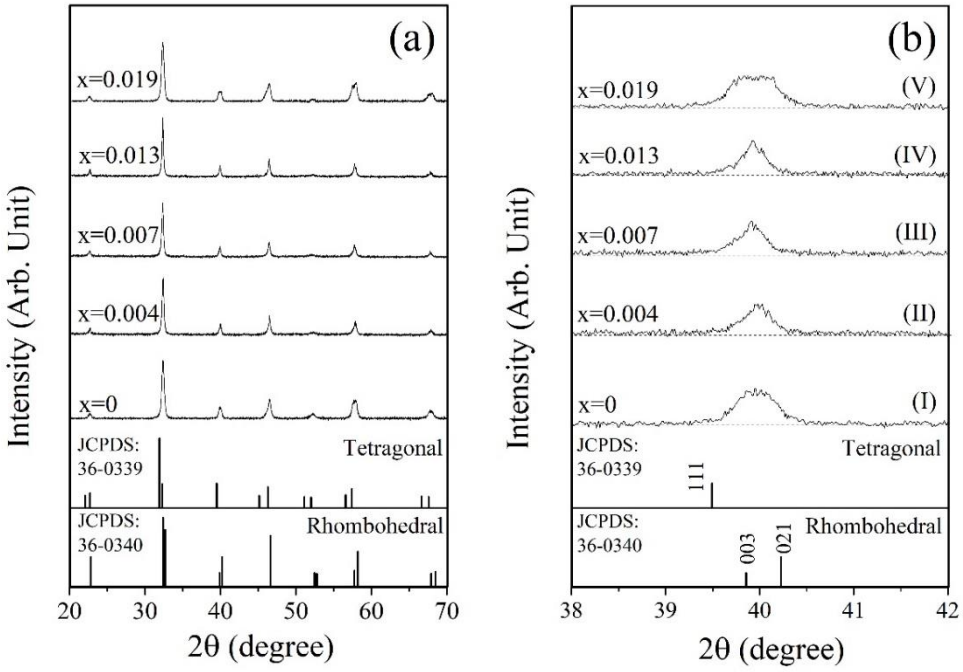

Figure 70 X-ray diffraction patterns of BNKLT-xBFCO ceramics in the 2θ range of (a) 10-70^o and (b) 38-42^o

Figure 70 (a-b) illustrates the X-ray diffraction (XRD) results of all the sintered samples. All samples showed a single perovskite structure without a secondary phase which matched the JCPDS file No. 36-0339 for $Bi_{0.5}K_{0.5}TiO_3$ and JCPDS file No. 30-0340 for $Bi_{0.5}Na_{0.5}TiO_3$. This confirmed that BFCO has completely entered into the BNKLT lattice. A well known characteristic of the rhombohedral (R) structure is that it exhibits dual peaks of (003)/(021) at 2θ around 40^o. In case of the tetragonal (T) structure, a single peak of (111) at 2θ around 40^o is observed. As shown in the enlarged XRD patterns around 40^o (Figure 70(b)), the

XRD data of the BNKLT ceramics exhibited a broad peak of (003)/(021) (Figure 70 (b) I) which indicated the coexistence between the R and T phases. At $0.004 \leq x \leq 0.013$, the broad peak of (003)/(021) sharpened into a single peak of (111) (Figure 1(b) II-IV) which indicated that the crystal structure possessed a high T structure. When x content increased up to 0.019, the broad peak of (111) were split into (003)/(021) (Figure 70 (b) V) again which inferred that the R phase increased.

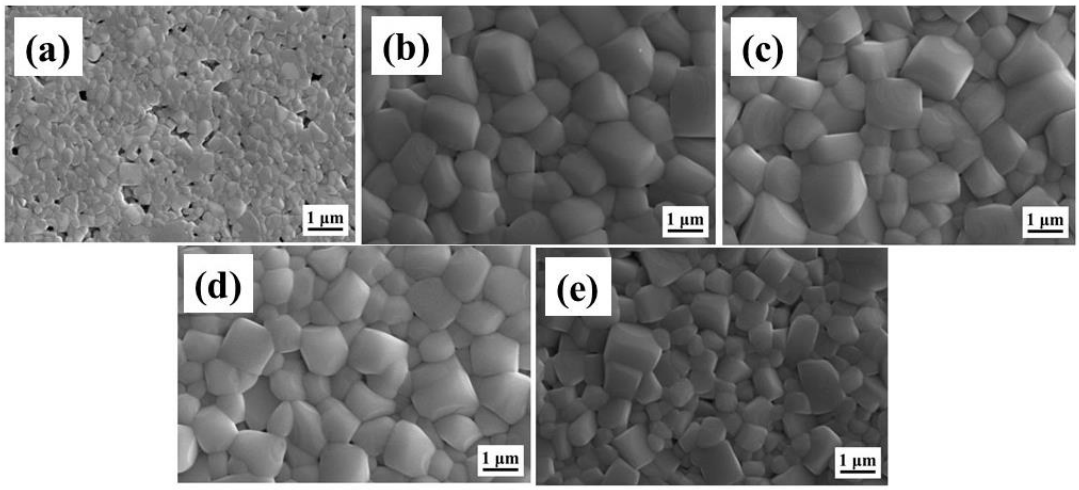

Figure 71 SEM images of BNKLT-xBFCO ceramics (a) x=0, (b) x=0.004, (c) x=0.007 (d) x=0.013 and (e) x=0.019

Figure 71 (a)-(e) shows the surface SEM micrographs of BNKLT-xBFCO polished ceramics. All samples exhibited a polygonal grain shape. The surface morphology of BNKLT ceramics showed large pores and small grain sizes as seen in Figure 71 (a). When x content increased up to 0.013 (Figure 71 (b)-(d)), the grains grew larger, a narrow grain size distribution and less pore were observed which lead to a denser microstructure. The average grain size tended to increase with x content up to x=0.013 and then dropped in value as listed in Table 1. This result suggests that adding x content induced grain growth in BNKLT ceramics, which could be clearly seen in Figure 71 (b)-(e). This result is a good agreement with the results of the BNT-BT-xmol%BFCO and BNT-BCTZ-xmol%BFCO ceramics (101, 102).

For the density results, it was found that the density increased from 4.80 to 5.87 g/cm^3 (80.41-98.42% of theoretical density) when x content increased from 0 to 0.013 (Table 9). With higher x content (x=0.019), the density and relative density decreased. The increased grain growth and densification of BNKLT-xBFCO ceramics can be attribute to two reasons. Firstly, the different valence state of the ions in the B-sites (Cr^{3+} and Fe^{3+} substitution into Ti^{4+} electrons acceptor) induced oxygen vacancies, which helps the ion transport in the ceramics during the sintering process (101). The oxygen vacancy equation can be written as:

$$M_2O_3 \underset{2TiO_2}{\Rightarrow} 2M'_{Ti} + 3O_O^x + V_O^{\bullet\bullet} \qquad (26)$$

Where M is the Cr^{3+} and Fe^{3+} ions. Secondly, Cr and Fe can convert to the liquid phase which is favorable to grain growth. By continuing to increase the x content (0.019mol%), the grain size became smaller and more pores were formed which lead to lower density. These may be caused by the solid solubility limits of the Cr^{3+} and Fe^{3+} ions in the crystal causing a segregation of ions, which plays an important role in inhibiting the grain growth (103, 104). In a similar way, R. Cheng et ai. (104) reported that the addition of excess $(Fe_{1/2}Nb_{1/2})^{4+}$ into the $(Bi_{1/2}Na_{1/2})_{0.935}Ba_{0.065}TiO_3$ ceramics lead to inhibit the grain growth.

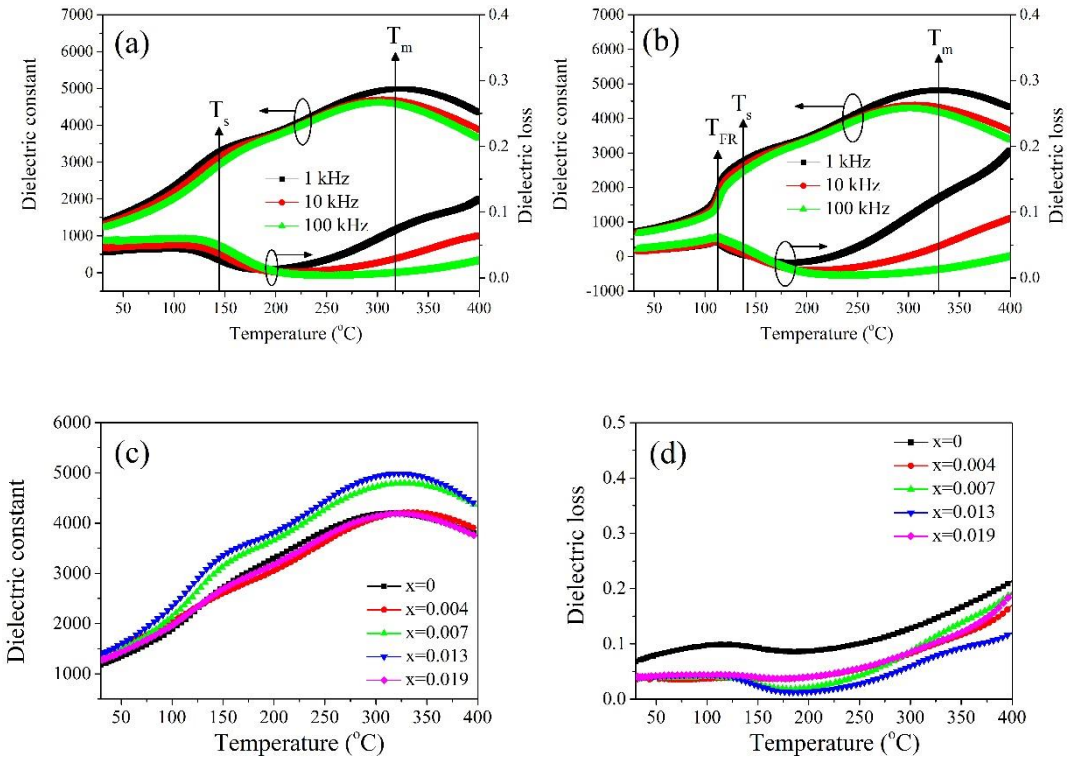

Figure 72 The temperature dependence of the dielectric properties of the BNKLT-0.013BFCO ceramics with different frequencies (a) unpoled and (b) poled. Temperature dependent of (c) dielectric constant and (d) dielectric loss measured at 1 kHz for unpoled BNKLT-xBFCO ceramics

The dielectric constant (ε) and dielectric loss (tan δ) of BNKLT-0.013BFCO unpoled and poled samples at different frequencies (1, 10 and 100 kHz) are shown in Figure 72 (a) and (b), respectively. The dielectric constant and loss showed broad and frequency dependent peaks in both unpoled and poled samples, which indicated that these samples show relaxor ferroelectric behavior. For the unpoled sample (Figure 3 (a)), two dielectrics anomalies were observed. The first anomalous peak was found at a low temperature (T_s) associated with the relaxation of the polar nanoregions (PNRs) of the rhombohedral phase (105-108). While, the second anomalous peak was observed at high temperature (T_m) and was the maximum in the dielectric constant and related to a relaxation of the tetragonal PNRs emerging from the rhombohedral PNRs (106-108). In case of the poled sample (Figure 72 (b)), three dielectric

anomalous peaks were observed. The first dielectric anomaly at the low temperature, around 100°C, is referred to the ferroelectric to relaxor phase transition temperature (T_{FR}), as determine by the sharp peak in the dielectric loss. The second and third anomalous peaks are observed at temperatures around 145°C and 320°C (Figure 72 (b)), which can be attributed similarly to the T_s and T_m anomalous peaks, respectively, in case of the unpoled sample. The T_{FR}, T_s and T_m values of all samples measured at 1 kHz are shown in Table 9.

The temperature dependence of the relative dielectric constant and dielectric loss of the BNKLT-xBFCO ceramics at a frequency of 1 kHz in the temperature range of 30-400°C is presented in Figure 72 (c)–(d). All unpoled samples exhibited two dielectric anomalies (T_s and T_m) as seen in Figure 72 (c). The room temperature dielectric constant (ε_R) and dielectric loss (tan δ_R) of the unpoled samples measured at 1 kHz in frequency are listed in Table 9. The ε_R value tended to increase as the x content increased up to 0.013 and then the ε_R value dropped. The tan δ_R values were found to be between 0.034 and 0.068. The dielectric constant at T_m (ε_m) of BNKLT-xBFCO ceramics tended to increase with x content up to 0.013 and then dropped in value (Table 9). The dielectric loss at T_m (tan δ_m) of BNKLT ceramics doped with BFCO is listed in Table 9. It was observed that the BNKLT-0.013BFCO ceramic exhibited the lowest tan δ_m value (Table 9).

The piezoelectric constant (d_{33}) of BNKLT-xBFCO ceramics tended to improve from 130 pC/N to 194 pC/N when x increased from 0 to 0.013. With x content >0.013, the d_{33} decreased to 100 pC/N. Good electrical properties, such as ε_R=1390, tan δ_R=0.039, ε_m=4986, tan δ_m=0.075 and d_{33}=194 pC/N were obtained from the BNKLT-0.013BFCO ceramic, which corresponded to the ceramic which had exhibited a morphotropic phase boundary (MPB) between R and T phases, a good morphology and the highest density (109).

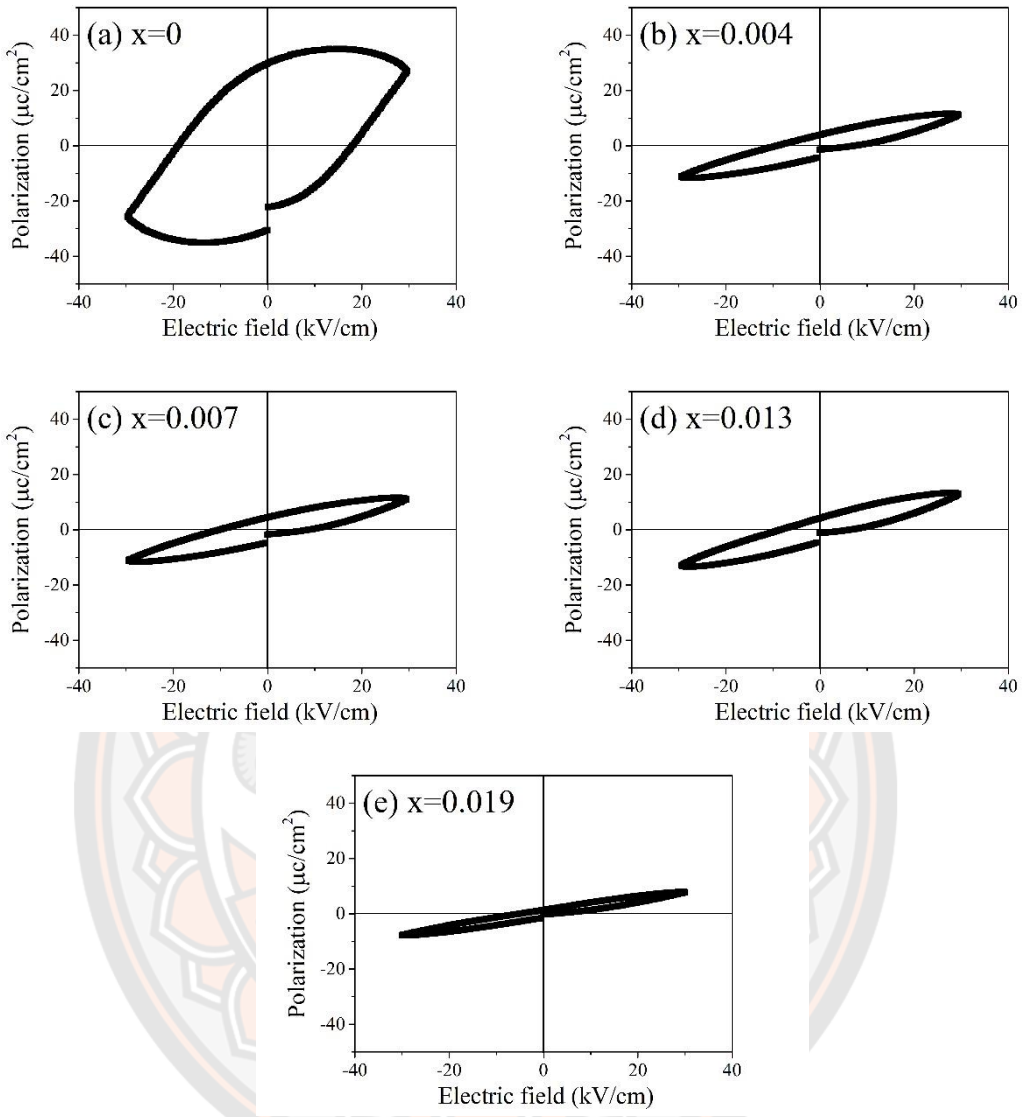

Figure 73 P-E hysteresis loops of BNKLT-xBFCO ceranmics with different x content

Figure 73 (a)-(e) shows the P-E hysteresis loops for the ferroelectric properties at room temperature of BNKLT-xBFCO ceramics measured under an electric field of 30 kV/cm. It was observed that the P-E hysteresis loops of the undoped BFCO sample exhibited saturated and symmetric loops, which corresponds to normal ferroelectric behavior. The remnant polarization (P_r) and coercive field (E_c) of the BNKLT sample were about 29.81 μC/cm^2 and 18.94 kV/cm, respectively. With x content increase,

unsaturated P-E hysteresis loops were observed with rapid decreases of P_r and E_c values as listed in Table 9. Defects and charge carriers of metal ions, Fe^{3+}, Cr^{3+} and Ti^{4+} at the B-sites contribute to the high conductivity in this samples.

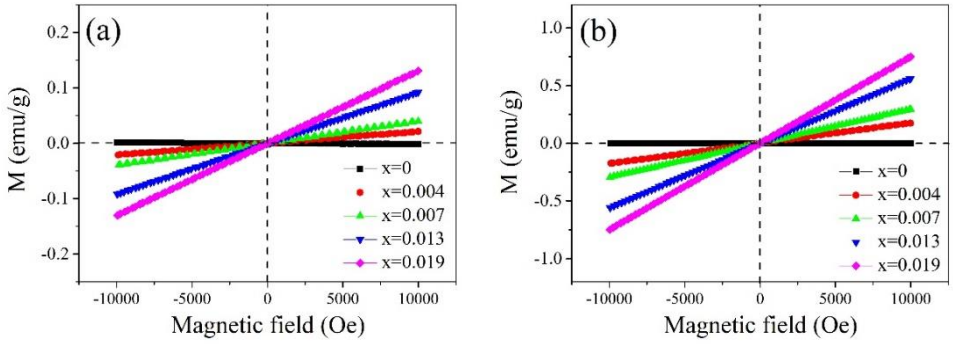

Figure 74 the magnetic M-H curves of BNKLT-xBFCO ceramics measured at (a) 300 K and (b) 50 K

The magnetic field induced magnetization of the BNKLT-xBFCO ceramics with $0 \leq x \leq 0.019$ measured at 300 K and 50 K is shown in Figure 74 (a) and (b). The BNKLT ceramics show a linear magnetization dependence of magnetic field with negative slope, indicating diamagnetic behavior. For samples with $0.004 \leq x \leq 0.019$, they exhibited a linear magnetization dependence of magnetic field with a positive slope implying paramagnetic behavior. This implied that the Cr and Fe magnetic ions inserted into the BNKLT matrix. However, with a low concentration of BFCO, the magnetic exchange interaction of the Cr and/or Fe ions is very small, and thus the ferromagnetism is suppressed (110). The maximum magnetization (M_{max}) at 300 K and 50 K of all samples are listed in Table 9. The M_{max} value increased when the x content increased. Moreover, it was found that the M_{max} value measured at 50 K was much higher than the samples measured at 300 K. This phenomenon can be explained by the atomic vibrations increasing with increasing temperature, which leds to a decrease in the magnetic ordering.

Table 9 Average grain size, density, transition temperature, electrical and magnetic properties of BNKLT-xBFCO ceramics

x	Average grain size (μm)	Measured density (g/cm^3)	Relative density (%)	T_{FR} (°C)	T_s (°C)	ε_R	tan δ_R	T_m (°C)	ε_m	tan δ_m	P_r ($\mu C/cm^2$)	Ec (kV/cm)	M_s at 300 K (emu/g)	M_s at 50 K (emu/g)
0	0.42±0.02	4.80	80.41	110	142	1175	0.068	318	4196	0.141	29.81	18.94	-0.0002	-0.0010
0.004	2.55±0.08	5.76	96.47	60	139	1356	0.034	337	4212	0.108	3.95	9.20	0.021	0.176
0.007	2.47±0.13	5.66	94.89	103	151	1305	0.038	326	4797	0.115	4.47	10.14	0.040	0.295
0.013	2.69±0.12	5.87	98.42	112	147	1390	0.039	322	4986	0.075	4.19	8.96	0.092	0.560
0.019	1.53±0.08	5.72	95.76	97	125	1279	0.040	325	4187	0.102	1.36	5.15	0.131	0.748

Phase formation, microstructure, electric and magnetic properties of multiferroic (1-x) $Bi_{0.5}(Na_{0.77}K_{0.20}Li_{0.03})_{0.5}TiO_3$-x$Bi_{0.8}Ba_{0.2}FeO_3$ ceramics prepared via the solid-state combustion technique

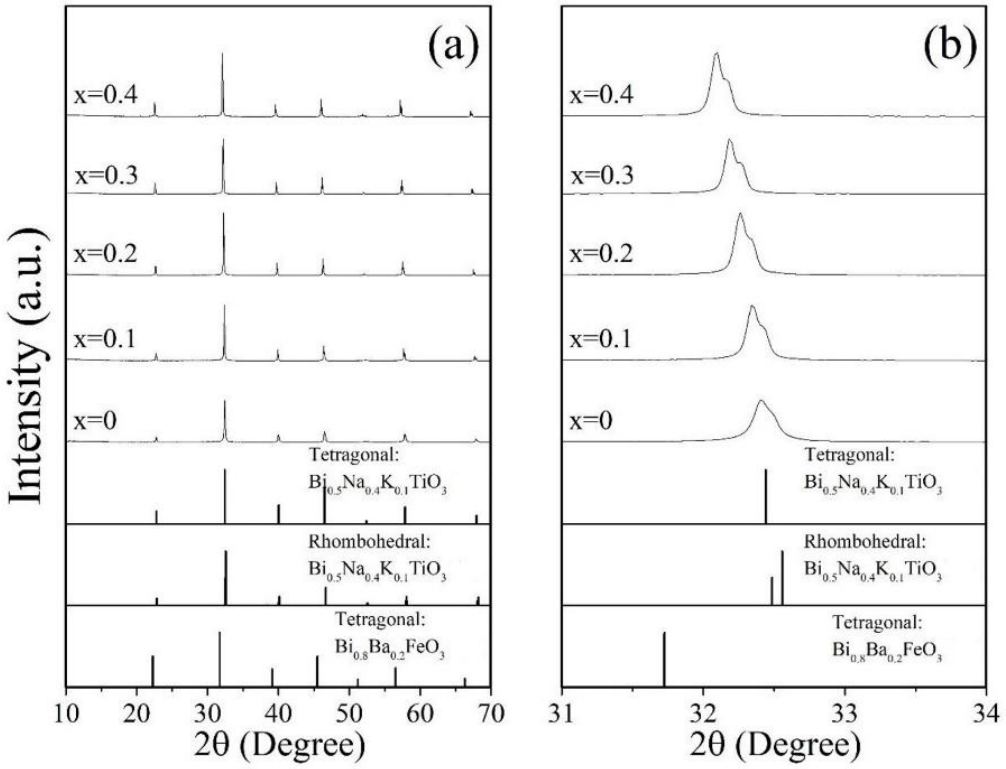

Figure 75 X-ray diffraction patterns of (a) (1-x)BNKLT-xBBF ceramics in the 2θ range from 10 to 70º, (b) and (c) the magnified patterns in the vicinity of 2θ ~40º and ~46º

Figure 75 (a) shows the XRD patterns of (1-x)BNKLT-xBBF ceramics in the 2θ range from 10 to 70º, together with the patterns of the tetragonal and rhombohedral phases of $Bi_{0.5}Na_{0.4}K_{0.1}TiO_3$ (BNKT) (111) and tetragonal phase of $Bi_{0.8}Ba_{0.2}FeO_3$ (BBF) (112). All samples exhibited a pure perovskite phase with no secondary phases detected. Figure 75 (b) presents the magnified patterns in the vicinity of 2θ ~32.5º. It was observed that the dual peak with a position at 2θ ~32.5º in the ceramic with x=0 exhibited a broader shaped peak and shifted slightly towards a lower 2θ angle, which is not similar to any reference pattern. This characteristic of the XRD pattern may be

caused by the substitution of Li^{1+} ions in A-sites of the BNKT ceramic. However, the doping of Li^{1+} ions does not transform the main phase structure of the specimen as the main phase structure is coexisting R and T phases, corresponded to previous work (8). When increasing x to 0.4, the position of the dual peaks at 2θ around 32.5° were sharper and more clearly separated, together with a shift towards a lower 2θ angle (Figure 75 (b)). This result means that all samples have no tetragonal phase $Bi_{0.8}Ba_{0.2}FeO_3$ microstructures and the smaller ions of BNKLT were being substituted by the larger ions of BBF.

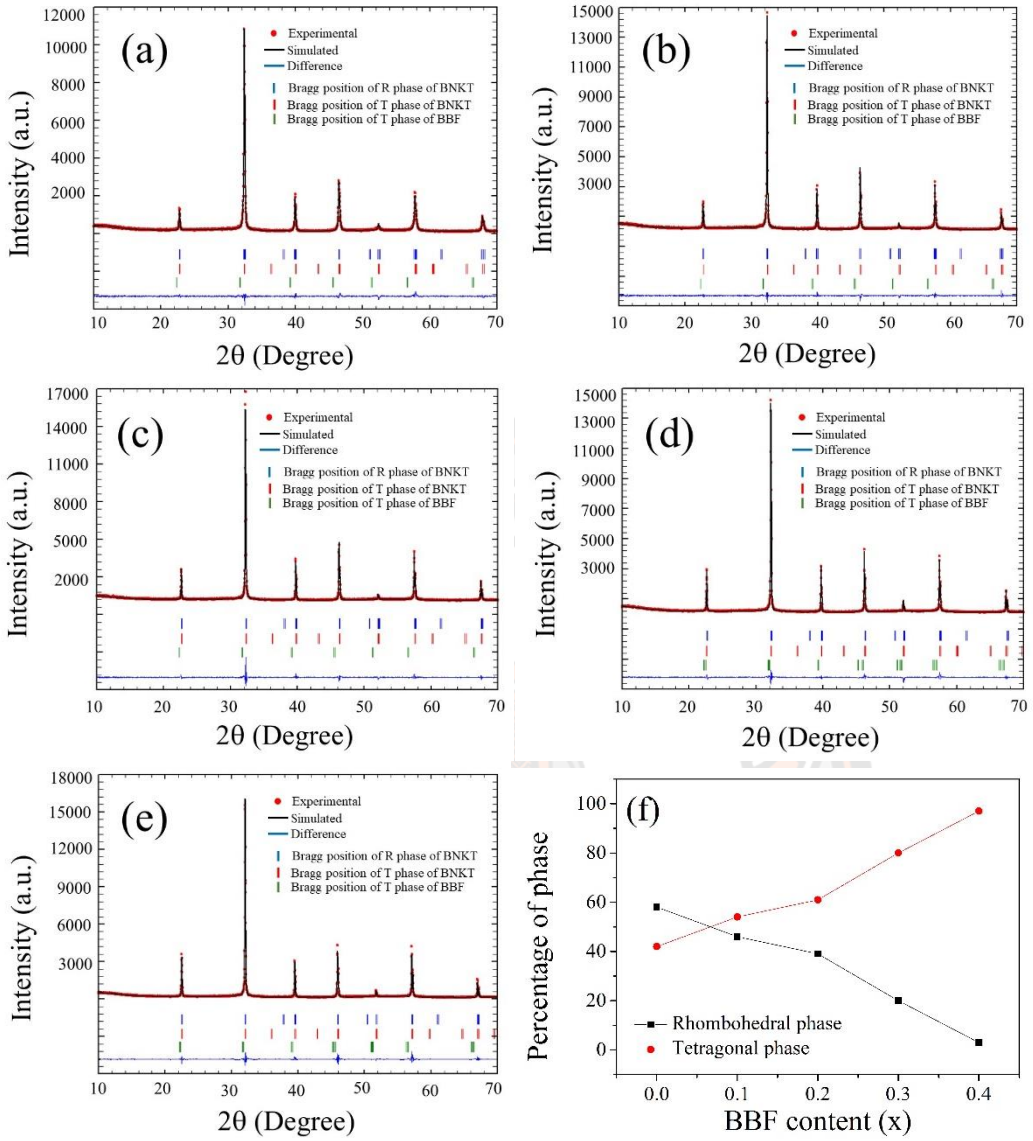

Figure 76 Rietveld refinement of (1-x)BNKLT-xBBF ceramics with various x contents: (a) x=0, (b) x=0.1, (c) x=0.2, (d) x=0.3 and (e) x=0.4 and (f) the percentage of phase with different x content

In order to confirm and complete the XRD analyze, the Rietveld refinement technique was performed using the Fullprof program, as shown in Figure 76. The initial conditions of the cell parameter, the lattice constant, space group and atomic functional position were obtained from corresponding referent patterns calculated from the Crystallography Open Database (COD). The structural model of the rhombohedral space group (*R3c*) of $Bi_{0.5}K_{0.1}Na_{0.4}TiO_3$ (111), tetragonal (*P4bm*) of

$Bi_{0.5}K_{0.1}Na_{0.4}TiO_3$ (111) and tetragonal (*P4mm*) of $Bi_{0.8}Ba_{0.2}FeO_3$ (112) were used to analyze all samples. The background was modeled using a Chebyschev function and the diffraction peak profiles were fitted with a pseudo-Voigt function (113). To further improved the fitting, the scale factor, unit cell, peak shape parameter (e.g. profile half-width parameter (u, v and w), asymmetry parameter), overall B-factor, atomic functional position and occupancy of Bi, Na, K, Li, Ba, Ti, Fe and O sites were refiled. The goodness of the fits for all samples had a chi-squared (χ^2) < 4, indicating the fitting procedure fit the data well (Table 10). The R_p, R_{wp} and R_{exp} values are listed in Table 10. In the case of x = 0, Li^{1+} cations substituted in A-sites of the BNKT lattice. Moreover, at x = 0.1-0.4, the substitution of Bi^{3+}, Ba^{2+} and Fe^{3+} cations into the BNKLT lattice formed a solid solution, which no pure BBF phase could be detected. The confirmation of this was obtained from the Rietveld refinement results (Table 10). As can be seen in Table 10, the unit cell volume (V) tended to increase due to the substitution of the larger ionic radius cations of Ba^{2+} (1.35 Å) and Fe^{3+} (0.64 Å) ions replacing Bi^{3+} (1.03 Å) and Ti^{4+} (0.605 Å) ions, respectively. The ratio of the phase between R and T of BNKLT ceramics was about 58:42 (Table 10). The percentage of the T phase increased from 54 to 97 when x increased from 0.1 to 0.4. An increase in the T phase of (1-x)BNKLT-xBBF ceramics can be explained by the presence of Ba^{2+} ions, which corresponds with L. A. Schmitt et. al and V. Dorcet et. al work's (114, 115). Figure 76 (f) shows the percentage of the R and T phases with a variety of x content. It was found that the R phase continuously decreased with increasing x.

Table 10 Rietveld structural refinement results for the (1-x)BNKLT-xBBF ceramics

x	Goodness of fit	Phase structure	Profile parameters	Atoms information					The percentage of phase
				Label	x	y	z	Occ.	
0	χ^2=1.47 R_p=18.2 R_{wp}=14.7 R_{exp}=12.13	R3c	a= 5.515 Å c= 13.576 Å V= 357.65 Å^3 u= 0.490155 v= 0.699948 w= 0.06746	Na Bi K Li O Ti	0 0 0 0 0.144 0	0 0 0 0 0.337 0	0.275 0.275 0.275 0.275 0.083 0.016	0.374 0.385 0.101 0.005 1.349 0.961	58
		P4bm	a= 5.522 Å c= 3.902 Å V= 118.974 Å^3 u= 0.041986 v= 0.071729 w= 0.00557	Na Bi K Li O1 O2 Ti	0 0 0 0 0 0.263 0	0.5 0.5 0.5 0.5 0 0.237 0	0.553 0.553 0.553 0.553 0.512 0.03 0	0.219 0.385 0.097 0.028 1.676 1.564 1.076	42
0.1	χ^2=1.49 R_p=19.5 R_{wp}=14.9 R_{exp}=12.17	R3c	a= 5.533 Å c= 13.599 Å V= 360.505 Å^3 u= 0.484981 v= 0.842831 w= 0.19874	Na Bi K Li O Ti Fe	0 0 0 0 0.144 0 0	0 0 0 0 0.337 0 0	0.275 0.275 0.275 0.275 0.083 0.016 0.016	0.304 0.381 0.106 0.044 1.148 0.889 0.062	46
		P4bm	a= 5.532 Å c= 3.911 Å V= 119.712 Å^3 u= 0.048411 v= 0.036917 w= 0.01289	Na Bi K Li O1 O2 Ti Fe	0 0 0 0 0 0.263 0 0	0.5 0.5 0.5 0.5 0 0.237 0 0	0.553 0.553 0.553 0.553 0.512 0.03 0 0	0.367 0.386 0.088 0.091 1.913 1.882 0.919 0.124	54
0.2	χ^2=1.56 R_p=19.8 R_{wp}=14.5 R_{exp}=11.57	R3c	a= 5.547 Å c= 13.571 Å V= 361.626 Å^3 u= 0.025792 v= -0.01083 w= 0.00856	Na Bi K Li O Ti Fe	0 0 0 0 0.144 0 0	0 0 0 0 0.337 0 0	0.275 0.275 0.275 0.275 0.083 0.016 0.016	0.344 0.372 0.061 0.037 1.358 0.934 0.101	39
		P4bm	a= 5.546 Å c= 3.923 Å V= 120.653 Å^3 u= 0.011459 v= -0.01414 w= 0.00888	Na Bi K Li O1 O2 Ti Fe	0 0 0 0 0 0.263 0 0	0.5 0.5 0.5 0.5 0 0.237 0 0	0.553 0.553 0.553 0.553 0.512 0.03 0 0	0.372 0.324 0.078 0.057 1.580 1.766 0.913 0.103	61

0.3	χ^2=1.80 R_p=20.1 R_{wp}=16.6 R_{exp}=12.36	R3c	a= 5.545 Å c= 13.598 Å V= 362.034 Å^3 u= 0.108885 v= -0.05636 w= 0.01112	Na Bi K Li O Ti Fe	0 0 0 0 0.144 0 0	0 0 0 0 0.337 0 0	0.275 0.275 0.275 0.275 0.083 0.016 0.016	0.385 0.381 0.130 0.022 1.601 1.078 0.163	20
		P4bm	a= 5.557 Å c= 3.926 Å V= 121.217 Å^3 u= 0.036016 v= -0.03636 w= 0.01346	Na Bi K Li O1 O2 Ti Fe	0 0 0 0 0 0.263 0 0	0.5 0.5 0.5 0.5 0 0.237 0 0	0.553 0.553 0.553 0.553 0.512 0.03 0 0	0.393 0.377 0.130 0.021 1.248 1.428 1.315 0.157	70
0.4	χ^2=1.55 R_p=20.3 R_{wp}=14.9 R_{exp}=11.94	R3c	a= 5.580 Å c= 13.681 Å V= 368.896 Å^3 u= 0.098837 v= 0.28705 w= 0.90023	Na Bi K Li O Ti Fe	0 0 0 0 0.144 0 0	0 0 0 0 0.337 0 0	0.275 0.275 0.275 0.275 0.083 0.016 0.016	0.367 0.352 0.063 0.085 1.779 0.899 0.208	3
		P4bm	a= 5.579 Å c= 3.948 Å V= 122.894 Å^3 u= 0.053182 v= 0.059145 w= 0.00894	Na Bi K Li O1 O2 Ti Fe	0 0 0 0 0 0.263 0 0	0.5 0.5 0.5 0.5 0 0.237 0 0	0.553 0.553 0.553 0.553 0.512 0.03 0 0	0.390 0.407 0.005 0.022 1.398 1.276 0.954 0.211	97

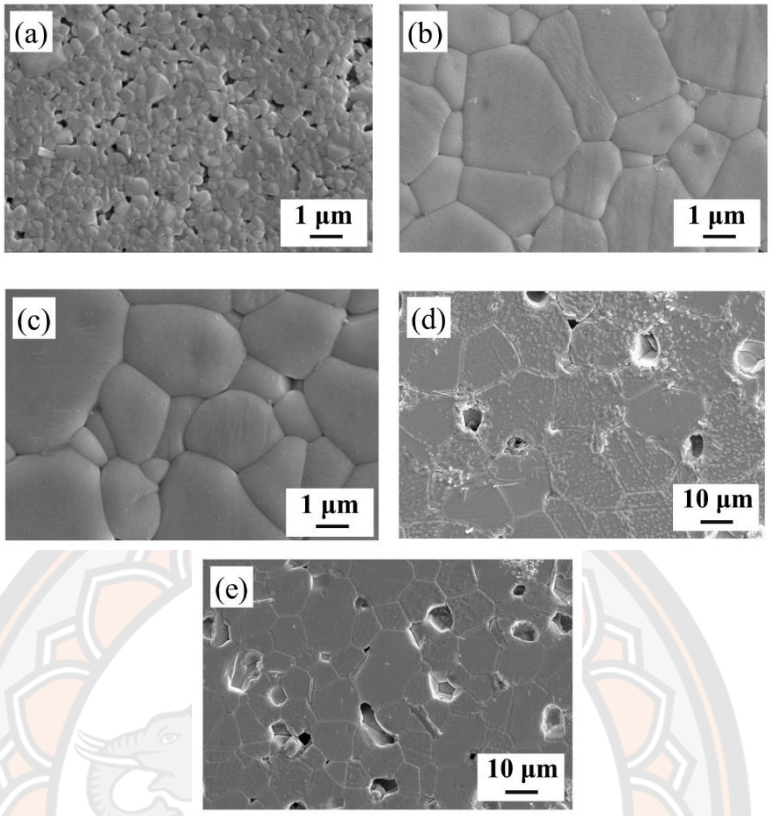

Figure 77 SEM micrograph of (1-x)BNKLT-xBBF ceramics; (a) x=0, (b) x=0.1, (c) x=0.2, (d) x=0.3 and (e) x=0.4

Figure 77 (a)-(e) shows the polished and thermally etched surfaces of (1-x)BNKLT-BBF ceramics with different x content by scanning electron microscopy (SEM). As can be seen, the grains of the (1-x)BNKLT-xBBF ceramics display a polyhedron shape. For BNKLT ceramics (Figure 77 (a)), a small grain size was observed with large pores on the surface and the grains were loosely joined. When x increased up to 0.2 (Figure 77 (b)-(e)), the ceramic grains rapidly grew and were closely packed. Moreover, a well-developed morphology and clear grain boundaries were observed. At $x \geq 0.3$ (Figure 77 (d)-(e)), the porosity increased at the grain boundaries, while the grain boundaries became unclear. The average grain size increased from 0.42±0.02 to 14.96±1.35 µm when the x increased from 0 to 0.4 as listed in Table 11. From the density results, it was observed that the density increased from 4.81 to 6.45 g/cm^3 as the x content increasing from 0 to 0.4 (Table 11). The density as a percentage of the maximum theoretical density increased with x content

up to 0.2 and then dropped as listed in Table 11. The highest theoretical density was about 95.48% which was obtained from the 0.8BNKLT-0.2BBF ceramic. It is well known that an increase in the grain size of a ceramic can be attributed to two main factors. First, the addition of BBF can induce the liquid phase during the sintering process which makes the ceramics more sinterable (103). Second, oxygen vacancies form, which enhances mass transport in the ceramics during the sintering process (104, 116). In our study, the oxygen vacancies originated from the different valent state of the ions in the B-sites (Fe^{3+} substitution into Ti^{4+} sites) which can be written as:

$$Fe_2O_3 \underset{2TiO_2}{\Rightarrow} 2Fe'_{Ti} + 3O_O^x + V_O^{\cdot\cdot} \qquad (27)$$

Therefore, increasing the amount of oxygen vacancies as x increased from 0-0.2 leaded to an increase in average grain size and higher densification. However, as x increases further (x=0.3-0.4), the porosity was observed to increase due to excessive oxygen vacancies, which led to a decrease in the density of the samples. In addition, an excessive amount of the liquid phase during sintering can also resulted in a porous microstructure. This behavior is in agreement with other reported research in BNT systems (104, 116).

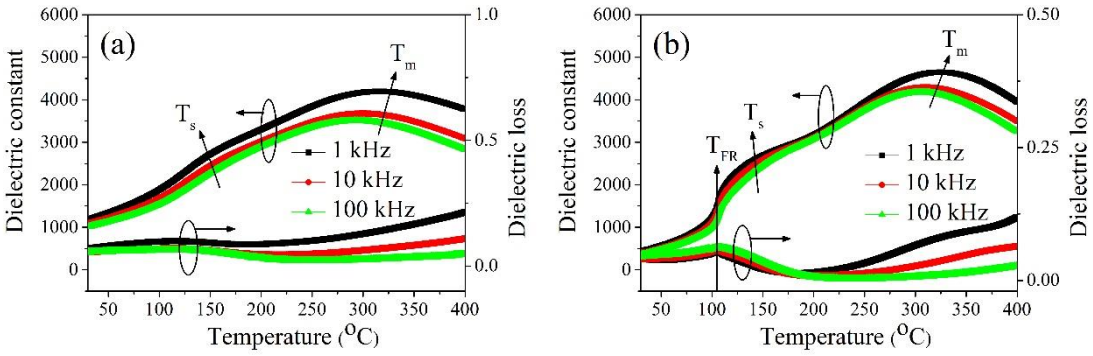

Figure 78 The temperature dependence of the dielectric properties of BNKLT ceramics with x=0 at different frequencies (a) unpoled and (b) poled

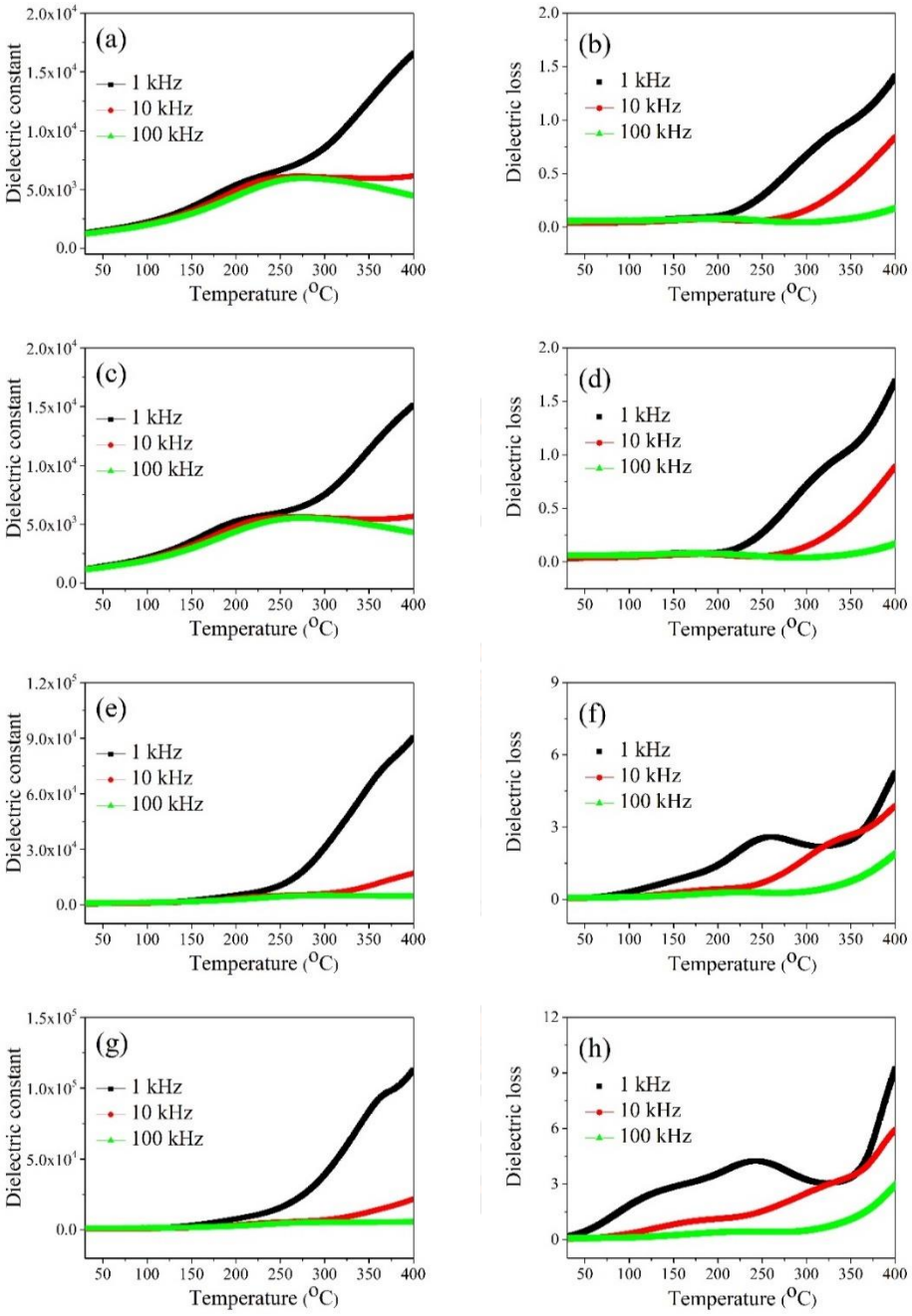

Figure 79 Temperature dependence of the dielectric constant and loss of (1-x)BNKLT-xBBF ceramics; (a)-(b) x=0.1, (c)-(d) x=0.2, (e)-(f) x=0.3 and (g)-(h) x=0.4

Figure 78 (a) and (b) show the temperature dependence of the dielectric properties of the BNKLT ceramic for an unpoled and a poled sample at difference frequencies (1, 10 and 100 kHz). The dielectric constant (ε) and loss (tan δ) showed a broad and frequency dependent peak in both unpoled and poled samples, which indicated that these samples are relaxor ferroelectric. This behavior relates to the multiple ion substitutions in the A and B-sites of the perovskite structure (117). For the unpoled samples (Figure 78 (a)), two dielectric anormaly peaks in the dielectric constant were observed. The first peak which occured at a lower temperature (T_s) ~150^{o}C is associated with relaxation of the polar nanoregions (PNRs) with different symmetries and the electric field inducing long-range ferroelectric order in BNT-based ceramics (107, 108, 118). While, the second peak located at a higher temperature (T_m) ~325^{o}C relates to a relaxation of the tetragonal PNRs emerging from rhombohedral PNRs and denotes a maximum in the dielectric constant. For the poled samples (Figure 78 (b)), three dielectric anomaly peaks were observed. The first peak observed at low temperature (~110^{o}C) is the phase transition temperature from ferroelectric to relaxor (T_{FR}). The T_{FR} peak is determined from the frequency independent peak in the dielectric loss of the poled samples (119, 120). The second and third peaks of the poled sample are related to the T_s and T_m of the unpoled sample.

In case of unpoled (1-x)BNKLT-xBBF ceramics with x=0.1-0.4, the temperature dependence of the dielectric constant and loss at different frequecies (1, 10 and 100 kHz) is shown in Figure 79 (a)-(h). At low temperatures, the dielectric constant was almost stable for all frequencies. At increasing temperatures, both the dielectric constant and dielectric loss increased sharply which may be associated with space charge polarization and higher ionic conductivity at higher temperatures leading to higher leakage current in the $BiFeO_3$ ceramics (17, 121, 122). Similar behaviors were observed in $0.7BiFeO_3$-$0.3Bi_{0.5}Na_{0.5}TiO_3$ (121), (1-x)$BiFeO_3$-x$Bi_{0.5}K_{0.5}TiO_3$ (122) and x$BiFeO_3$-(1-x)$BaTiO_3$ (17) ceramics. In addition, the dielectric loss tangent exhibited an abnormal peak which is attributed by two reasons. First, the transient interaction between the Fe^{3+} and Fe^{2+} ions was obsereved in these samples which is similar to S. Cheng work's (123). Second, the oxygen vacancies that occurred from the substiution of Fe^{3+} into Ti^{4+} sites. The dielectric constant and dielectric loss at

room temperature (ε_R and tan δ_R) of the BNKLT ceramic was about 1175 and 0.068, respectively. The ε_R value increased as x increased up to 0.2 and then dropped in value (Table 11). While, tan δ_R decreased as x increased up to 0.1 and then increased with increasing x content (Table 11). The highest ε_R value of the sample at x=0.2 can be attributed to the well-developed grain structure as seen in Figure 77 (c). Moreover, the increase in grain size can increase the domain size which leds to the formation of multiple domains and domain wall movement. This behavior can increase the dielectric constant at room temperature (124). However, the dielectric constant decreased at higher x content (x=0.3-0.4). Excessive oxygen vacancies and an increased liquid phase during the sintering process for the x=0.3-0.4 samples led to an increase in the porosity, resulting in inhibited domain wall movement (125). The maximum dielectric constant and dielectric loss at T_m (ε_m and tan δ_m) of the BNKLT samples was about 4196 and 0.141, respectively. The ε_m and tan δ_m values for other compositions ($0.1 \leq x \leq 0.4$) was not observed, which is ascribed to the increase in the electrical conductivity (126).

When considering the dielectric properties measured at 100 kHz, the ε_R and ε_m values of the 0.8BNT-0.2BF ceramics studied by K. H. Ryu et al. were about 500 and 1900, respectively (29). In the present study, the ε_R, tan δ_R, ε_m and tan δ_m values of the 0.8BNKLT-0.2BBF ceramics were about 1069, 0.0519, 5457 and 0.0349, respectively which is higher than previously reported. These results suggest that the addition of BBF content is a good candidate to improve the dielectric properties of BNT-based ceramics.

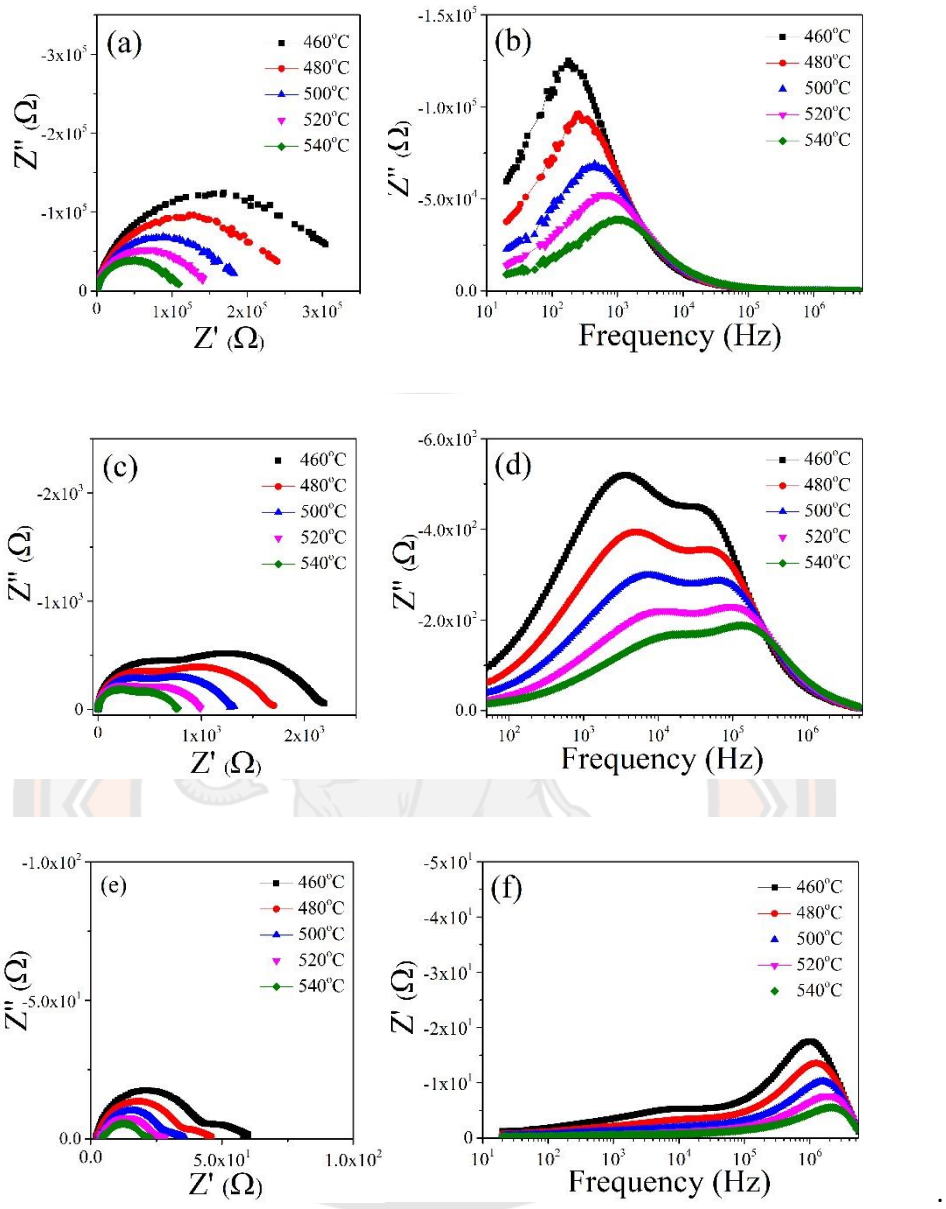

Figure 80 Complex impedance spectra of (1-x)BNKLT-xBBF ceramics as a function of temperature from 20 Hz to 5 MHz; (a)-(b) x=0, (c)-(d) x=0.2 and (e)-(f) x=0.4

To more clearly see the effect of BBF content on the conduction mechanism and the electrical microstructure of BNKLT ceramics, impedance spectroscopy (IS) measurements were conducted at selected compositions (e.g., x=0, 0.2, and 0.4) at different temperatures (460-540°C) and frequencies (20 Hz to 5 MHz). The complex

impedance plane (Z*, Z′ vs. Z″) and the corresponding Z″ spectroscopy (imaginary part of impedance [Z″] vs. frequency) data of each composition were plotted and are shown in Figure 80 (a-f). For the BNKLT ceramic (Figure 80 (a)), a semicircle and a broad Debye-like peak (Figure 80 (b)) in the spectroscopic plot were observed in all temperature measurements, implying a non-Debye type relaxation with several relaxation times in the materials. At x=0.2 (Figure 80 (c)), the Z* plot exhibited two semicircles at all temperatures: 1) at low frequencies, a relative large distorted semicircle corresponding to the resistivity at the grain boundaries and 2) at higher frequencies a much smaller semicircle caused by the resistivity of the bulk. The corresponding Z″ spectroscopic plot (Figure 80 (d)) also presented two Debye-like peaks, suggesting that the (1-x)BNKLT-xBBF ceramics at x=0.2 are electrically inhomogeneous. When x increased up to 0.4, both the Z* (Figure 80 (e)) and Z″ spectroscopic plots (Figure 80 (f)) showed similar features to the 0.8BNKLT-0.2BBF sample, indicating that the electrically inhomogeneous microstructure persisted. Moreover, both bulk and grain boundary resistivity continuously decreased when the BBF content increased, suggesting that the samples become more conductive. This behavior can be explained by an increase in compensating oxygen vacancies which arise from the substitution of Fe^{3+} into B-sites (Ti^{4+}) as written in the equation (27). In addition, the resistivity of (1-x)BNKLT-xBBF ceramics decreased with an increase in temperature, confirming the negative temperature coefficient of resistance (NTCR) behavior.

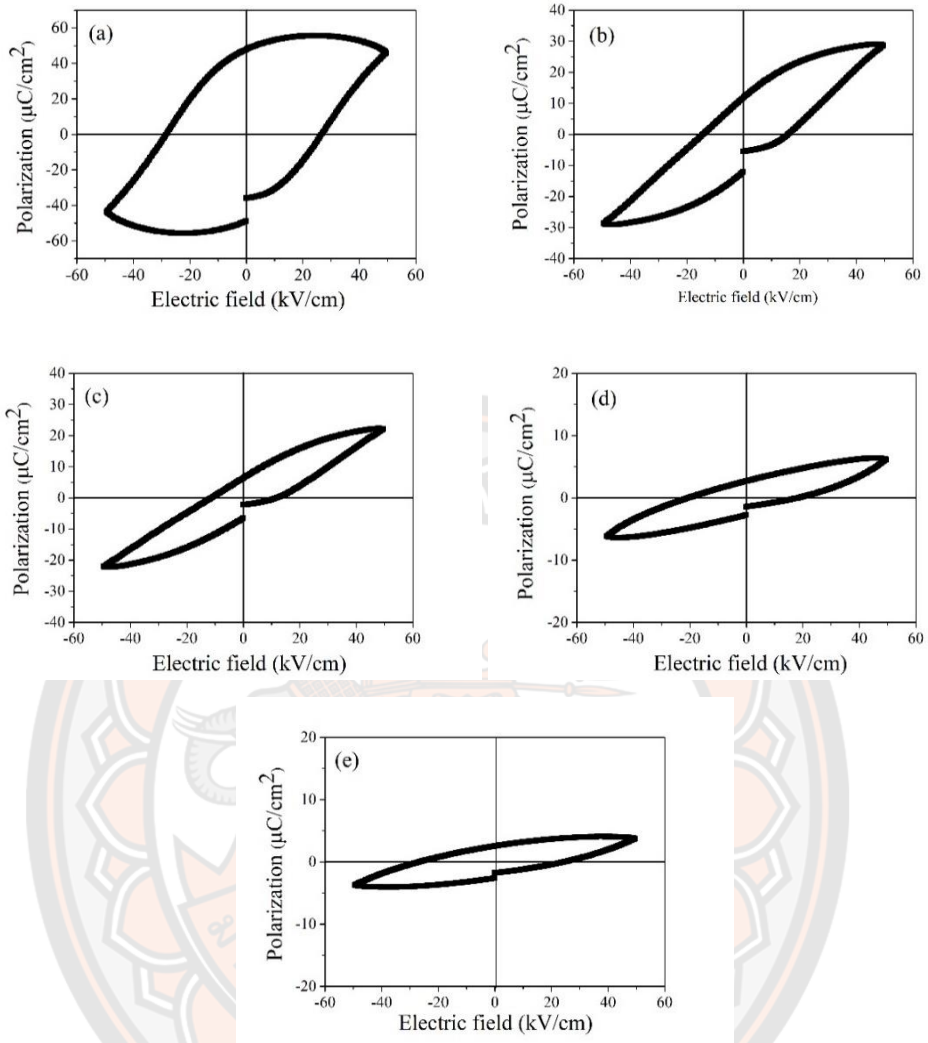

Figure 81 Polarization measurement as a function of electric field at room-temperature of (1-x)BNKLT-xBBF ceramics with (a) x=0, (b) x=0.1, (c) x=0.2, (d) x=0.3 and (e) x=0.4

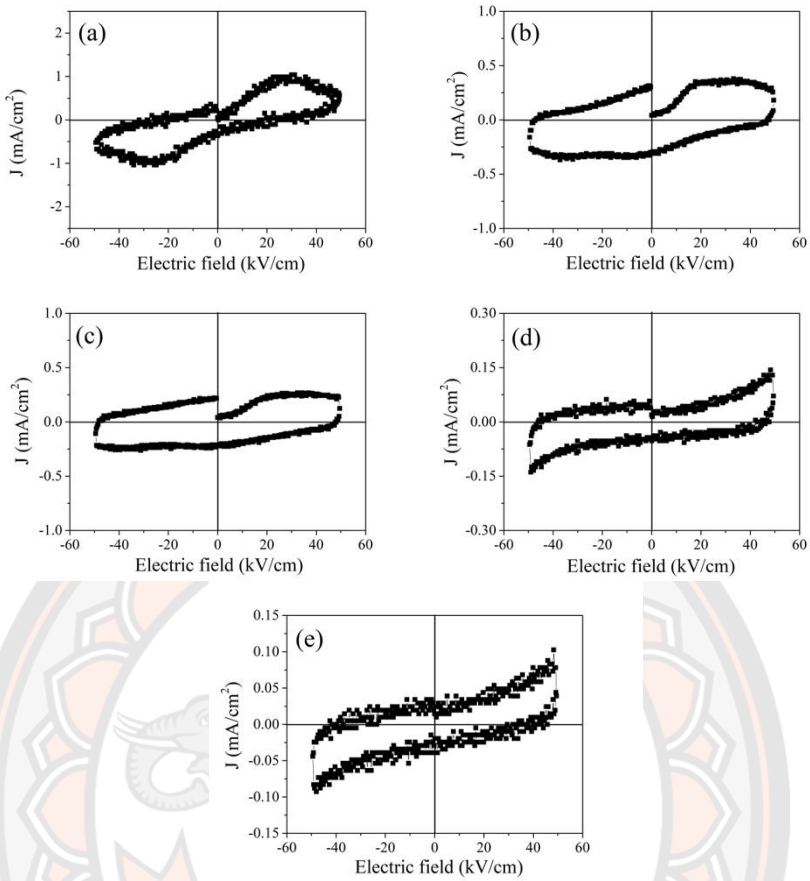

Figure 82 Room temperature polarization current intensity-electric field loops of the (1-x)BNKLT-xBBF ceramics (a) x=0, (b) x=0.1, (c) x=0.2, (d) 0.3 and (e) x=0.4

Figure 81 (a)-(e) shows the room temperature polarization hysteresis loops (P-E loops) of (1-x)BNKLT-xBBF ceramics with x=0-0.4 measured under an electric field of 50 kV/cm. The P-E loops of the BNKLT ceramics exhibited saturated and symmetric loops, which corresponds to normal ferroelectric behavior. Meanwhile, the P-E loops of the (1-x)BNKLT-xBBF ceramics with x=0.1-0.4 become much slim, indicating that the appearance of typical ferroelectric relaxor behaviors (127-129). To be more clearly, the polarization current intensity-electric field (J-E) curves is an effective way to observe the reorientation of polarization and measure ferroelectric properties by distinguishing the contribution of linear capacitance, electric conductivity and domain switching (127). Figure 82 (a)-(e) demonstrates the J-E

curves of (1-x)BNKLT-xBBF ceramics. It was found that the BNKLT ceramic exhibited two sharp current peaks symbolizing domain switching which indicated the normal ferroelectric behavior. When x=0.1-0.4, the J-E curves showed broad peaks and flat peaks at the nonergodic state which correspond the ferroelectric domain reversal and relaxor behaviors (127-129). The values of the remnant polarization (P_r) and coercive field (E_c) of (1-x)BNKLT-xBBF ceramics are listed in Table 11. The P_r and E_c values of the BNKLT ceramic was about 47 μC/cm^2 and 28 kV/cm, respectively. When increasing x from 0.1 to 0.4, the P_r value continuously decreased, which might arise from the suppression of the ferroelectric properties of the (1-x)BNKLT-xBBF ceramics. The E_c value decreased with x content up to 0.2 and then increased. The weakened ferroelectric properties in these samples may be explained by the pinning effect on domain reversal due to the increase oxygen vacancies with increasing x (127, 128). In this study, an excellent P_r value (6.46 μC/cm^2) and the lowest E_c value (11.84 kV/cm) were obtained from 0.8BNKLT-0.2BBF ceramics. These properties were observed because this sample possessess a compact microstructure and have the highest relative density.

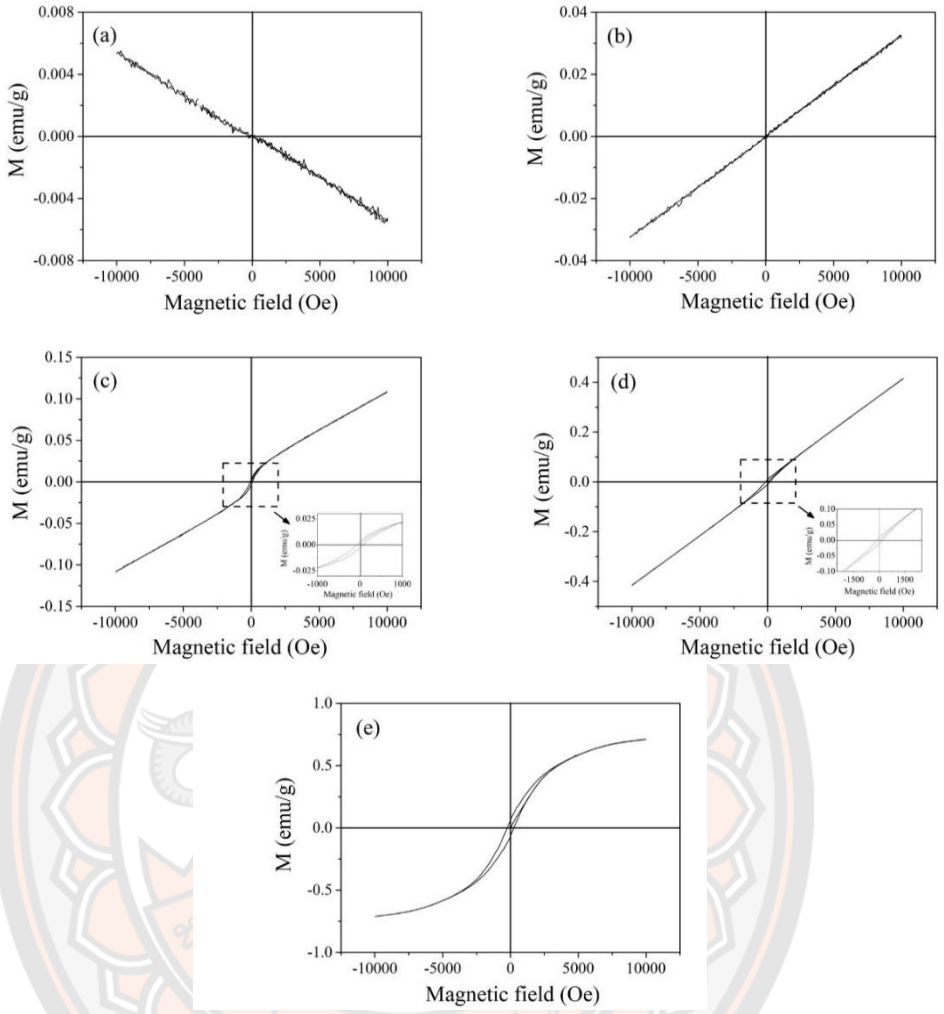

Figure 83 Magnetic hysteresis loop for (1-x)BNKLT-xBBF ceramics recorded at room temperature, with (a) x=0, (b) x=0.1, (c) x=0.2, (d) x=0.3 and (e) x=0.4

Figure 83 (a)-(e) shows the room temperature magnetization (M) versus magnetic field (H) (M-H curves) of (1-x)BNKLT-xBBF ceramics, using the maximum magnetic field of ±10 kOe. It was found that the BNKLT sample (Figure 83 (a)) exhibited a linear relationship with a negative slope indicating diamagnetic behavior. At x=0.1 (Figure 83 (b)), the slope of the graphs changed from negative to positive implying paramagnetic behavior. The origin of the paramagnetic behavior for the 0.9BNKLT-0.1BBF ceramic could be attributed to the large distance between neighboring Fe ions within the BNKLT matrix which could not establish magnetic exchange interactions (130). When x increased from 0.2 to 0.4, the samples exhibited

a hysteresis M-H behavior (Figure 83 (c)–(e)), with the increasing remnant magnetization (M_r) and coercive field (H_c) with increasing x as listed in Table 11. This enhanced ferromagnetism (FM) behavior of the samples should be explained by the substitution-induced suppression of the spiral spin modulation by the oxygen vacancies, which is due to the replacement of Ti^{4+} ions by Fe^{3+} ions in the lattice (131). The 0.8BNKLT-0.2BBF ceramic exhibited an excellent remnant magnetization (M_r=0.002 emu/g) and the lowest coercive field (H_c=110 Oe) at 10kOe. It was found that the H_c value of this sample was lower than the 0.8BNT-0.2BBF ceramic (H_c=354.51 Oe) which was measured at the magnetic field range of ±6 kOe (33). However, the M_r value of the 0.8BNT-0.2BBF ceramic was higher than the M_r value of the 0.8BNKLT-0.2BBF ceramic. One possible explanation might be because the complexity of BNKLT ceramics is higher than BNT ceramics leading to inhibit of the ferromagnetic behavior. We have found that the addition of 0.2BBF content in BNKLT ceramics improved the densification, dielectric, ferroelectric and magnetic properties. Moreover, the presentation of multiferroic behavior means these ceramics can be effective in multifunctional devices.

Table 11 Average grain size, density, transition temperature, electric and magnetic properties of (1-x)BNKLT-xBBF ceramics

x	Average grain size (μm)	Measured density (g/cm^3)	Relative density (%)	ε_R	tan δ_R	P_r ($\mu C/cm^2$)	E_c (kV/cm)	M_r (emu/g)	H_c (Oe)
0	0.42±0.02	4.81	80.41	1175	0.068	47	28	-	-
0.1	2.80±0.41	5.79	93.14	1264	0.0269	11.89	14.23	-	-
0.2	3.24±0.41	6.16	95.48	1746	0.0296	6.46	11.84	0.002	110
0.3	9.67±0.82	6.35	94.87	822	0.0447	2.72	20.96	0.012	136
0.4	14.96±1.35	6.45	93.09	819	0.0840	2.55	26.9	0.077	238

Multiferroic properties of lead-free (1-x)($K_{0.44}Na_{0.52}Li_{0.04}$)($Nb_{0.84}Ta_{0.10}Sb_{0.06}$)$O_3$-x$Bi_{0.8}Ba_{0.2}FeO_3$ ceramics prepared via the solid-state combustion technique

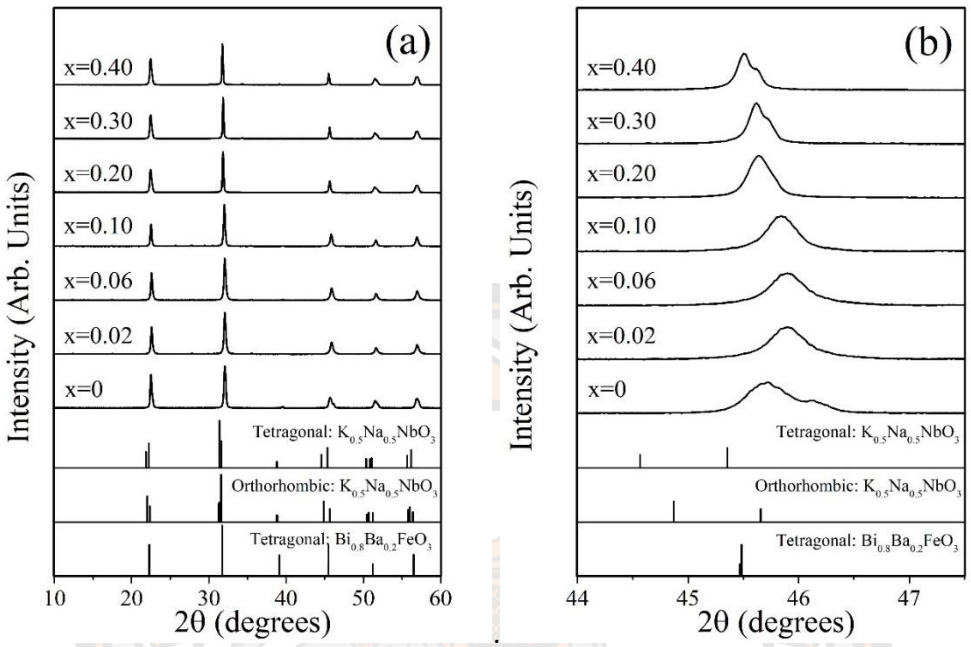

Figure 84 (a) XRD patterns of the (1-x)KNLNTS-xBBF ceramics in the 2θ range of (a) 10-60º and (b) 43.5-47.5º

The XRD patterns of (1-x)KNLNTS-xBBF ceramics with x=0-0.4 in the 2θ range of 10-60º are displayed in Figure 84 (a). It can be observed that all samples exhibited a pure perovskite phase. The enlarged XRD patterns of the peaks in the 2θ range of 43.5-47.5º are shown in Figure 84 (b). Generally, the orthorhombic structure (O) is identified by split peaks of (202) and (020) at a 2θ around 45º corresponding to JCPDS 71–2171 (132). The tetragonal structure (T) is characterized by the dual peaks of (002) and (200) at a 2θ around 45º, corresponding to JCPDS 71-0945 (133), where the KNLNTS ceramics presented dual board peaks. The dual broad peaks began to merge when the x increased from 0 to 0.2 and then split again with x>0.2 (Figure 77 (b)), which indicated the coexisting O and T phases. Moreover, it was observed that the peaks of the sample shifted to lower angles, suggesting expansion of the unit cell volume.

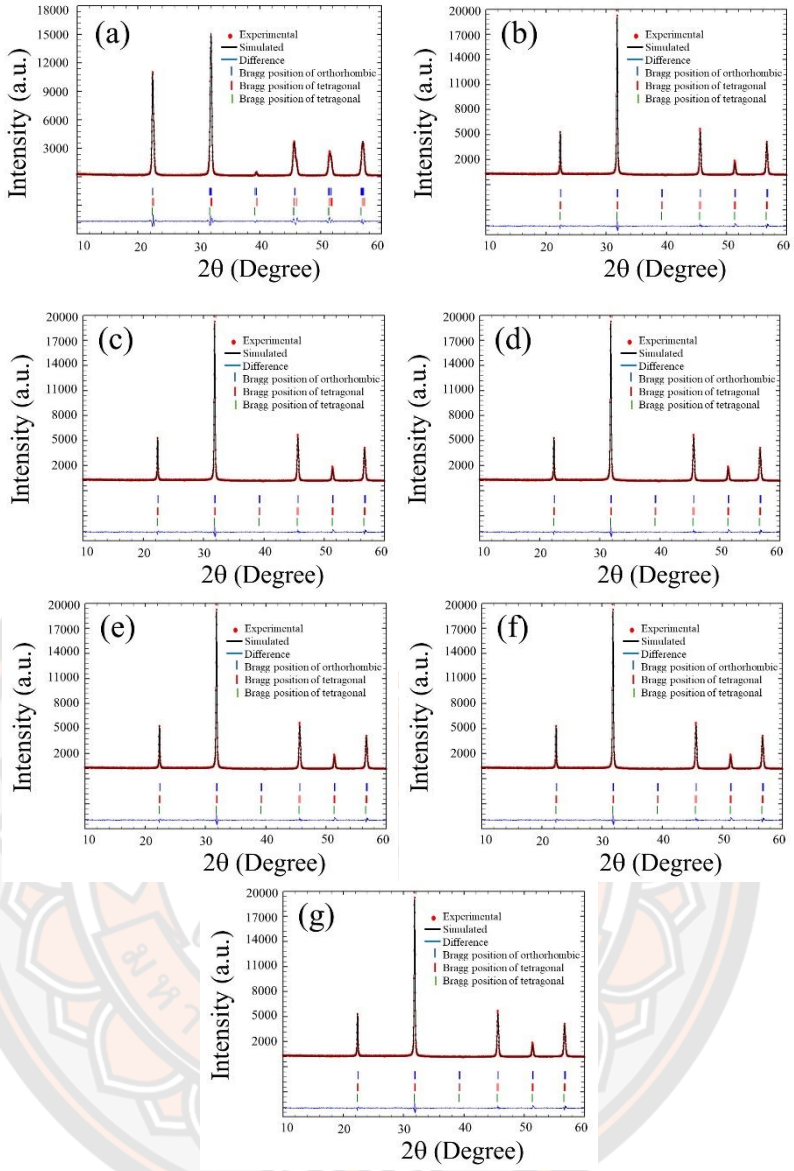

Figure 85 XRD patterns with the Rietveld refinement fitting for the (1-x)KNLNTS-xBBF ceramics of (a) x=0, (b) x=0.02, (c) x=0.06, (d) x=0.1, (e) x=0.2, (f) x=0.3 and (g) x=0.4

Rietveld refinement was used to analyze the quantity of each phase. Figure 85 (a)-(b) displayed the Reitveld refinement fits of (1-x)KNLNTS-xBBF ceramics with x=0 and 0.2. The Rietveld refinement fits were carried out by the Fullprof program. The initial parameters for the cell parameters, lattice parameters, space group and atomic functional positions were taken from the reference patterns calculated from the Crystallography Open Database (COD). $K_{0.5}Na_{0.5}NbO_3$ was used for the structural

model of the orthorhombic phase, with an Amm2 space group (112), while $K_{0.3}Na_{0.7}NbO_3$ and $Bi_{0.8}Ba_{0.2}FeO_3$ were used for the tetragonal (P4mm) phase (112, 133) for all samples. A Chebyshev function was used to create the background signal and a Psudo-Voigt function (combination of Gaussian and Lorentzian function) was used to fit the diffraction peaks (113). For the Rietveld refinement, the profile reliability (R_p), the weight pattern reliability (R_{wp}), the expected residual (R_{exp}) and the goodness of fit (χ^2) can be expressed as follows (113)

$$R_p = 100\frac{\sum|y_{oi} - y_{ci}|}{\sum y_{oi}} \quad (28)$$

$$R_{wp} = 100\left\{\frac{\sum w_i\left(y_{oi} - y_{ci}\right)^2}{\sum w_i\left(y_{oi}\right)^2}\right\}^{1/2} \quad (29)$$

$$R_{\exp} = 100\left\{\frac{\left(N - P + C\right)}{\sum w_i\left(y_{oi}\right)^2}\right\}^{1/2} \quad (30)$$

$$\chi^2 = \frac{R_{wp}}{R_{\exp}} \quad (31)$$

Where w_i the statistical weight and y_{oi} and y_{ci} are observed and calculated intensities for the diffraction angle $2\theta_i$. N is the total number of data points, P is the number of adjustable parameters and C is the number of constraints applied (134). Good agreement between the experimental peak shape and the simulated values were obtained based on the relatively low R_p, R_{wp}, R_{exp} values (<15%) and χ^2 value (<4) (Table 12). The fitted structural parameters for all compositions are listed in Table 11. The fitting results confirmed that all samples had coexisting orthorhombic and tetragonal phases, with the percentage of tetragonal phase increased with increasing x content (Table 12). Moreover, it was observed that the unit cell volume increased with increased x, which corresponded to the shift to lower angles for the peak positions (Figure 84 (b)). The expansion of unit cell volume can explain by the substitution of Ba^{2+} (1.61 Å) into Na^+ (1.39 Å)/Li^+ (0.76 Å) at A-sites and Fe^{3+} (0.645 Å) into Nb^{5+} (0.64 Å)/Ta^{5+} (0.64 Å) at B-sites (109).

Table 12 Rietveld structural refinement results for the (1-x)KNLNTS-xBBF ceramics

x	Goodness of fit	Phase structure	Profile parameters	Atoms information					The percentage of phase
				Label	x	y	z	Occ.	
0	χ^2=2.89 R_p=10.3 R_{wp}=11.1 R_{exp}=6.50	Amm2	a=3.950 Å b= 5.606 Å c= 5.635 Å V= 124.82 Å^3 u= 1.113 v= -0.311 w= 0.041	K	0.5	0	0.484	0.227	52.1
				Na	0.5	0	0.484	0.221	
				Li	0.5	0	0.484	0.014	
				Nb	0	0	0	0.360	
				Ta	0	0	0	0.049	
				Sb	0	0	0	0.029	
				O1	0.5	0	0.073	0.884	
				O2	0	0.299	0.271	1.189	
		P4mm	a= 3.946 Å c= 3.977 Å V= 61.945 Å^3 u= 0.712 v= 0.407 w= 0.285	K	0.5	0	0	0.205	47.9
				Na	0.5	0	0	0.218	
				Li	0.5	0	0	0.028	
				Nb	0	0.5	0.492	0.419	
				Ta	0	0.5	0.492	0.050	
				Sb	0	0.5	0.492	0.029	
				O1	0.5	0.5	0.038	1.490	
				O2	0.5	0	0.038	0.905	
0.02	χ^2=2.09 R_p=13.8 R_{wp}=12.2 R_{exp}=8.45	Amm2	a=3.950 Å b= 5.606 Å c= 5.635 Å V= 124.82 Å^3 u= 1.113 v= -0.311 w= 0.041	K	0.5	0	0.484	0.227	34.2
				Na	0.5	0	0.484	0.221	
				Li	0.5	0	0.484	0.014	
				Bi	0.5	0	0.484	0.012	
				Ba	0.5	0	0.484	0.005	
				Nb	0	0	0	0.360	
				Ta	0	0	0	0.049	
				Sb	0	0	0	0.029	
				Fe	0	0	0	0.010	
				O1	0.5	0	0.073	0.884	
				O2	0	0.299	0.271	1.189	
		P4mm	a= 3.946 Å c= 3.977 Å V= 61.945 Å^3 u= 0.712 v= 0.407 w= 0.285	K	0.5	0	0	0.205	65.8
				Na	0.5	0	0	0.218	
				Li	0.5	0	0	0.028	
				Bi	0.5	0	0	0.013	
				Ba	0.5	0	0	0.004	
				Nb	0	0.5	0.492	0.419	
				Ta	0	0.5	0.492	0.050	
				Sb	0	0.5	0.492	0.029	
				Fe	0	0.5	0.492	0.010	
				O1	0.5	0.5	0.038	1.490	
				O2	0.5	0	0.038	0.905	
0.06	χ^2=2.87 R_p=10.2 R_{wp}=11.0	Amm2	a=3.950 Å b= 5.606 Å c= 5.635 Å V= 124.82 Å^3 u= 1.113 v= -0.311	K	0.5	0	0.484	0.227	30.7
				Na	0.5	0	0.484	0.221	
				Li	0.5	0	0.484	0.014	
				Bi	0.5	0	0.484	0.021	
				Ba	0.5	0	0.484	0.009	
				Nb	0	0	0	0.360	
				Ta	0	0	0	0.049	
				Sb	0	0	0	0.029	
				Fe	0	0	0	0.003	

	R_{ex}=6.51		w= 0.041	O1	0.5	0	0.073	0.884	
				O2	0	0.299	0.271	1.189	
				K	0.5	0	0	0.205	
				Na	0.5	0	0	0.218	
			a= 3.946 Å	Li	0.5	0	0	0.028	
			c= 3.977 Å	Bi	0.5	0	0	0.025	
		P4mm	V= 61.945	Ba	0.5	0	0	0.008	69.3
			$Å^3$	Nb	0	0.5	0.492	0.419	
			u= 0.712	Ta	0	0.5	0.492	0.050	
			v= 0.407	Sb	0	0.5	0.492	0.029	
			w= 0.285	Fe	0	0.5	0.492	0.003	
				O1	0.5	0.5	0.038	1.490	
				O2	0.5	0	0.038	0.905	
				K	0.5	0	0.484	0.289	
				Na	0.5	0	0.484	0.221	
			a=3.945 Å	Li	0.5	0	0.484	0.037	
			b= 5.597 Å	Bi	0.5	0	0.484	0.042	
			c= 5.661 Å	Ba	0.5	0	0.484	0.012	
		Amm2	V= 125.010	Nb	0	0	0	0.391	19.2
			$Å^3$	Ta	0	0	0	0.050	
			u= 0.728	Sb	0	0	0	0.030	
			v= 0.276	Fe	0	0	0	0.051	
			w= 0.041	O1	0.5	0	0.073	1.267	
	χ^2=2.91			O2	0	0.299	0.271	0.873	
0.1	R_p=10.6			K	0.5	0	0	0.251	
	R_{wp}=11.4			Na	0.5	0	0	0.219	
	R_{exp}=6.66		a= 3.953 Å	Li	0.5	0	0	0.017	
			c= 3.981 Å	Bi	0.5	0	0	0.038	
		P4mm	V= 62.235	Ba	0.5	0	0	0.014	80.8
			$Å^3$	Nb	0	0.5	0.492	0.435	
			u= 0.038	Ta	0	0.5	0.492	0.050	
			v= 0.029	Sb	0	0.5	0.492	0.030	
			w= 0.008	Fe	0	0.5	0.492	0.095	
				O1	0.5	0.5	0.038	0.957	
				O2	0.5	0	0.038	1.292	
				K	0.5	0	0.484	0.231	
				Na	0.5	0	0.484	0.170	
			a=3.969 Å	Li	0.5	0	0.484	0.018	
			b=5.640 Å	Bi	0.5	0	0.484	0.079	
			c= 5.589 Å	Ba	0.5	0	0.484	0.020	
		Amm2	V= 125.145	Nb	0	0	0	0.317	14.4
			$Å^3$	Ta	0	0	0	0.050	
			u= 0.089	Sb	0	0	0	0.029	
			v= 0.014	Fe	0	0	0	0.099	
	χ^2=1.91		w= 0.010	O1	0.5	0	0.073	1.077	
0.2	R_p=12.9			O2	0	0.299	0.271	0.968	
	R_{wp}=11.7			K	0.5	0	0	0.211	
	R_{exp}=8.45			Na	0.5	0	0	0.169	
			a= 3.950 Å	Li	0.5	0	0	0.019	
			c= 3.991 Å	Bi	0.5	0	0	0.080	
		P4bm	V= 62.298	Ba	0.5	0	0	0.019	85.6
			$Å^3$	Nb	0	0.5	0.492	0.309	
			u= 0.791	Ta	0	0.5	0.492	0.048	
			v= -0.205	Sb	0	0.5	0.492	0.030	
			w= 0.210	Fe	0	0.5	0.492	0.108	
				O1	0.5	0.5	0.038	0.826	

				O2	0.5	0	0.038	1.133	
				K	0.5	0	0.484	0.222	
				Na	0.5	0	0.484	0.220	
			a=3.956 Å	Li	0.5	0	0.484	0.021	
			b=5.609 Å	Bi	0.5	0	0.484	0.112	
			c=5.641 Å	Ba	0.5	0	0.484	0.040	
		Amm2	V= 125.202	Nb	0	0	0	0.419	9.3
			$Å^3$	Ta	0	0	0	0.050	
			u= 0.092	Sb	0	0	0	0.030	
			v= 0.070	Fe	0	0	0	0.142	
	χ^2=2.96		w= 0.001	O1	0.5	0	0.073	1.101	
0.3	R_p=9.67			O2	0	0.299	0.271	1.046	
	R_{wp}=10.7			K	0.5	0	0	0.224	
	R_{exp}=6.23			Na	0.5	0	0	0.219	
			a= 3.954 Å	Li	0.5	0	0	0.013	
			c= 3.997 Å	Bi	0.5	0	0	0.123	
		P4mm	V= 62.512	Ba	0.5	0	0	0.028	90.7
			$Å^3$	Nb	0	0.5	0.492	0.464	
			u= 0.087	Ta	0	0.5	0.492	0.050	
			v= 0.089	Sb	0	0.5	0.492	0.030	
			w= 0.001	Fe	0	0.5	0.492	0.155	
				O1	0.5	0.5	0.038	0.995	
				O2	0.5	0	0.038	0.921	
				K	0.5	0	0.484	0.247	
				Na	0.5	0	0.484	0.220	
			a= 3.972 Å	Li	0.5	0	0.484	0.050	
			b= 5.625 Å	Bi	0.5	0	0.484	0.168	
			c= 5.618 Å	Ba	0.5	0	0.484	0.032	
		Amm2	V= 125.581	Nb	0	0	0	0.547	0.2
			$Å^3$	Ta	0	0	0	0.050	
			u= 0.107	Sb	0	0	0	0.030	
			v= 0.115	Fe	0	0	0	0.253	
	χ^2=2.75		w= 0.007	O1	0.5	0	0.073	1.203	
0.4	R_p=9.95			O2	0	0.299	0.271	0.885	
	R_{wp}=11.0			K	0.5	0	0	0.204	
	R_{exp}=6.62			Na	0.5	0	0	0.220	
			a= 3.974 Å	Li	0.5	0	0	0.030	
			c= 3.983 Å	Bi	0.5	0	0	0.172	
		P4mm	V= 62.935	Ba	0.5	0	0	0.035	99.8
			$Å^3$	Nb	0	0.5	0.492	0.393	
			u= 0.079	Ta	0	0.5	0.492	0.050	
			v= 0.100	Sb	0	0.5	0.492	0.030	
			w= 0.017	Fe	0	0.5	0.492	0.245	
				O1	0.5	0.5	0.038	1.074	
				O2	0.5	0	0.038	0.975	

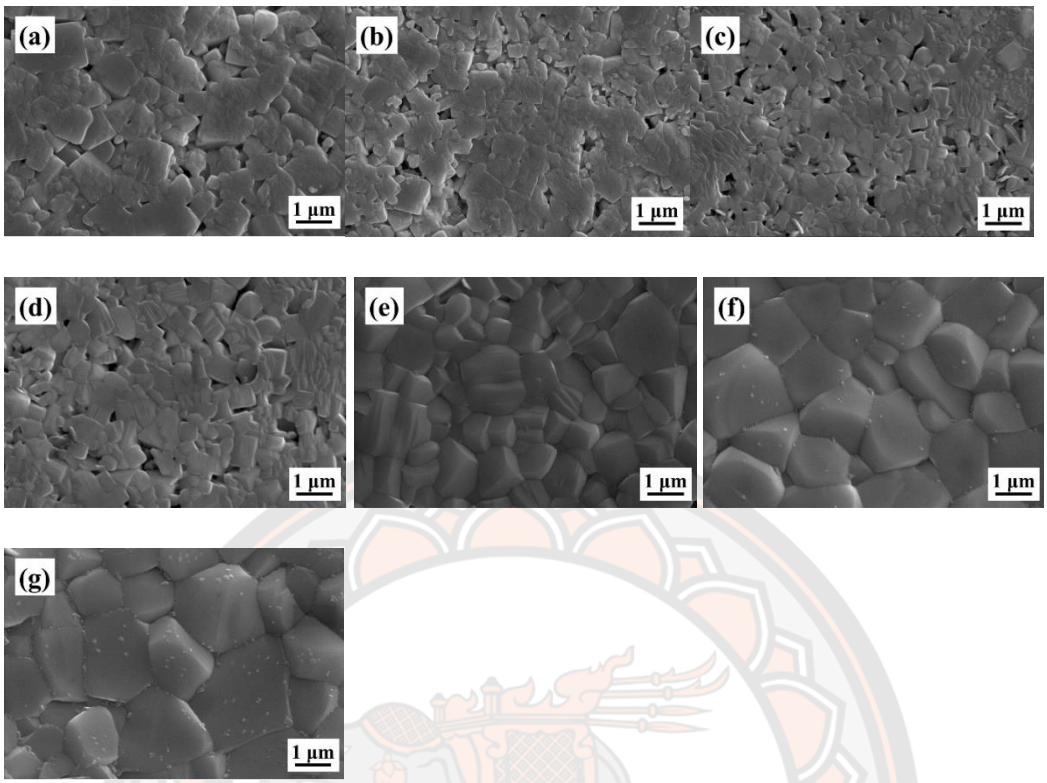

Figure 86 SEM photographs of (1-x)KNLNTS-xBBF ceramics for different x: (a) x=0, (b) x=0.02, (c) x=0.06, (d) x=0.1, (e) x=0.2, (f) x=0.3 and (g) x=0.4

SEM images of (1-x)KNLNTS-xBBF ceramics with different x content are shown in Figure 86 (a)-(g). It was found that the ceramic grains demonstrated polygonal shapes and the grain growth tended to be anisotropic. Moreover, it was found the porosity increased when x increased from 0.02 to 0.06 and then dropped. The average grain size decreased when x increased up to 0.06 and then continuously increased with further increases in x, as listed in Table 13. The density of all the ceramics was measured using Archimedes' method. The measured density and relative density dropped when x increase up to 0.06 and then continuously increased with increasing x, as listed in Table 13.

Generally, the variation of the grain size is related to the solubility of the ceramic in the liquid phase and defect chemistry (103, 104, 116). The decrease in grain size (Figure 86 (b)-(d)) can be attributed to the excess liquid phase, which hindered the grain growth, which corresponds with previous works (103, 104, 116). The accelerated grain growth was observed at x=0.2-0.4 (Figure 86 (e)-(g)). This may

be from adding cations which increased vacancies, which improved the morphology and densification. In this study, the oxygen vacancies occurred from the different valent states of the ions in the B-sites and these defects can be calculated with the following equation:

$$Fe_2O_3 \underset{M_2O_5}{\Rightarrow} 2Fe_M^{'} + 3O_O^x + 2V_O^{\cdot\cdot} \quad (32)$$

where M are the ions in B-sites (M; Nb and Ta). Therefore, it was observed that the BBF added can generate oxygen vacancies, which helps to enhance the mass transfer during the sintering process, and strongly promoted grain growth and densification (104, 116).

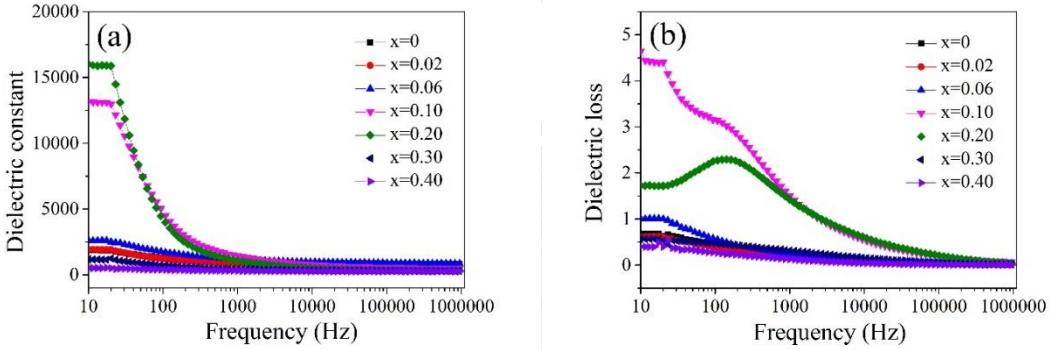

Figure 87 Variation of (a) dielectric constant and (b) dielectric loss with log frequency of (1-x)KNLNTS-xBBF ceramics

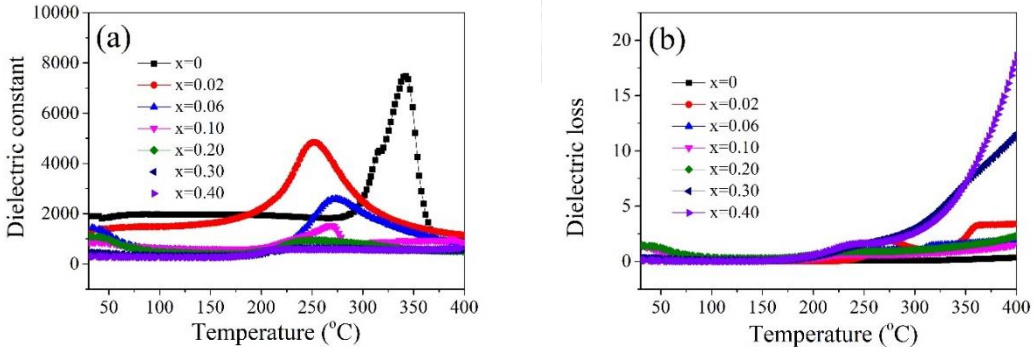

Figure 88 Temperature dependences of (a) dielectric constant and (b) dielectric loss for (1-x)KNLNTS-xBBF ceramics with different x content measured at 1 kHz

Figure 87 exhibits the room temperature (a) dielectric constant and (b) dielectric loss versus frequency (10 Hz to 10 MHz) plots of (1-x)KNLNTS-xBBF ceramics with x=0-0.4. It is well known that the dielectric constant of dielectric materials decreased rapidly with increasing frequencies, and then becomes constant at higher frequencies. At lower frequencies, the dielectric constant has a maximum value, which is related to the space charge, interfacial, ionic, orientation and electronic polarization which contributes to the higher dielectric constant at low frequencies. At higher frequencies, the dielectric constant becomes constant as the orientation declines. This behavior originates from the dipoles being hard to orient along the direction of the applied external electric field. These phenomena can attribute to the Maxwell-Wagner effect on the interfacial polarization, which is in agreement with Koop's phenomenological theory (135). It was found that the dielectric constant increased when x increased up to 0.2 and then dropped. While, the dielectric loss increased when x increased up to 0.1, it then dropped. The highest dielectric constant was obtained from the 0.8KNLNTS-0.2BBF ceramic. The enhancement of the dielectric constant effects can be understood in terms of the densification, oxygen vacancy and chemical composition results for each sample (109). However, further increases in x content (x=0.3-0.4) led to decreased dielectric constants which suggests that excessive oxygen vacancies were created (125).

Figure 88 (a)-(b) displays the temperature dependence of the dielectric constant and dielectric loss of the (1-x)KNLNTS-xBBF ceramics with different x, in the temperature range of 30-400^{o}C, measured at 1 kHz. Generally, KNN-based ceramics exhibit two obvious phase transition peaks above room temperature, these correspond to the orthorhombic-tetragonal phase transition (T_{O-T}) and the tetragonal-cubic paraelectric phase transition (T_C), respectively. The T_{O-T} values continuously decreased when x increased while the T_C values increased with increased x up to 0.1 and then dropped with further increased x content. The T_{O-T} value reduced from 64^{o}C to 35^{o}C when x increased from 0 to 0.2 (Table 12). At $x \geq 0.3$, the T_{O-T} peak disappeared, indicating the T_{O-T} shifted below room temperature. The reduction of the T_{O-T} value could be attributed to the distortion of the crystal structure and the increased amount of the tetragonal phase, which corresponds with the XRD analysis and is similar to previous reports (109). The T_C value increased with increased x

content, up to 0.1 and then decreased as listed in Table 13. Generally, the reduction of T_{O-T} and the enhancement of T_C may be caused from a partial substitution of A-site ions. While, both the reduction of T_{O-T} and T_C may be caused from a partial substitution of B-site ions (136-138). Therefore, the co-substitution of A-site and B-site ions led to the variation of T_C values. One possible reason for this phenomenon might be the fluctuation and complexity of the compositions led to both A- and B sites containing various ions. Moreover, the T_C peak became broader with the increased x, indicating that the introduction of BBF induced a diffuse phase transition in KNLNTS ceramics. The values of the dielectric constant and dielectric loss at room temperature (ε_r and tan δ at T_R) and at the Curie temperature (ε_C and tan δ at T_C) are listed in Table 13. The ε_r value and the tan δ at T_R increased when x increased up to 0.1 and then dropped as listed in Table 13. The maximum dielectric constant at T_C (ε_C) continuously decreased while the tan δ at T_C tended to increase with increased x content (Table 13). Moreover, the dielectric loss at high temperatures was found to rapidly increase, which was observed from the samples with x=0.3-0.4 (Figure 87 (b)). This behavior may be caused by defects or oxygen vacancies arising from the substitution of Fe^{3+} ions into Nb^{5+} or Ta^{5+} ions in B-sites, which corresponds to previous work (139).

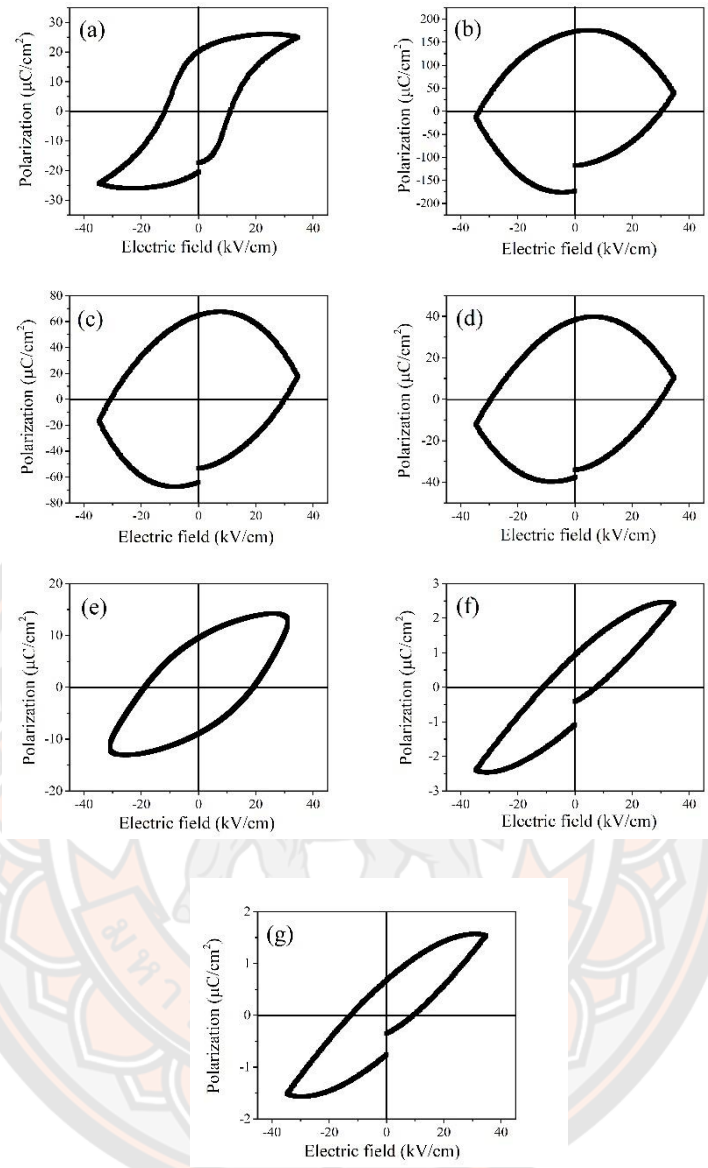

Figure 89 Ferroelectric hysteresis loops of (1-x)KNLNTS-xBBF ceramics; (a) x=0, (b) x=0.02, (c) x=0.06, (d) x=0.1, (e) x=0.2, (f) x=0.3 and (g) x=0.4

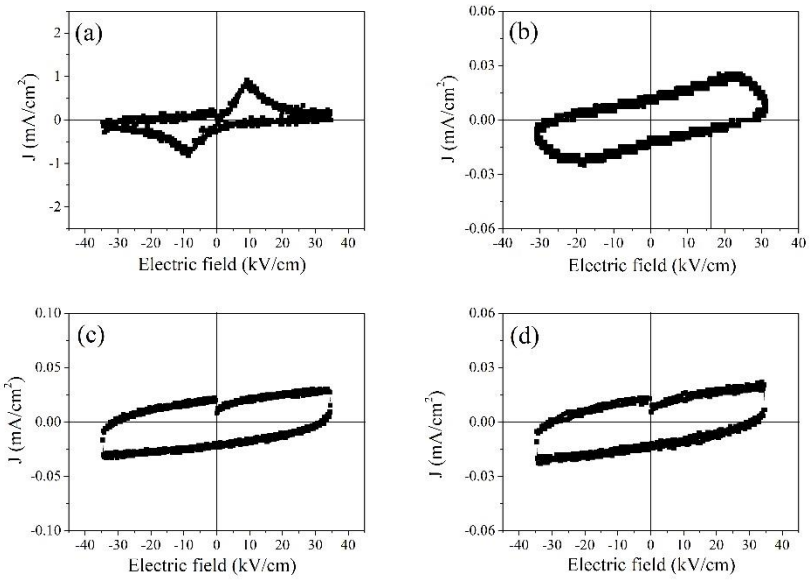

Figure 90 Room temperature polarization current intensity-electric field loops of the (1-x)KNLNTS-xBBF ceramics (a) x=0, (b) x=0.20, (c) x=0.30 and (d) 0.40

Figure 89 (a)-(g) show the P-E loops of the (1-x)KNLNTS-xBBF ceramics at room temperature, measured under an electric field of 40 kV/cm. It was found that the P-E hysteresis loop of the KNLNTS ceramic showed well saturated and symmetric loops with the P_r and E_c values of 21.21 μC/cm^2 and 12.38 kV/cm, respectively, as seen in Figure 89 (a). For x=0.02-0.2 (Figure 89 (b)-(e)), the ceramics exhibited round P-E loops, which indicated a high leakage current. At x=0.3 and 0.4, slim P-E loops accompanied with reduced leakage currents were observed (Figure 89 (f)-(g)). The P_r and E_c values decreased from 1.06 μC/cm^2 and 12.68 kV/cm to 0.67 μC/cm^2 and 7.56 kV/cm with x increased from 0.3 to 0.4. Moreover, it was found that the leakage current reduced. Therefore, the current intensity-electric field (J-E) curves is an effective way to distinguish between the contribution of linear capacitance, electric conductivity and domain switching in current electric field loops and P-E hysteresis loops (127). Figure 90 (a)-d) shows J-E curves obtained for (1-x)KNLNTS-xBBF ceramics with x=0, 0.2-0.4. KNLNTS ceramic presented two sharp currents in opposite direction which corresponding to the stabilizing domain switching indicated the normal ferroelectric behavior (128). For x=0.02-0.1, the J-E curve can not be

observed due to their large leakage current. Meanwhile, the J-E curve of x=0.2-0.4 exhibited broad peaks and flat peaks at the nonergodic state, suggesting ferroelectric domain and relaxor behaviors (129). The reasons for this observation of the P-E loops are discussed based on the density, grain size, defect structure. In the case of x=0.02-0.2, the observation could be explained by three reasons. First, low densities of these compositions were obtained, when compared with other compositions. Second, small grain size led to the large amount of grain boundary, and grain boundary induced the polarization discontinuity between grains. Third, the defects formed from the substitution of Ba^{2+} for Na^{+}/ Li^{+} at the A-sites and Fe^{3+} for Nb^{5+} /Ta^{5+} at the B-sites. For x=0.3-0.4, the increase in the density and grain size led to a decrease in the leakage current. However, the P_r and E_c values continuously decreased when compared with KNLNTS ceramic. This behavior can be attributed to the presence of trapped charge carriers and the high conductivity may be caused by the increased ferrite content. The mix valence of Fe ions between Fe^{2+} and Fe^{3+} and oxygen vacancy follows as eq. (32). Moreover, a reasonable explanation for the decreased ferroelectricity of the samples could be the presence of the ferromagnetic phase in these samples.

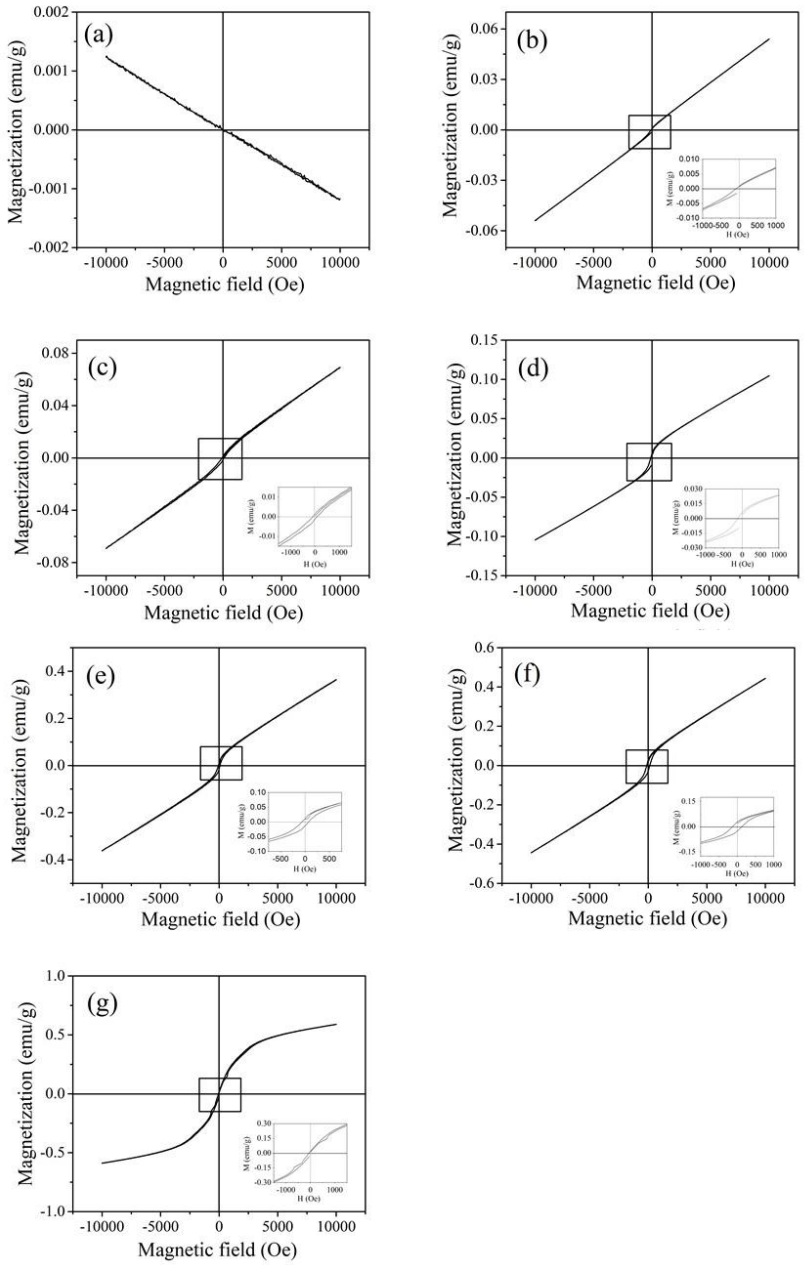

Figure 91 The magnetic M-H curves of (1-x)KNLNTS-xBBF ceramics; (a) x=0, (b) x=0.02, (c) x=0.06, (d) x=0.1, (e) x=0.2, (f) x=0.3 and (g) x=0.4

The magnetic hysteresis curves at room temperature of (1-x)KNLNTS-xBBF with x=0-0.4 ceramics are presented in Figure 91 (a)-(g). It was found that the KNLNTS ceramic exhibited diamagnetic behavior, as seen in Figure 91 (a). A weak ferromagnetic behavior was observed from the samples with x=0.02-0.4 (Figure 91

(b)-(e)). The values of the saturation magnetization (M_s), the remnant magnetization (M_r) and coercivity (H_c) are listed in Table 13. The explanation for the origin of the ferromagnetic properties can be followed three reasons. First, the origin of the oxygen vacancies which is due to the replacement of Nb^{5+} or Ta^{5+} ions by Fe^{3+} ions in B sites in the perovskite structure (131). Second, the rearrangement of the spin led to weak ferromagnetic ordering due to exchange interactions and a collapse of the space-modulated spin structure in these samples (140). Third, the structural distortions because of the increased unit cell volume of KNLNTS via the substitution of Ba^{2+} (1.61 Å) for Na^{+} (1.39 Å)/Li^{+} (0.76 Å) in the A-sites and Fe^{3+} (0.645 Å) for Nb^{5+} (0.64 Å)/Ta^{5+} (0.64 Å) in the B-site. This behavior induced weak ferromagnetic properties due to the change of the atomic bond angle between Fe-O-Fe, which led to the suppress the spin (141). It was found the M_s and M_r values continuously increased with increased x. The coercive field (H_c) was about 39-227 Oe, as listed in Table 13.

Table 13 Average grain size, density, transition temperature, electric and magnetic properties of (1-x)KNLNTS-xBBF ceramics

x	Average grain size (μm)	Measured density (g/cm^3)	Relative density (%)	To-t (°C)	ε_r	tan δ at T_R	T_C (°C)	ε_c	tan δ at T_C	M_r (emu/g)	H_c (Oe)
0	0.91±0.14	4.59	96.23	64	1889	0.22	340	7449	0.14	-	-
0.02	0.68±0.12	4.49	94.13	52	1322	0.17	253	4838	0.53	0.0016	78.96
0.06	0.51±0.17	4.42	92.56	44	1442	0.24	260	2956	0.123	0.0025	150
0.1	0.76±0.05	4.86	94.74	39	852	1.5	273	2593	0.649	0.0051	227.54
0.2	0.96±0.11	5.19	94.79	35	1091	1.41	253	942	0.897	0.023	40.43
0.3	1.43±0.11	5.54	94.95	-	451	0.31	243	633	1.464	0.039	130
0.4	1.52±0.21	5.91	95.32	-	302	0.13	225	584	1.239	0.040	39.26

Electric and magnetic properties of $Bi_{0.80}Ba_{0.20}FeO_3$ doped $Ba_{0.85}Ca_{0.15}Ti_{0.90}Zr_{0.10}O_3$ ceramics prepared via the solid-state combustion technique

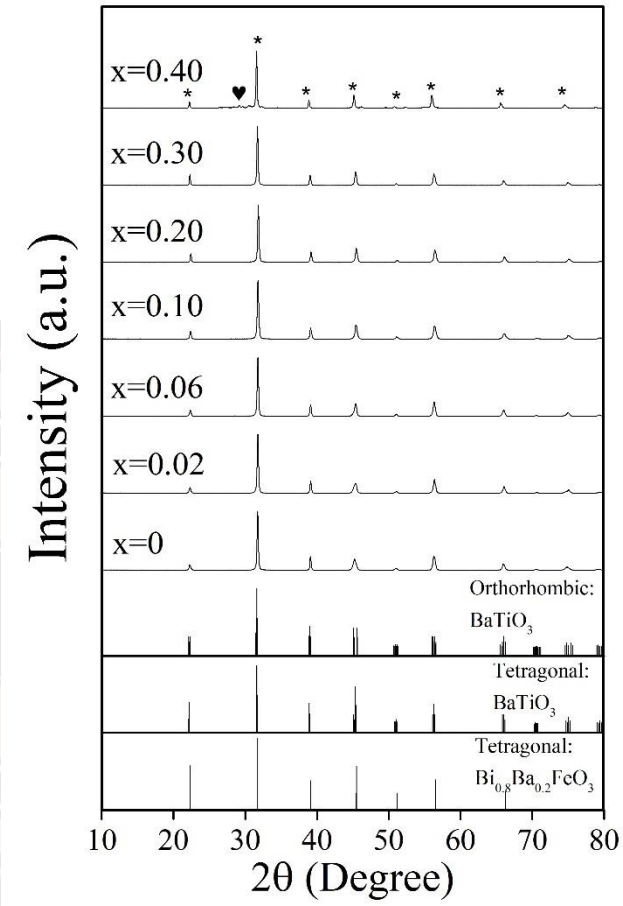

Figure 92 XRD patterns in the 2θ range of 10-80º of (1-x)BCTZ-xBBF ceramics with different x: (*) perovskite and (♥) $Bi_2Fe_4O_9$ phase

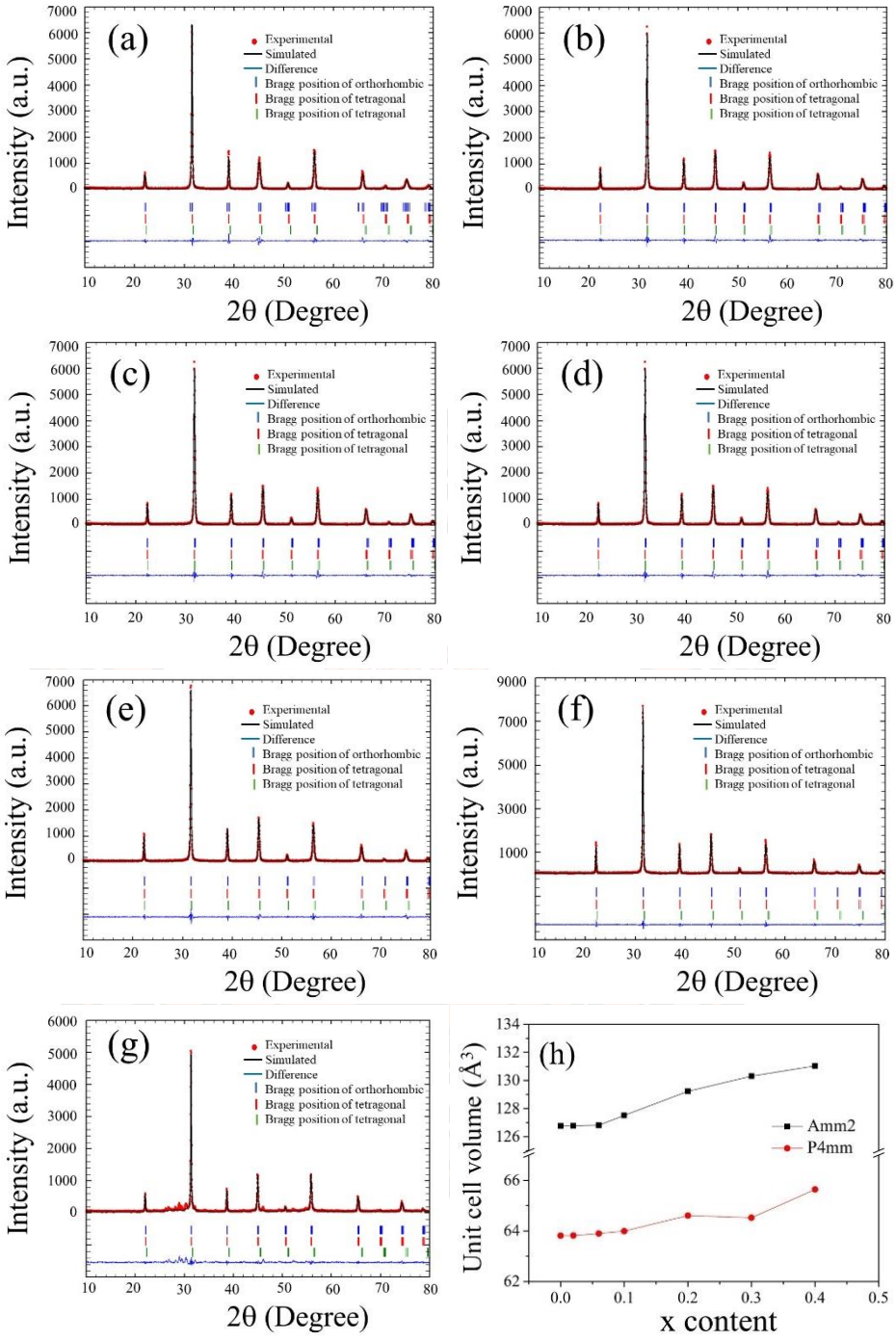

Figure 93 XRD pattern fitted by Rietveld refinement of (1-x)BCTZ-xBBF ceramics: (a) x=0, (b) x=0.02, (c) x=0.06, (d) x=0.1, (e) x=0.2, (f) x=0.3, (g) x=0.4 and (h) unit cell volume with different x content

Figure 92 presents the XRD patterns of the (1-x)BCTZ-xBBF ceramics with different x content. At $0 \leq x \leq 0.3$, the diffraction peaks could be closely matched with a single perovskite phase from the patterns of the orthorhombic phase of $BaTiO_3$ (39, 142, 143) and the tetragonal phase of $Bi_{0.8}Ba_{0.2}FeO_3$ (BBF) (112). Whereas a secondary phase was found in the XRD pattern for x=0.4 which corresponded to the $Bi_2Fe_4O_9$ phase. The purity of the perovskite structure for the x=0.4 ceramic can be calculated from the major XRD peak intensities using the following equation (33):

$$\%\ \ perovskite\ \ \ phase = \left(\frac{I_{perov}}{I_{perov} + I_{Bi_2Fe_4O_9}} \right) \times 100 \qquad (33)$$

Where, I_{perov} is the highest peak intensity of 2θ around 33° and $I_{Bi_2Fe_4O_9}$ is the highest intensity of the $Bi_2Fe_4O_9$ peak. At x=0.4, the perovskite structure was about 93.0% of the sample.

To further investigate the crystal structure and phase formation of all the samples, the Reitveld refinement, using the Fullprof software program, was performed. The crystallographic information files used were the $BaTiO_3$ file, with an orthorhombic phase (Amm2 space group) (39) and tetragonal phase (P4mm space group) (143). And to check the existence of the BBF phase, the crystallographic information file of $BiFeO_3$, with the tetragonal phase (P4mm space group) (112) was also used to fit the experimental data. Several parameters like the scale factor, background of the XRD pattern, lattice constants, profile half-width parameters (u, v and w), atomic functional positions and occupancy rates were calculated for all the samples. A Chebyshev polynomial function was used to generate the background and a Pseudo-Voigt function was used to fit the diffraction peak profiles (113). The Pseudo-Voigt function is a combination of the Lorentzian and Gaussian functions. Figure 93 (a)-(g) shows the fitting of the XRD data using the Rietveld refinement in the 2θ range of 10-80°. The Rietveld refinement parameters for all samples are listed in Table 14. The goodness of fit (χ^2) of all the samples was less than 4, suggesting a good fitting of the refined data. The O and T phases of BCTZ were obtained from the fitting result. For x=0, the percentage of the O and T phases was about 35.4 and 64.6. The ratio of T:O exhibited an increase in the T phase whereas the O phase decreased when BBF content increased from 0.02 to 0.1. After that, the percentage of the T

phase was 100% with $x \geq 0.2$ as listed in Table 1. This result indicated that the substitution of Bi^{3+}, Ba^{2+} and Fe^{3+} cations into the BCTZ lattice formed a homogenous solid solution.

The unit cell volume of the (1-x)BCTZ-xBBF ceramics increased with increased x as presented in Figure 93 (h). Generally, a change in the unit cell volume is caused by two main reasons (144-146). First, the substitution of larger ions into A- and B-sites leads to an increased lattice volume (144, 145). Second, the enhancement of the lattice volume relates to the ordering of the crystal structure and the formation of oxygen vacancies (146). It is well known that the creation of oxygen vacancies decreases the Coulomb attraction force between the anions and cations in the immediate vicinity of the elementary cell, resulting in interatomic distances increases. In our case, 85% of A-site ions were Ba^{2+} (1.64 Å) and 15% were Ca^{2+} (1.34 Å) that were substituted by 20% Ba^{2+} (1.64 Å) and 80% Bi^{3+} (1.03 Å) which could cause a decrease in the unit cell volume. The B-sites were 90% Ti^{4+} (0.605 Å) ions and 10% Zr^{4+} (0.72 Å) that were substituted by Fe^{3+} (0.64 Å) which could cause an increase in the unit cell volume. Finally, increasing the BBF content was expected to increase the oxygen vacancies, as described by equation 34.

$$Fe_2O_3 \underset{2MO_2}{\Rightarrow} 2Fe_M^{'} + 3O_O^x + V_O^{\bullet\bullet} \qquad (34)$$

Where M are the ions in B-sites (M; Ti or Zr). The expansion of the unit cell volume was dominated by Fe^{3+} ions substituting into Ti sites in the TiO_6 octahedrons which was greater than the effect of Bi^{3+} ions in the interstitial space of the TiO_6 skeleton, although there is more Bi.

Table 14 Rietveld structural refinement results for the (1-x)BCTZ-xBBF ceramics

x	Goodness of fit	Phase structure	Profile parameters	Atoms information					The percentage of phase
				Label	x	y	z	Occ.	
0	χ^2= 1.57 R_p= 12.7 R_{wp}= 16.5 R_{exp}= 13.16	Amm2	a= 3.993 Å b= 5.644 Å c= 5.622 Å u= 0.2260 v= 0.0045 w= 0.0058	Ba	0	0	0	0.50272	35.4
				Ca	0	0	0	0.07853	
				Ti	0.5	0	0.5143	0.2999	
				Zr	0.5	0	0.5143	0.00277	
				O1	0	0	0.489	1.72329	
				O2	0.5	0.2561	0.24833	1.26566	
		P4mm	a= 3.994 Å c= 3.999 Å u= 0.3042 v= 0.2255 w= 0.0106	Ba	0	0	0	0.38018	64.6
				Ca	0	0	0	0.07181	
				Ti	0.5	0.5	0.48	0.53678	
				Zr	0.5	0.5	0.48	0.05300	
				O1	0.5	0.5	0.016	1.57835	
				O2	0.5	0	0.515	1.6664	
0.02	χ^2= 1.68 R_p= 13.8 R_{wp}= 16.2 R_{exp}= 12.53	Amm2	a= 3.993 Å b= 5.644 Å c= 5.623 Å u= 0.6678 v= 0.3318 w= 0.0732	Ba	0	0	0	0.506	29.2
				Ca	0	0	0	0.067	
				Bi	0	0	0	0.039	
				Ti	0.5	0	0.5143	0.331	
				Zr	0.5	0	0.5143	0.045	
				Fe	0.5	0	0.5143	0.050	
				O1	0	0	0.489	1.289	
				O2	0.5	0.2561	0.24833	1.550	
		P4mm	a= 3.994 Å c= 4.000 Å u= 0.5609 v= 0.7814 w= 0.1048	Ba	0	0	0	0.395	70.8
				Ca	0	0	0	0.067	
				Bi	0	0	0	0.041	
				Ti	0.5	0.5	0.48	0.568	
				Zr	0.5	0.5	0.48	0.046	
				Fe	0.5	0.5	0.48	0.049	
				O1	0.5	0.5	0.016	1.740	
				O2	0.5	0	0.515	1.286	
0.06	χ^2= 1.26 R_p= 14.0 R_{wp}= 15.0 R_{exp}= 13.40	Amm2	a= 3.995 Å b= 5.635 Å c= 5.632 Å u= 0.7603 v= 0.3528 w= 0.0874	Ba	0	0	0	0.479	21.4
				Ca	0	0	0	0.057	
				Bi	0	0	0	0.029	
				Ti	0.5	0	0.5143	0.226	
				Zr	0.5	0	0.5143	0.034	
				Fe	0.5	0	0.5143	0.041	
				O1	0	0	0.489	1.362	
				O2	0.5	0.2561	0.24833	1.234	
		P4mm	a= 3.996 Å c= 3.999 Å u= 0.6141 v= 0.1959 w= 0.1931	Ba	0	0	0	0.290	78.6
				Ca	0	0	0	0.084	
				Bi	0	0	0	0.041	
				Ti	0.5	0.5	0.48	0.844	
				Zr	0.5	0.5	0.48	0.057	
				Fe	0.5	0.5	0.48	0.039	
				O1	0.5	0.5	0.016	1.513	
				O2	0.5	0	0.515	1.248	

0.1	χ^2= 1.42 R_p=12.1 R_{wp}= 14.8 R_{exp}= 12.44	Amm2	a= 3.993 Å b= 5.651 Å c= 5.649 Å u= 0.6678 v= -0.3192 w= 0.0732	Ba Ca Bi Ti Zr Fe O1 O2	0 0 0 0.5 0.5 0.5 0 0.5	0 0 0 0 0 0 0 0.2561	0 0 0 0.5143 0.5143 0.5143 0.489 0.24833	0.50586 0.06750 0.03958 0.31585 0.04459 0.05019 1.11065 1.59401	15.6
		P4mm	a= 4.000 Å c= 3.997 Å u= 0.5609 v= 0.7270 w= 0.1048	Ba Ca Bi Ti Zr Fe O1 O2	0 0 0 0.5 0.5 0.5 0.5 0.5	0 0 0 0.5 0.5 0.5 0.5 0	0 0 0 0.48 0.48 0.48 0.016 0.515	0.14149 0.06601 0.04229 0.81118 0.04595 0.05007 1.75597 1.36427	84.4
0.2	χ^2= 1.45 R_p= 14.5 R_{wp}= 16.2 R_{exp}= 13.48	Amm2	a= 4.012 Å b= 5.675 Å c= 5.674 Å u= 0.3605 v= -0.1592 w= 0.0507	Ba Ca Bi Ti Zr Fe O1 O2	0 0 0 0.5 0.5 0.5 0 0.5	0 0 0 0 0 0 0 0.2561	0 0 0 0.5143 0.5143 0.5143 0.489 0.24833	0.59933 0.10287 0.04060 0.46322 0.04469 0.05128 1.34580 1.34967	0
		P4mm	a= 4.012 Å c= 4.012 Å u= 0.5566 v= -0.1485 w= 0.0460	Ba Ca Bi Ti Zr Fe O1 O2	0 0 0 0.5 0.5 0.5 0.5 0.5	0 0 0 0.5 0.5 0.5 0.5 0	0 0 0 0.48 0.48 0.48 0.016 0.515	0.14529 0.08030 0.04283 0.58406 0.04686 0.04957 1.89287 1.79917	100
0.3	χ^2= 1.25 R_p= 13.9 R_{wp}= 15.0 R_{exp}= 13.39	Amm2	a= 4.000 Å b=5.746 Å c= 5.669 Å u= 0.5455 v= -0.3057 w= 0.0690	Ba Ca Bi Ti Zr Fe O1 O2	0 0 0 0.5 0.5 0.5 0 0.5	0 0 0 0 0 0 0 0.2561	0 0 0 0.5143 0.5143 0.5143 0.489 0.24833	0.53233 0.06738 0.03963 0.25662 0.04420 0.05000 1.14290 1.89305	0
		P4mm	a= 4.008 Å c= 4.014 Å u= 0.4728 v= 0.7994 w= 0.1740	Ba Ca Bi Ti Zr Fe O1 O2	0 0 0 0.5 0.5 0.5 0.5 0.5	0 0 0 0.5 0.5 0.5 0.5 0	0 0 0 0.48 0.48 0.48 0.016 0.515	0.11465 0.06735 0.04180 0.73406 0.04670 0.04941 2.13390 2.34579	100
	χ^2= 3.38 R_p= 28.4	Amm2	a= 4.024 Å b= 5.709 Å c= 5.703 Å u= 0.2813 v= -0.1978 w= 0.0521	Ba Ca Bi Ti Zr Fe O1 O2	0 0 0 0.5 0.5 0.5 0 0.5	0 0 0 0 0 0 0 0.2561	0 0 0 0.5143 0.5143 0.5143 0.489 0.24833	0.62557 0.06972 0.04026 0.31456 0.04317 0.05381 1.13509 1.72613	0

0.4	R_{wp}= 32.0		a= 4.035 Å	Ba	0	0	0	0.19231	
	R_{exp}=17.39		c= 4.030 Å	Ca	0	0	0	0.07320	
			u= 0.2561	Bi	0	0	0	0.04308	
		P4mm	v= 0.4296	Ti	0.5	0.5	0.48	0.88052	100
			w= 0.1120	Zr	0.5	0.5	0.48	0.04442	
				Fe	0.5	0.5	0.48	0.04659	
				O1	0.5	0.5	0.016	1.26509	
				O2	0.5	0	0.515	1.64523	

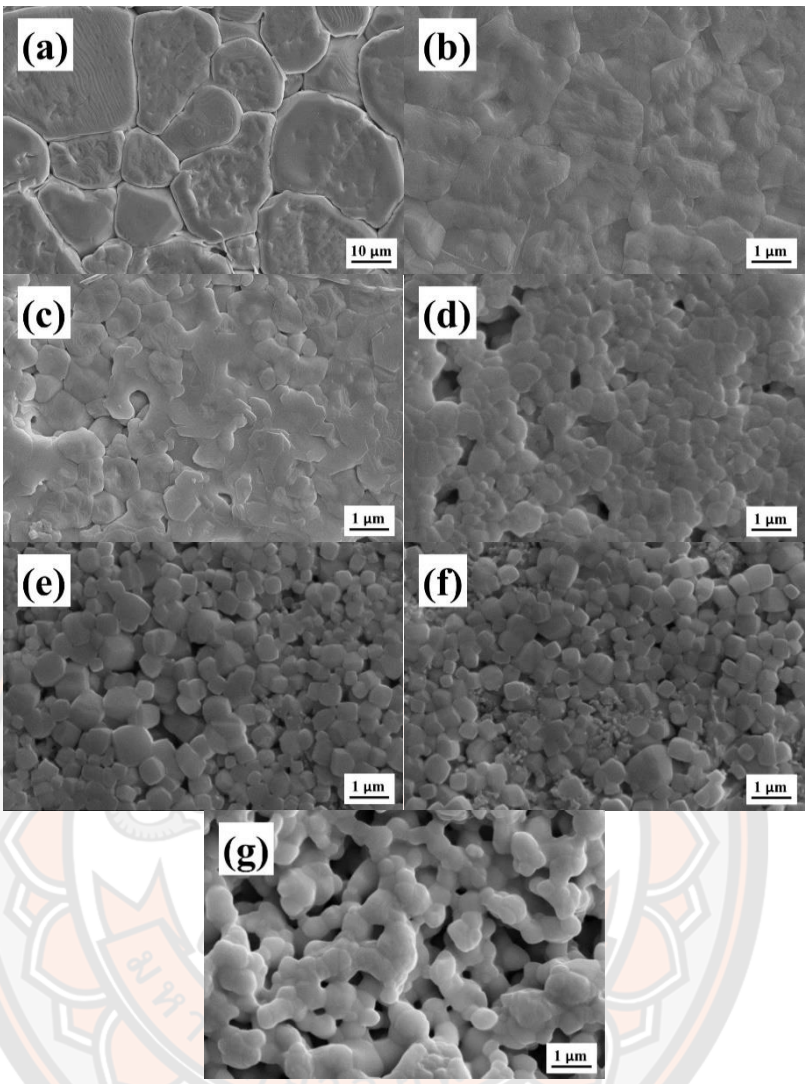

Figure 94 SEM photograph of the (1-x)BCTZ-xBBF ceramics: (a) x=0, (b) x=0.02, (c) x=0.06, (d) x=0.1, (e) x=0.2, (f) x=0.3 and (g) x=0.4

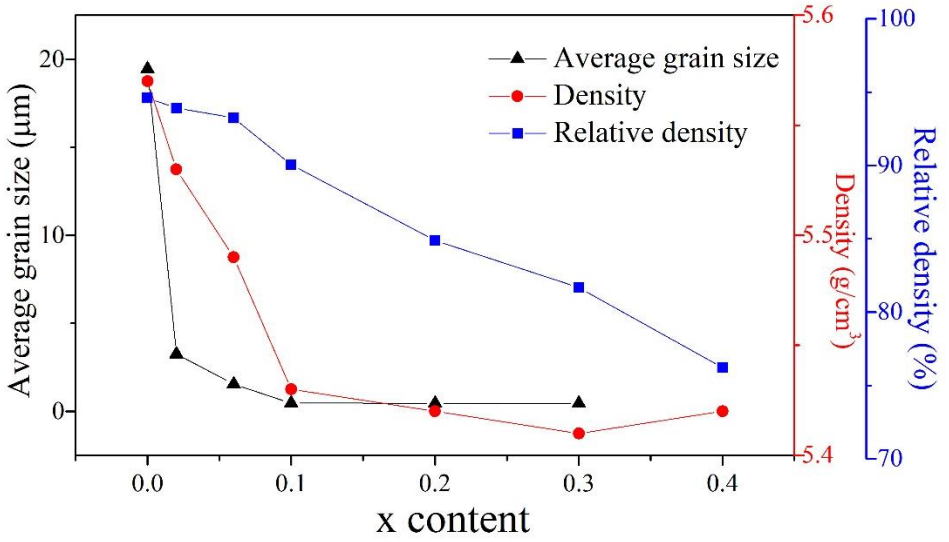

Figure 95 Average grain size, density and relative density with different x content

SEM images of the (1-x)BCTZ-xBBF ceramics after being polished and thermally etched with x=0-0.4 are shown in Figure 94 (a)-(g). The grain structure of all the samples showed a polygonal shape. The BCTZ ceramics exhibited large grains, clear grain boundaries and were closely packed while the porosity was barely observed (Figure 94 (a)). When x increased from 0.02 to 0.3, it was found that the average grain size decreased continuously, the grains of the sample presented uneven sizes, the porosity increased, and unclear grain boundaries were observed (Figure 94 (b)-(f)). For the sample with x=0.4, the grain boundaries became even more unclear and an increase in the porosity was obtained (Figure 94 (g)). The increased porosity in the sample may have been caused by the evaporation of Bi at the higher sintering temperatures, due to its low melting point (62, 147). The density and relative density continuously decreased with increased x, as shown in Figure 95. The decrease in the grain size of the (1-x)BCTZ-xBBF ceramics may be caused by the accumulation of Fe_2O_3 at the grain boundaries, which suppressed the grain growth (135, 148).

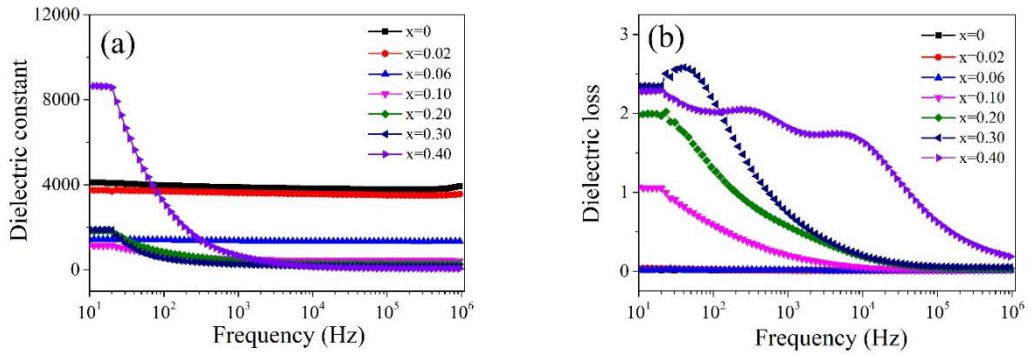

Figure 96 (a) Dielectric constant and (b) dielectric loss versus frequencies of (1-x)BCTZ-xBBF ceramics with x=0-0.4

The dielectric properties measured at room temperature, as a function of frequency, (10 Hz to 10 MHz) of (1-x)BCTZ-xBBF ceramics with different x content are presented in Figure 96 (a) and (b). It was found that the dielectric constant and loss of the x=0-0.06 ceramics was rather stable with frequency which corresponds to normal ferroelectric behavior. For the (1-x)BCTZ-xBBF ceramics with $0.1 \leq x \leq 0.4$, the maximum dielectric was obtained from low frequencies and then the dielectric continuously dropped and became more stable with higher frequencies. This phenomenon is characteristic of multiferroic materials which corresponds to the Magwell-Wagner type of heterogeneous systems (135). The dielectric constant at 10 Hz decreased with increased x content up to x=0.1 and then tended to increase with further increases in x. The dielectric loss versus frequency graph presented a relaxation peak. This related to charge carriers being trapped among the oxygen vacancies, which indicates a relatively high mobility of charge carriers (149). The relaxation peak shifted to higher frequencies with increased x, suggesting these samples exhibited a high mobility and larger leakage currents (150). Moreover, when x increased, it was found that the dielectric loss measured at 10 Hz tended to increase due to the oxygen vacancies in these samples (139).

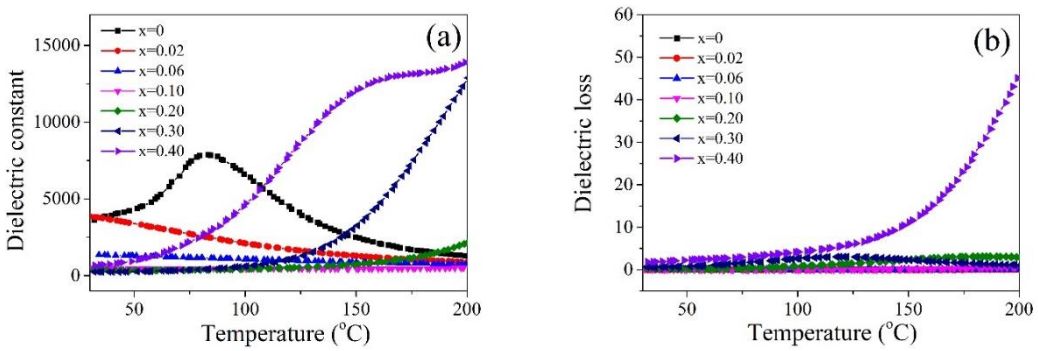

Figure 97 Variation of the dielectric property versus temperature of (1-x)BCTZ-xBBF ceramics with different x measured at 1 kHz

Figure 97 (a)-(b) shows the temperature dependence of the dielectric constant and loss of (1-x)BCTZ-xBBF ceramics with different x content. Normally, BT-based ceramics exhibit a peak which relates to the tetragonal ferroelectric-cubic paraelectric phase transition at T_C of ~120ºC. T_C was about 83ºC for the sample with x=0. At x=0.02-0.4, the T_C peaks were not observed. This behavior can be explained by the substitution of Ti^{4+} and Zr^{4+} by Fe^{3+} ions in B-sites which induced the creation of oxygen vacancies as described by equation 34. The oxygen vacancies lead to space charge polarization and higher ionic conductivity at higher temperatures (151-153). The ε_R, the dielectric loss at room temperature (tan δ_R), ε_C and dielectric loss at T_C (tan δ_C) of the BCTZ ceramic was about 3774, 0.014, 7869 and 0.009, respectively. The ε_R and tan δ_R of all the samples are listed in Table 15.

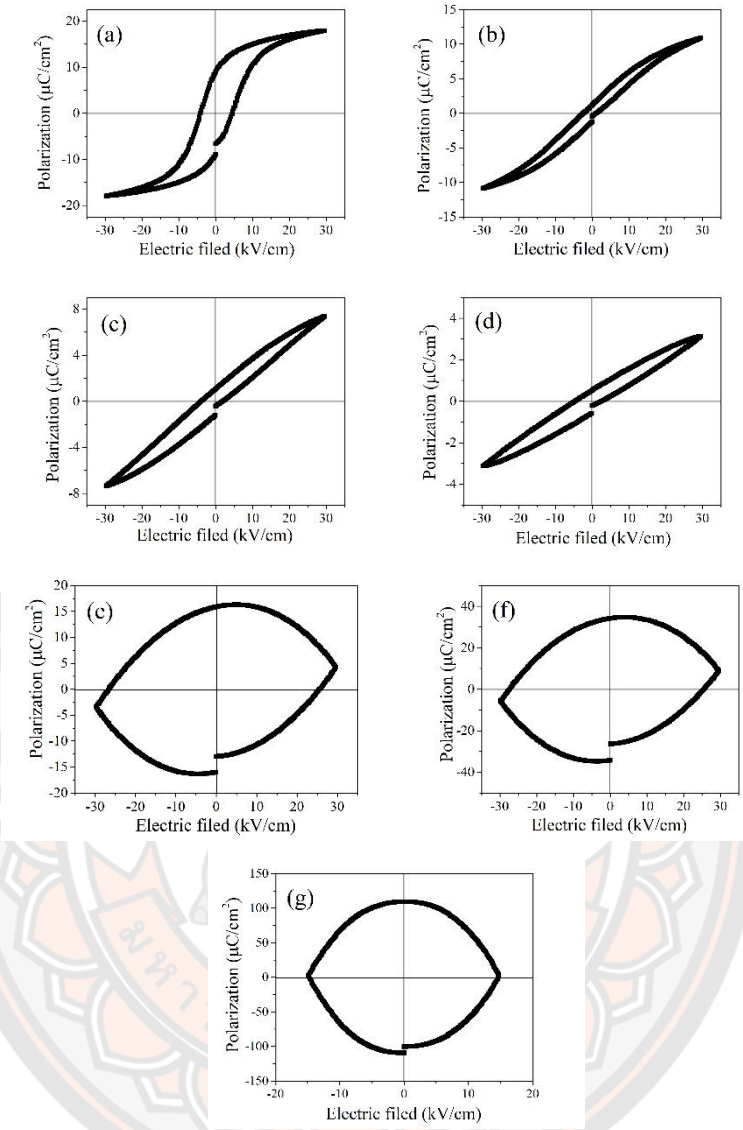

Figure 98 P-E hysteresis loops of (1-x)BCTZ-xBBF ceramics with x=0-0.40 measured at room temperature; (a) x=0, (b) x=0.02, (c) x=0.06, (d) x=0.1, (e) x=0.2, (f) x=0.3 and (g) x=0.4

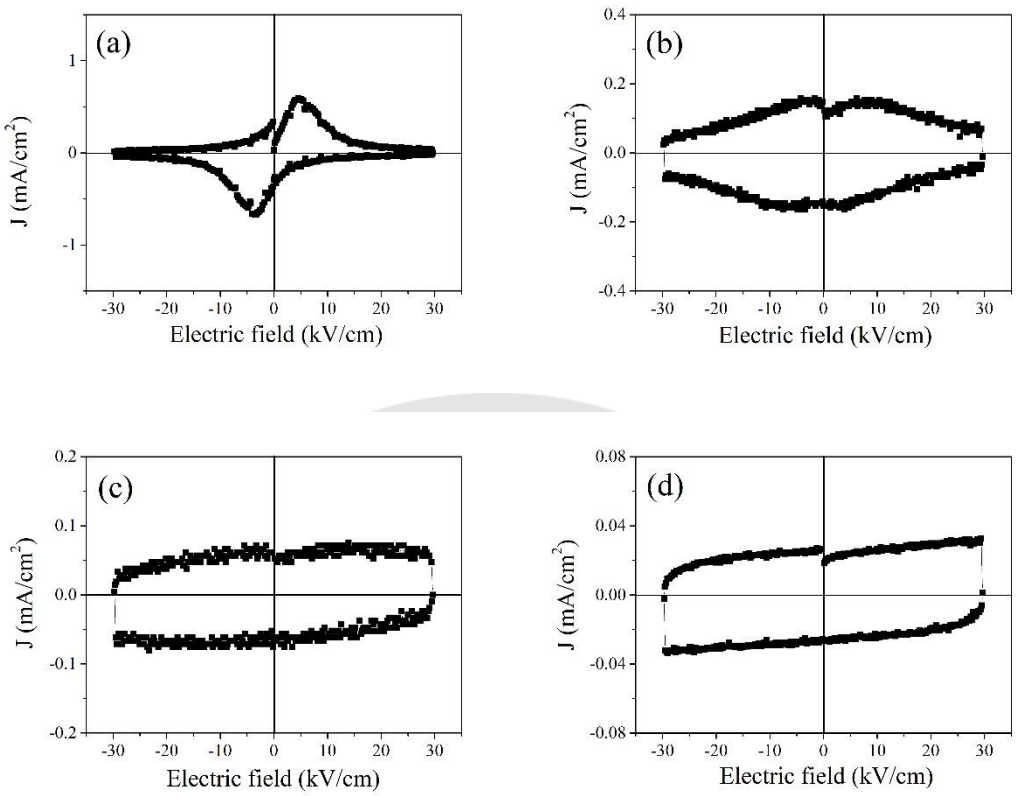

Figure 99 Room temperature polarization current intensity-electric field loops of the (1-x)BCTZ-xBBF ceramics (a) x=0, (b) x=0.02, (c) x=0.06 and (d) 0.1

Fig. 98 (a)-(g) are the polarization vs. electric field hysteresis loops for (1-x)BCTZ-xBBF ceramics with different x, measured at 30 kV/cm. The BCTZ ceramic exhibited a well saturated and symmetric P-E loop with a remnant polarization (P_r) and coercive field (E_c) of 8.94 μC/cm^2 and 4.06 kV/cm, respectively (Fig. 98 (a)). At x=0.02 (Fig. 98 (b)), ferroelectricity dramatically reduced and P_r and E_c were 1.16 μC/cm^2 and 2.39 kV/cm, respectively. As x increased, the ferroelectric was very difficult to measure and their P-E loops become more rounded (Fig. 98 (c)-(g)), which may be the origin of the increased leakage currents. To observe polarization reorientation and measure the ferroelectricity of the materials, the polarization current intensity-electric field (J-E) curve is an effective way to distinguish between contributions of electric conductivity, linear capacitance, and ferroelectric crystals (127). Fig. 99 (a)-(d) present the J-E curves of (1-x)BCTZ-xBBF ceramics with x=0-

0.1. For x=0 (Fig. 99 (a)), sharp peaks in the J-E curve were found, indicating normal ferroelectric behavior (128). The broad peaks in the J-E curve for x=0.02 (Fig. 99 (b)) was found, suggesting a relaxor ferroelectric behavior (129). For higher x (Fig. 99 (c)-(d)), the J-E curve could not be calculated because large leakage currents were observed in these samples. When x increased, the J-E curve tended to be rectangular which is characteristic of linear capacitance (127). The dramatic change of the ferroelectric behavior and creation of the leakage currents can be explained by 3 reasons. First, a decrease in the grain size led to polarization discontinuities between grains, resulting in decreased polarization. Second, the substitution of Ba^{2+}/Ca^{2+} for Bi^{3+} and Ti^{4+}/Zr^{4+} for Fe^{3+} generated oxygen vacancies or electrons to maintain the charge neutrality, which can pin the domain wall motion and suppress the ferroelectric properties. Third, the mix valence of ions in B-sites (Fe^{2+} to Fe^{3+}) lead to weakness in the ferroelectricity (127-129).

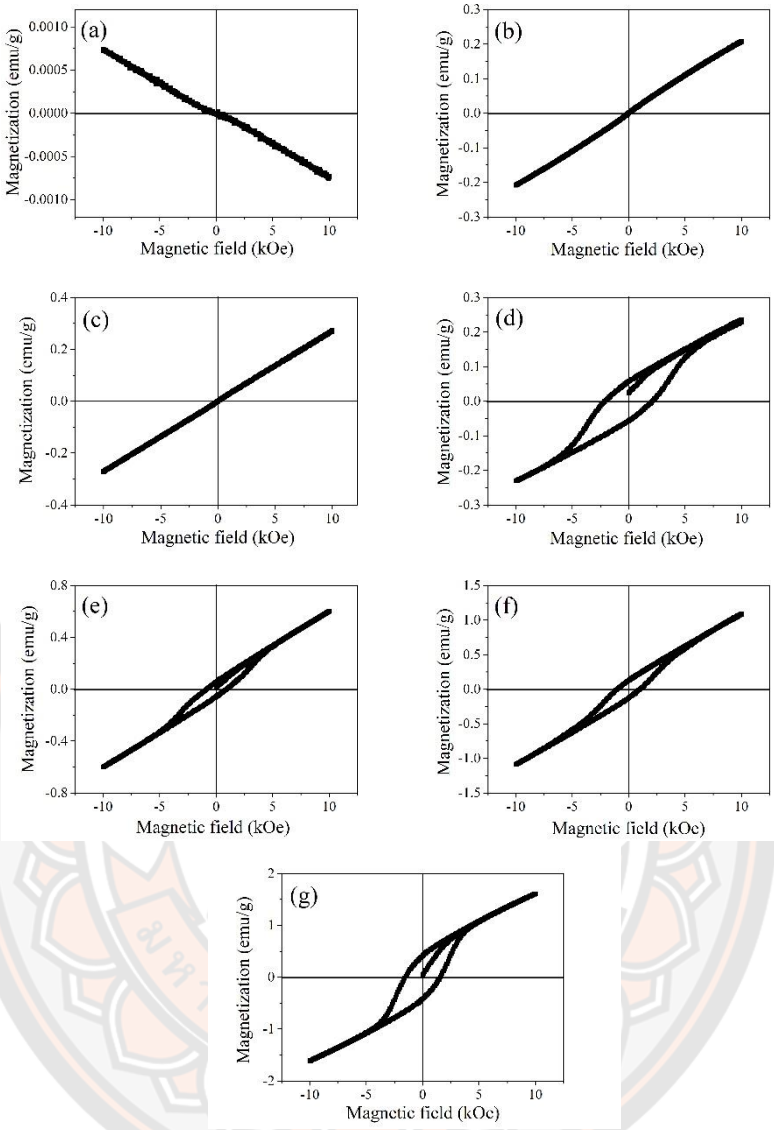

Figure 100 Magnetic property of (1-x)BCTZ-xBBF ceramics; (a) x=0, (b) x=0.02, (c) x=0.06, (d) x=0.1, (e) x=0.2, (f) x=0.3 and (g) x=0.4

The ferromagnetic properties measured at room temperature for all of the samples is shown in Figure 100 (a)-(g). Diamagnetic behavior was observed in BCTZ ceramics where the saturation magnetization (Ms) was about -0.0007 emu/g. For x=0.02 and 0.06 (Figure 100 (b)-(c)), paramagnetic behavior was found. With increased x, ferromagnetic behavior was found in all the compositions (Figure 100 (d)-(g)). The factors which could be responsible for the ferromagnetic behavior are oxygen vacancies, the magnetic exchange interaction and structural distortions (131,

140, 141). In our case, the oxygen vacancies were formed following Eq.34 which required charge compensation, which led to the suppression of the spin spiral structure (131). The addition of BBF increased the concentration of Fe^{3+} ions, resulting in increased exchange interactions between metal ions in A and B sites (140). Finally, the increase in the unit cell volume might be caused by the substitution of larger Fe^{3+} in B-sites (replacing the smaller Ti^{4+} and Zr^{4+}), leading to structure distortions in the atomic bond angles between Fe-O-Fe, which led to the suppress the spin spiral (141). The remnant magnetization (M_r) and saturation magnetization (M_s) tended to increase with increased x content (see Table 15). The magnetic field (H_c) of all samples are listed in Table 15. It was found that it decreased from 2.131 to 0.819 kOe when x increased from 0.1 to 0.2 and then increased with further increased x content.

Table 15 Dielectric and ferromagnetic properties of (1-x)BCTZ-xBBF ceramics

x	ε_R	tan δ_R	M_r (emu/g)	M_s (emu/g)	H_c (kOe)
0	3770	0.014	-	-0.0007	-
0.02	3880	0.01	-	0.207	-
0.06	1360	0.02	-	0.272	-
0.1	500	0.20	0.056	0.236	2.131
0.2	430	0.57	0.055	0.601	0.819
0.3	260	0.74	0.125	1.084	1.009
0.4	670	1.82	0.415	1.611	1.557

CHAPTER V

SUMMARY

In the overview of this research, the results can be summarized as follows.

Effect of BFCO doping on phase structure, microstructure, electric and magnetic properties of BNKLT ceramics prepared by the combustion method

$Bi_{0.5}(Na_{0.68}K_{0.22}Li_{0.10})_{0.5}TiO_3$-$xBi_2FeCrO_6$ (x=0, 0.004, 0.007, 0.013 and 0.019) solid solutions with a perovskite structure were prepared via the solid-state combustion technique. All samples showed the co-existence between the rhombohedral and tetragonal phases. The average grain size tended to increase with increasing BFCO content up to x=0.013 and then the grain size decreased. The highest density (5.87 g/cm^3), excellent dielectric constant (ε_R ~1390 and ε_m ~4986) and the highest piezoelectric constant (d_{33} ~ 194 pC/N) were obtained from the BNKLT-0.013BFCO ceramics because this sample has a MPB composition and exhibited good morphology. Without BFCO doping, the ceramic showed diamagnetic behavior whereas all of the BFCO doped ceramics showed paramagnetic behavior. These results suggested that the optimum BFCO doping content could improve the dielectric, piezoelectric and magnetic properties of BNKLT-xBFCO ceramics.

Phase formation, microstructure, electric and magnetic properties of multiferroic (1-x) $Bi_{0.5}(Na_{0.77}K_{0.20}Li_{0.03})_{0.5}TiO_3$-$xBi_{0.8}Ba_{0.2}FeO_3$ ceramics prepared via the solid-state combustion technique

(1-x)BNKLT-xBBF ceramics with x=0-0.4 were synthesized by the solid state combustion technique. All samples exhibited coexisting rhombohedral (R3c) and tetragonal (P4bm) phases. The ratio of the phase between R:T was about 58:41 which was obtained from the BNKLT ceramic. With increased x content, the percentage of the R phase decreased which was obtained from the Reitveld refinement. The average grain size and density continuously increased with increasing x. The dielectric constant at T_R tended to increase when x content increased up to 0.2 and then dropped. The remnant polarization (P_r) continuously decreased with increasing x. The coercive field (E_c) decreased as the BBF content increased up to 0.2 and then E_c

increased. For the magnetic properties, the BNKLT ceramics exhibited diamagnetic behavior. The 0.9BNKLT-0.1BBF ceramic exhibited paramagnetic behavior. (1-x)BNKLT-xBBF ceramics with x=0.2-0.4 showed ferromagnetic behavior, were the remnant magnetization (M_r) and coercive field (H_c) tended to increase as x content increased. 0.8BNKLT-0.2BBF ceramics exhibited a good morphology, excellent dielectric properties (ε_R=1746 and tan δ_R=0.0296), good ferroelectric properties (P_r=6.46 $\mu C/cm^2$ and E_c=11.84 kV/cm) and good ferromagnetic properties (M_r=0.002 emu/g and H_c=110 Oe).

Multiferroic properties of lead-free (1-x)($K_{0.44}Na_{0.52}Li_{0.04}$)($Nb_{0.84}Ta_{0.10}Sb_{0.06}$)$O_3$-x$Bi_{0.8}Ba_{0.2}FeO_3$ ceramics prepared via the solid-state combustion technique

The effect of BBF on the phase formation, microstructure, electrical and magnetic properties of (1-x)KNLNTS-xBBF ceramics with $0 \leq x \leq 0.4$ were fabricated by the solid state combustion technique were studied. The coexistence of the orthorhombic and tetragonal phases were observed in all samples. The enlargement of the unit cell volume and an increase in the tetragonal phase with increased x content was confirmed by the Rietveld refinement. The average grain size, density and relative density decreased with increased x up to 0.1 and then increased. T_{O-T} decreased with increased x while the T_C increased with increased x up to 0.1 and then it dropped. The dielectric constant at T_{O-T} and T_C tended to decrease with increased x content. The KNLNTS ceramic showed a well saturated P-E loop. For x=0.02-0.2, round P-E loop were observed due to the existence of a leakage current. With $x \geq 0.3$, the leakage current of the samples reduced, resulting in the samples exhibiting slim P-E loops. The KNLNTS ceramic showed diamagnetic behavior. For x=0.02-0.4, the M-H loops exhibited ferromagnetic behavior, and the magnetization was enhanced. Therefore, the binary multiferroic KNLNTS-BBF ceramics with x=0.3-0.4 can be a good candidate for many applications such as reading/writing with magnetization, spintronic, energy harvesting or sensors.

Electric and magnetic properties of $Bi_{0.80}Ba_{0.20}FeO_3$ doped $Ba_{0.85}Ca_{0.15}Ti_{0.90}Zr_{0.10}O_3$ ceramics prepared via the solid-state combustion technique

The phase, microstructure, electric and magnetic properties of lead free multiferroic $(1-x)Ba_{0.85}Ca_{0.15}Ti_{0.90}Zr_{0.10}O_3$-$xBi_{0.80}Ba_{0.20}FeO_3$ [(1-x)BCTZ-xBBF] ceramics, with x=0-0.4, were prepared via the solid-state combustion technique and investigated. A pure perovskite phase, with no secondary phase, was observed for the samples with x=0-0.3. At x=0.4, a secondary phase of $Bi_2Fe_4O_9$ was found. The ratio between the O and T phases of the BCTZ ceramic was 35.44:64.56. The T phase increased while the O phase decreased when x increased from 0 to 0.1, and then the T phase became 100% when $x \geq 0.2$, as verified by the Rietveld refinement analysis. The grain size, measured density and relative density continuously dropped when x increased. With increased x, the ε_R tended to decrease while tan δ_R tended to increase. Ferroelectric behavior decreased dramatically, and leakage currents were observed with x=0, 0.02 and 0.06-0.40, respectively. The addition BBF into the BCTZ matric induced oxygen vacancies, increased the Fe^{3+}-Fe^{3+} exchange interactions and caused structural distortions, which led to ferroelectricity and ferromagnetism coexisting.

In summary, the combination between ferroelectric and ferromagnetic materials can be produced the binary multiferroic material. In our work, the optimum content of BFCO and BBF could be observed in BNKLT-0.013BFCO, BNKLT-0.2BBF, KNLNTS-0.3BBF and BCTZ-0.1BBF ferroelectric ceramics which is effective way to improve the properties of these ceramics for various applications such as reading/writing with magnetization, spintronic, energy harvesting or sensors. The optimum content was found different x for each system, assumed that the different in chemical composition, phase formation, microstructure, and electrical property.

REFERENCES

1. Haertling G. Ferroelectric Ceramics: History and Technology. 2007. p. 157-78.
2. Jaffe H. Piezoelectric Ceramics. Journal of the American Ceramic Society. 1958;41(11):494-8.
3. Moulson AJ, Herbert JM. Electroceramics: Materials, Properties, Applications, 2nd Edition. England: John Wiley & Sons Ltd; 2003.
4. Smolensky GA, editor New ferroelectrics of complex composition. IV1961.
5. Bai W, Hao J, Fu F, Li W, Shen B, Zhai J. Structure and Strain Behavior of Textured BNT-Based Ceramics by Template Grain Growth. Materials Letters. 2013;97:137–40.
6. Wu J. Bi0.5Na0.5TiO3-Based Piezoelectric Materials. In: Wu J, editor. Advances in Lead-Free Piezoelectric Materials. Singapore: Springer Singapore; 2018. p. 191-245.
7. Xu Q, Chen X, Chen W, Chen S, Kim B-H, Lee J. Synthesis, Ferroelectric and Piezoelectric Properties of Some (Na0.5Bi0.5)TiO3 System Compositions. Materials Letters - MATER LETT. 2005;59:2437-41.
8. Sumang R, Cann D, Kumar N, Bongkarn T. Large strain in lead-free piezoelectric (1−x−y)Bi0.5Na0.5TiO3–xBi0.5K0.5TiO3–yBi0.5Li0.5TiO3 system near MPB prepared via the combustion technique. Ceramics International. 2015;41.
9. Wang X, Wu J, Xiao D, Cheng X, Zheng T, Lou X, et al. New Potassium–Sodium Niobate Ceramics with a Giant d33. ACS Applied Materials & Interfaces. 2014;6(9):6177-80.
10. Li J-F, Wang K, Zhu F-Y, Cheng L-Q, Fang-Zhou Y. (K,Na)NbO3-Based Lead-Free Piezoceramics: Fundamental Aspects, Processing Technologies, and Remaining Challenges. Journal of the American Ceramic Society. 2013;92(12):3677-96.
11. Xiao DQ, Wu JG, Wu L, Zhu JG, Yu P, Lin DM, et al. Investigation on the composition design and properties study of perovskite lead-free piezoelectric ceramics. Journal of Materials Science. 2009;44(19):5408-19.
12. Mathrmool K, Udeye T, Bongkarn T. Low temperature fabrication of lead-free piezoelectric KNLNTS ceramics by the solid state combustion technique. Ferroelectrics. 2017;518:31-41.
13. Zhang S, Zhang H, B.-P. Zhang Z, Yang S. Phase-transition behavior and piezoelectric properties of lead-free (Ba0.95Ca0.05)(Ti1−xZrx)O3 ceramics. Journal of Alloys and Compounds. 2010;506:131-5.
14. Kalyani A, Brajesh K, Senyshyn A, Ranjan R. Orthorhombic-tetragonal phase coexistence and enhanced piezo-response at room temperature in Zr, Sn, and Hf modified BaTiO3. Applied Physics Letters. 2014;104:252906-.
15. Liu W, Ren X. Large Piezoelectric Effect in Pb-Free Ceramics. Physical Review Letters. 2009;103(25):257602.
16. Kornphom C, Vittayakorn N, Bongkarn T. Low Firing Temperatures and High Ferroelectric Properties of (Ba0.85Ca0.15)(Ti0.90Zr0.10)O3 Lead-Free Ceramics Synthesized by the Combustion Technique. Ferroelectrics. 2016;491:44-53.
17. Dai Z, Liu L, Ying G, Yuan M, Ren X. Structural, dielectric and magnetic properties of Mn modified xBiFeO3-(1-x)BaTiO3 Ceramics. Journal of Magnetism and Magnetic Materials. 2016;434.
18. Hu M, Su R, Wang C. Tailoring the multiferroic properties in

Ba0.85Ca0.15Zr0.1Ti0.9O3/La0.7Sr0.3MnO3 bilayer heterostructures using residual strain. Journal of Materials Science: Materials in Electronics. 2021;32(21):26049-58.
19. Hill NA. Why Are There so Few Magnetic Ferroelectrics? The Journal of Physical Chemistry B. 2000;104(29):6694-709.
20. Fischer P, Polomska M, Sosnowska I, Szymanski M. Temperature dependence of the crystal and magnetic structures of BiFeO₃. Journal of Physics C: Solid State Physics. 1980;13(10):1931-40.
21. Pradhan AK, Zhang K, Hunter D, Dadson JB, Loiutts GB, Bhattacharya P, et al. Magnetic and electrical properties of single-phase multiferroic BiFeO3. Journal of Applied Physics. 2005;97(9):093903.
22. Wang YP, Zhou L, Zhang MF, Chen XY, Liu JM, Liu ZG. Room-temperature saturated ferroelectric polarization in BiFeO3 ceramics synthesized by rapid liquid phase sintering. Applied Physics Letters. 2004;84(10):1731-3.
23. Kumar MM, Palkar VR, Srinivas K, Suryanarayana SV. Ferroelectricity in a pure BiFeO3 ceramic. Applied Physics Letters. 2000;76(19):2764-6.
24. Anjum G, Kumar R, Mollah S, Shukla DK, Kumar S, Lee CG. Structural, dielectric, and magnetic properties of La0.8Bi0.2Fe1−xMnxO3 (0.0≤x≤0.4) multiferroics. Journal of Applied Physics. 2010;107(10):103916.
25. Khomchenko VA, Kiselev DA, Vieira JM, Jian L, Kholkin AL, Lopes AML, et al. Effect of diamagnetic Ca, Sr, Pb, and Ba substitution on the crystal structure and multiferroic properties of the BiFeO3 perovskite. Journal of Applied Physics. 2008;103(2):024105.
26. Khomchenko VA, Kiselev DA, Bdikin IK, Shvartsman VV, Borisov P, Kleemann W, et al. Crystal structure and multiferroic properties of Gd-substituted BiFeO3. Applied Physics Letters. 2008;93(26):262905.
27. Yang C, Jiang J-S, Qian F-Z, Jiang D-M, Wang C-M, Zhang W-G. Effect of Ba doping on magnetic and dielectric properties of nanocrystalline BiFeO3 at room temperature. Journal of Alloys and Compounds. 2010;507(1):29-32.
28. Nechache R, Rosei F. Recent progress in nanostructured multiferroic Bi2FeCrO6 thin films. Journal of Solid State Chemistry. 2012;189:13-20.
29. Ryu KH, Song TK, Kim MH, Lee SH, Seong YS, Jeong SJ, et al. EFFECT OF BiFeO3 DOPING ON FERROELECTRIC AND PIEZOELECTRIC PROPERTIES OF (Bi0.5Na0.5)TiO3 AND BaTiO3 CERAMICS. Integrated Ferroelectrics. 2006;84(1):31-8.
30. Wei Y, Wang X, Jia J, Wang X. Multiferroic and Piezoelectric Properties of 0.65BiFeO3–0.35BaTiO3 Ceramic With Pseudo-Cubic Symmetry. Ceramics International. 2012;38:3499-502.
31. Yi J, Tian Y, Wei L, Li J, Liang P, Shi P, et al. Structure, dielectric, ferroelectric, and magnetic properties of (1 - X) BiFeO3-x (Ba0.85Ca0.15)(Zr0.10Ti0.90)O3 ceramics. Materials Research Bulletin. 2015;66.
32. Kaswan K, Agarwal A, Sanghi S, Kotnala RK. Crystal structure refinement and magnetic properties of Bi0.8Ba0.2FeO3 substituted Na0.5Bi0.5TiO3 ceramics. Journal of Molecular Structure. 2016;1108:54-9.
33. Kaswan K, Agarwal A, Sanghi S, Rangi M, Jangra S, Kumar A. Crystal structure refinement, enhanced magnetic and dielectric properties of Na0.5Bi0.5TiO3 modified Bi0.8Ba0.2FeO3 ceramics. Ceramics International. 2017;43(5):4622-9.
34. Waser R. Nanoelectronics and Information Technology: Advanced Electronic

Materials and Novel Devices. Weinheim: Wiley-VCH, Verlag GmbH and Co. KGaA; 2003.
35. Kittel C. Introduction to Solid State Physics, 8th Edition: John Wiley and Sons, Inc.; 2004.
36. Olaf Müller, Roy R. The Major ternary structural families. Berlin ; Heidelberg ; New York: Springer-Verlag; 1974.
37. Acosta M. Strain Mechanisms in Lead-Free Ferroelectrics for Actuators. Switzerland Springer, Cham; 2015.
38. Känzig W. Ferroelectrics and Antiferroeletrics. In: Seitz F, Turnbull D, editors. Solid State Physics. 4: Academic Press; 1957. p. 1-197.
39. Kwei GH, Lawson AC, Billinge SJL, Cheong SW. Structures of the ferroelectric phases of barium titanate. The Journal of Physical Chemistry. 1993;97(10):2368-77.
40. Damjanovic D. Ferroelectric, dielectric and piezoelectric properties of ferroelectric thin films and ceramics. Reports on Progress in Physics. 1998;61(9):1267-324.
41. Kittel C. Introduction to Solid State Physics. American Journal of Physics. 1967;35(6):547-8.
42. Wikipedia. Diamagnetism. [Internet]. [cited 2021 Nov 20]. 2017 [Available from: https://en.wikipedia.org/wiki/Diamagnetism
43. The Editors of Encyclopaedia Britannica See Article History. [Internet]. [cited 2021 Nov 20]. [Available from: https://www.britannica.com/science/paramagnetism
44. Classes of Magnetic Materials. [Internet]. [cited 2021 Nov 20]. [Available from: http://www.irm.umn.edu/hg2m/hg2m_b/hg2m_b.html
45. Wikipedia. (2017). Ferromagnetism. [Internet]. [cited 2021 Nov 20]. [Available from: https://en.wikipedia.org/wiki/Ferromagnetism
46. Wikipedia. (2017). Antiferromagnetism. [Internet]. [cited 2021 Nov 20]. [Available from: https://en.wikipedia.org/wiki/Antiferromagnetism.
47. Wikipedia. (2017). Ferrimagnetism. [Internet]. [cited 2021 Nov 20]. [Available from: https://en.wikipedia.org/wiki/Ferrimagnetism
48. Cheong S-W, Mostovoy M. Multiferroics: a magnetic twist for ferroelectricity. Nature Materials. 2007;6(1):13-20.
49. West AR, Sinclair DC, Hirose N. Characterization of Electrical Materials, Especially Ferroelectrics, by Impedance Spectroscopy. Journal of Electroceramics. 1997;1(1):65-71.
50. Irvine JTS, Sinclair DC, West AR. Electroceramics: Characterization by Impedance Spectroscopy. Advanced Materials. 1990;2(3):132-8.
51. Wul BM, Golman IM. Dielectric Constants of Titanates of Metals of the Second Group. Dokl Akad Nauk SSSR. 1945;46:154-7.
52. Barsoum MW. Fundamentals of Ceramics. Boca Raton: Taylor & Francis 2002.
53. Fernández-García M, Martínez-Arias A, Hanson JC, Rodriguez JA. Nanostructured Oxides in Chemistry: Characterization and Properties. Chemical Reviews. 2004;104(9):4063-104.
54. Kolen'ko YV, Kovnir KA, Gavrilov AI, Garshev AV, Meskin PE, Churagulov BR, et al. Structural, textural, and electronic properties of a nanosized mesoporous ZnxTi1-xO2-) solid solution prepared by a supercritical drying route. Journal of Physical Chemistry B. 2005;109(43):20303-9.
55. Pierre AC. Introduction to Sol-Gel Processing: Springer, Boston, MA; 1998.

56. Livage J, Sanchez C. Sol-gel chemistry. Journal of Non-Crystalline Solids. 1992;145:11-9.
57. Judeinstein P, Sanchez C. Hybrid organic–inorganic materials: a land of multidisciplinarity. Journal of Materials Chemistry. 1996;6(4):511-25.
58. Carp O, Huisman CL, Reller A. Photoinduced reactivity of titanium dioxide. Progress in Solid State Chemistry. 2004;32(1):33-177.
59. Pampuch R. Advanced HT ceramic materials via solid combustion Journal of the European Ceramic Society. 1999;19:2395-404.
60. Varma A, Rogachev AS, Mukasyan AS, Hwang S. Combustion Synthesis of Advanced Materials: Principles and Applications. In: Wei J, editor. Advances in Chemical Engineering. 24: Academic Press; 1998. p. 79-226.
61. Patil KC, Aruna ST, Mimani T. Combustion synthesis: an update. Current Opinion in Solid State and Materials Science. 2002;6(6):507-12.
62. Wang XX, Tang XG, Kwok KW, Chan HLW, Choy CL. Effect of excess Bi2O3 on the electrical properties and microstructure of (Bi1/2Na1/2)TiO3 ceramics. Applied Physics A. 2005;80(5):1071-5.
63. Kainz T, Naderer M, Schütz D, Fruhwirth O, Mautner FA, Reichmann K. Solid state synthesis and sintering of solid solutions of BNT–xBKT. Journal of the European Ceramic Society. 2014;34(15):3685-97.
64. Singh A, Chatterjee R. Structural and electrical properties of BKT rich Bi0.5K0.5TiO3-K0.5Na0.5NbO3 system. AIP Advances. 2013;3(3):032129.
65. Li W, Xu Z, Chu R, Fu P, Zang G. High piezoelectric d33 coefficient in (Ba1−xCax)(Ti0.98Zr0.02)O3 lead-free ceramics with relative high Curie temperature. Materials Letters. 2010;64:2325–7.
66. Rödel J, Webber KG, Dittmer R, Jo W, Kimura M, Damjanovic D. Transferring lead-free piezoelectric ceramics into application. Journal of the European Ceramic Society. 2015;35(6):1659-81.
67. Wu J, Xiao D, Zhu J. Potassium–Sodium Niobate Lead-Free Piezoelectric Materials: Past, Present, and Future of Phase Boundaries. Chemical Reviews. 2015;115(7):2559-95.
68. Zheng T, Wu J, Xiao D, Zhu J. Recent development in lead-free perovskite piezoelectric bulk materials. Progress in Materials Science. 2018;98:552-624.
69. Buhrer CF. Some Properties of Bismuth Perovskites. The Journal of Chemical Physics. 1962;36(3):798-803.
70. Hiruma Y, Nagata H, Takenaka T. Thermal depoling process and piezoelectric properties of bismuth sodium titanate ceramics. Journal of Applied Physics. 2009;105(8):084112.
71. Lee W-C, Huang C-Y, Tsao L-K, Wu Y-C. Chemical composition and tolerance factor at the morphotropic phase boundary in (Bi0.5Na0.5)TiO3-based piezoelectric ceramics. Journal of the European Ceramic Society. 2009;29(8):1443-8.
72. Suzuki M, Akedo J. Polarization and leakage current properties of bismuth sodium titanate ceramic films deposited by aerosol deposition method. Journal of the Ceramic Society of Japan. 2013;121:664-9.
73. Hiruma Y, Yoshii K, Nagata H, Takenaka T. Phase transition temperature and electrical properties of (Bi1/2Na1/2)TiO3-(Bi1/2A1/2)TiO3 (A=Li and K) lead-free ferroelectric ceramics. Journal of Applied Physics. 2008;103:084121-.
74. Chu B-J, Chen D-R, Li G-R, Yin Q-R. Electrical properties of Na1/2Bi1/2TiO3–

BaTiO3 ceramics. Journal of the European Ceramic Society. 2002;22(13):2115-21.
75. Jones G, Kreisel J, Jennings V, Geday M, Thomas P, Glazer M. Investigation of a Peculiar Relaxor Ferroelectric: Na0.5Bi0.5TiO3. Ferroelectrics. 2002;270.
76. Jones G, Thomas P. Investigation of the Structure and Phase Transition in the Novel A-Site Substituted Distorted Perovskite Compound Na1/2Bi1/2TiO3. Acta Crystallographica Section B-structural Science - ACTA CRYSTALLOGR B-STRUCT SCI. 2002;58:168-78.
77. Rao P, Sankaram T. Impedance spectroscopy studies of K0.5Bi0.5TiO3. Journal of Electroceramics. 2010;25:60-9.
78. Isupov VA. Ferroelectric Na0.5Bi0.5TiO3 and K0.5Bi0.5TiO3 Perovskites and Their Solid Solutions. Ferroelectrics. 2005;315(1):123-47.
79. Hou Y, Zhu M, Hou L, Liu J, Tang J, Wang H, et al. Synthesis and characterization of lead-free K0.5Bi0.5TiO3 ferroelectrics by sol–gel technique. Journal of Crystal Growth. 2005;273(3):500-3.
80. Lencka MM, Oledzka M, Riman RE. Hydrothermal Synthesis of Sodium and Potassium Bismuth Titanates. Chemistry of Materials. 2000;12(5):1323-30.
81. Zhao S, Li G, Ding A, Wang T, Yin Q. Ferroelectric and Piezoelectric Properties of (Na, K)0.5Bi0.5TiO3 Lead Free Ceramics. Journal of Physics D: Applied Physics. 2006;39:2277.
82. Yang J, Hou Y, Wang C, Zhu M, Yan H. Relaxor behavior of (K0.5Bi0.5)TiO3 ceramics derived from molten salt synthesized single-crystalline nanowires. Applied Physics Letters. 2007;91(2):023118.
83. Hiruma Y, Marumo K, Aoyagi R, Nagata H, Takenaka T. Ferroelectric and piezoelectric properties of (Bi1/2K1/2)TiO3 ceramics fabricated by hot-pressing method. Journal of Electroceramics. 2008;21(1):296-9.
84. Yang Z, Liu B, Wei L, Hou Y. Structure and electrical properties of (1−x)Bi0.5Na0.5TiO3–xBi0.5K0.5TiO3 ceramics near morphotropic phase boundary. Materials Research Bulletin. 2008;43(1):81-9.
85. Yang Z, Hou Y, Pan H, Chang Y. Structure, microstructure and electrical properties of (1−x−y)Bi0.5Na0.5TiO3–xBi0.5K0.5TiO3–yBi0.5Li0.5TiO3 lead-free piezoelectric ceramics. Journal of Alloys and Compounds. 2009;480(2):246-53.
86. Wang K, Li J-F. Analysis of crystallographic evolution in (Na,K)NbO3-based lead-free piezoceramics by x-ray diffraction. Applied Physics Letters. 2007;91(26):262902.
87. Guo Y, Kakimoto K-i, Ohsato H. (Na0.5K0.5)NbO3–LiTaO3 lead-free piezoelectric ceramics. Materials Letters. 2005;59:241-4.
88. Saito Y, Takao H, Tani T, Nonoyama T, Takatori K, Homma T, et al. Lead-free piezoceramics. Nature. 2004;432(7013):84-7.
89. Saito Y, Takao H. High Performance Lead-free Piezoelectric Ceramics in the (K,Na)NbO3-LiTaO3 Solid Solution System. Ferroelectrics. 2006;338:17-32.
90. Jiang M, Liu X, Liu C. Effect of BiFeO3 additions on the dielectric and piezoelectric properties of (K0.44Na0.52Li0.04)(Nb0.84Ta0.1Sb0.06)O3 ceramics. Materials Research Bulletin. 2010;45(2):220-3.
91. Jain TA, Fung KZ, Chan J. Effect of the A/B ratio on the microstructures and electrical properties of (Ba0.95±xCa0.05)(Ti0.82Zr0.18)O3 for multilayer ceramic capacitors with nickel electrodes. Journal of Alloys and Compounds. 2009;468(1):370-4.

92. Hennings D, Schreinemacher H. Temperature dependence of the segregation of calcium titanate from solid solutions of (Ba, Ca) (Ti, Zr)O3 and its effect on the dielectric properties. Materials Research Bulletin. 1977;12(12):1221-6.
93. Wang P, Li Y, Lu Y. Enhanced Piezoelectric Properties of (Ba0.85Ca0.15)(Ti0.9Zr0.1)O-3 Lead-Free Ceramics by Optimizing Calcination and Sintering Temperature. Journal of The European Ceramic Society - J EUR CERAM SOC. 2011;31:2005-12.
94. Kubel F, Schmid H. Structure of a ferroelectric and ferroelastic monodomain crystal of the perovskite BiFeO3. Acta Crystallographica Section B. 1990;46(6):698-702.
95. Moreau JM, Michel C, Gerson R, James WJ. Ferroelectric BiFeO3 X-ray and neutron diffraction study. Journal of Physics and Chemistry of Solids. 1971;32(6):1315-20.
96. Catalan G, Scott JF. Physics and Applications of Bismuth Ferrite. Advanced Materials. 2009;21(24):2463-85.
97. Shannon RD. Revised effective ionic radii and systematic studies of interatomic distances in halides and chalcogenides. Acta Crystallographica Section A. 1976;32(5):751-67.
98. Dai J-Q, Xu J-W, Zhu J-H. First-principles study on the multiferroic BiFeO3 (0001) polar surfaces. Applied Surface Science. 2016;392.
99. Shvartsman V, Kleemann W, Haumont R, Kreisel J. Large Bulk Polarization and Regular Domain Structure in Ceramic BiFeO3. Applied Physics Letters. 2007;90:172115-.
100. Palkar VR, John J, Pinto R. Observation of saturated polarization and dielectric anomaly in magnetoelectric BiFeO3 thin films. Applied Physics Letters. 2002;80(9):1628-30.
101. Cheng R, Xu Z, Chu R, Hao J, Du J, Ji W, et al. Large piezoelectric effect in Bi1/2Na1/2TiO3-based lead-free piezoceramics. Ceramics International. 2015;41(6):8119-27.
102. Thawong P, Prasertpalichat S, Suriwong T, Pinitsoontorn S, McQuade R, Gupta S, et al. Phase formation, microstructure, electrical and magnetic properties of 0.94Bi0.50Na0.50TiO3–0.06Ba0.85Ca0.15Ti0.90Zr0.10O3 ceramics doped with Bi2FeCrO6 prepared via solid-state combustion technique. Journal of Materials Science. 2020;55.
103. Yotthuan S, Suriwong T, Pinitsoontorn S, Bongkarn T. Effect of Fe 2 O 3 doping on phase formation, microstructure, electric and magnetic properties of (Ba 0.85 Ca 0.15)(Ti 0.90 Zr 0.10)O 3 ceramics. Integrated Ferroelectrics. 2018;187:100-12.
104. Cheng R, Xu Z, Chu R, Hao J, Du J, Li G. Electric field-induced ultrahigh strain and large piezoelectric effect in Bi1/2Na1/2TiO3-based lead-free piezoceramics. Journal of the European Ceramic Society. 2016;36(3):489-96.
105. Li Y, Wang F, Ye X, Xie Y, Tang Y, Sun D, et al. Large Strain Response and Fatigue-Resistant Behavior in Ternary Bi0.5Na0.5TiO3–BaTiO3–Bi(Zn0.5Ti0.5)O3 Solid Solutions. Journal of the American Ceramic Society. 2014;97.
106. Bai W, Li L, Li W, Shen B, Zhai J, Chen H. Phase Diagrams and Electromechanical Strains in Lead-Free BNT-Based Ternary Perovskite Compounds. Journal of the American Ceramic Society. 2014;97(11):3510-8.
107. Viola G, McKinnon R, Koval V, Adomkevicius A, Dunn S, Yan H. Lithium-

Induced Phase Transitions in Lead-Free Bi0.5Na0.5TiO3 Based Ceramics. The Journal of Physical Chemistry C. 2014;118(16):8564-70.
108. Jo W, Schaab S, Sapper E, Schmitt LA, Kleebe H-J, Bell AJ, et al. On the phase identity and its thermal evolution of lead free (Bi1/2Na1/2)TiO3-6 mol% BaTiO3. Journal of Applied Physics. 2011;110(7):074106.
109. Bongkarn T, Chootin S, Pinitsoontorn S, Maensiri S. Excellent piezoelectric and ferroelectric properties of KNLNTS ceramics with Fe2O3 doping synthesized by the solid state combustion technique. Journal of Alloys and Compounds. 2016;682:14-21.
110. Qiu S-y, Li W, Liu Y, Liu G-h, Wu Y-q, Chen N. Phase evolution and room temperature ferroelectric and magnetic properties of Fe-doped BaTiO3 ceramics. Transactions of Nonferrous Metals Society of China. 2010;20(10):1911-5.
111. Jones G, Kreisel J, Thomas P. A structural study of the (Na1−xKx)0.5Bi0.5TiO3 perovskite series as a function of substitution (x) and temperature. Powder Diffraction. 2002;17.
112. Clemens O, Kruk R, Patterson EA, Loho C, Reitz C, Wright AJ, et al. Introducing a Large Polar Tetragonal Distortion into Ba-Doped BiFeO3 by Low-Temperature Fluorination. Inorganic Chemistry. 2014;53(23):12572-83.
113. Shariq M, Hussain S, Rafique M, Naveed-Ul-Haq M, Rahman A. Enhanced multiferroic response in new binary solid solution (0.5)Bi0.70A0.30FeO3–(0.5)PbTi0.5Fe0.5O3 (A = Sr, Pb, and Ba) systems. Journal of Magnetism and Magnetic Materials. 2019;492:165685.
114. Schmitt L, Hinterstein M, Kleebe H-J, Fuess H. Comparative Study of Two Lead-Free Piezoceramics Using Diffraction Techniques. Journal of Applied Crystallography - J APPL CRYST. 2010;43:805-10.
115. Dorcet V, Trolliard G. A transmission electron microscopy study of the A-site disordered perovskite Na0.5Bi0.5TiO3. Acta Materialia. 2008;56(8):1753-61.
116. Zhang H, Zhou J, Shen Ji, Yang X, Wu C, Han K, et al. Enhanced piezoelectric property and promoted depolarization temperature in Fe doped Bi-1/2(Na0.8K0.2)(1/2)TiO3 lead-free ceramics. Ceramics International. 2017:16395-402.
117. Hao J, Xu Z, Chu R, Li W, Du J, Fu P. Large strain response and fatigue-resistant behavior in lead-free Bi0.5(Na0.80K0.20)0.5TiO3-(K0.5Na0.5)MO3 (M = Sb, Ta) ceramics. RSC Advances. 2015;5:82605-16.
118. Bai W, Li L, Li We, Shen Bo, Zhai J, Chen H. Phase Diagrams and Electromechanical Strains in Lead-Free BNT-Based Ternary Perovskite Compounds. Journal of the American Ceramic Society. 2014:3510-8.
119. Ni F, Luo L, Li W, Chen H. A-Site Vacancy-Induced Giant Strain and the Electrical Properties in Non-Stoichiometric Ceramics Bi0.5+x(Na1−yKy)0.5−3xTiO3. Journal of Physics D: Applied Physics. 2012;45:415103.
120. Hao J, Bai W, Li W, Shen B, Zhai J. Phase transitions, relaxor behavior, and large strain response in LiNbO3-modified Bi0.5(Na0.80K0.20)0.5TiO3 lead-free piezoceramics. Journal of Applied Physics. 2013;114.
121. Zerihun G, Huang S, Gong G, Yuan S. Influence of Eu doping on the magnetoelectric and dielectric properties of BiFeO3–Bi0.5Na0.5TiO3 ceramics. Ceramics International. 2015;41(5, Part A):6589-95.
122. Hussain A, Zheng P, Xu X, Chen X, Li T, Wang Y, et al. Structural and electrical properties of multiferroic (1−x)BiFeO3−xBi0.5K0.5TiO3 ceramics. Journal of Alloys and Compounds. 2016;678:228-33.

123. Cheng S, Zhang B-P, Zhao L, Wang K-K. Enhanced insulating and piezoelectric properties of BiFeO3-BaTiO3-Bi0.5Na0.5TiO3 ceramics with high Curie temperature. Journal of the American Ceramic Society. 2019;102(12):7355-65.
124. Koduri R, Orellana J. Dielectric and piezoelectric characterization of PSZT BT ceramics for capacitor applications. Journal of Materials Science: Materials in Electronics. 2008;19:373-8.
125. Bhupaijit P, Kornphom C, Vittayakorn N, Bongkarn T. Structural, microstructure and electrical properties of La2O3-doped Bi0.5(Na0.68K0.22Li0.1)0.5TiO3 lead-free piezoelectric ceramics synthesized by the combustion technique. Ceramics International. 2015;41.
126. Wu MS, Tian Z, Yuan SL, Duan HN, Qiu Y. Dielectric behavior and ac conductivity in Aurivillius Bi4Ti3O12 doped by antiferromagnetic BiFeO3. Physics Letters A. 2012;376:2062–6.
127. Li C-X, Yang B, Zhang S-T, Zhang R, Sun Y, Zhang H-J, et al. Enhanced Multiferroic and Magnetocapacitive Properties of (1 − x)Ba0.7Ca0.3TiO3–xBiFeO3 Ceramics. Journal of the American Ceramic Society. 2014;97(3):816-25.
128. Li C-X, Yang B, Zhang S-T, Liu D-Q, Zhang R, Sun Y, et al. Effects of Mn doping on multiferroic and magnetocapacitive properties of 0.33Ba0.70Ca0.30TiO3–0.67BiFeO3 diphasic ceramics. Journal of Alloys and Compounds. 2014;590:346-54.
129. Wang L, Wang X, Shi J. Measurement and Estimation of Ferroelectric Hysteresis Loops. Ferroelectrics. 2010;411(1):86-92.
130. Qiu S-y, Li W, Liu Y, Liu G-h, Wu Y-q, Chen N. Phase Evolution and Room Temperature Ferroelectric and Magnetic Properties of Fe-Doped BaTiO3 Ceramics. Transactions of Nonferrous Metals Society of China. 2010;20:1911-5.
131. Guo R, Fang L, Dong W, Zheng F, Shen M. Enhanced Photocatalytic Activity and Ferromagnetism in Gd Doped BiFeO3 Nanoparticles. The Journal of Physical Chemistry C. 2010;114(49):21390-6.
132. L. Katz, Megaw HD. The structure of potassium niobate at room temperature: the solution of a pseudosymmetric structure by Fourier methods. Acta Crystallographica Section A. 1967;22:639-48.
133. Hewat AW. Cubic-tetragonal-orthorhombic-rhombohedral ferroelectric transitions in perovskite potassium niobate: neutron powder profile refinement of the structures. Journal of Physics C: Solid State Physics. 1973;6(16):2559-72.
134. Sindhu M, Ahlawat N, Sanghi S, Kumari R, Agarwal A. Effect of Zr substitution on phase transformation and dielectric properties of Ba0.9Ca0.1TiO3 ceramics. Journal of Applied Physics. 2013;114(16):164106.
135. Wagner A. Zur Theorie der Unvollkommenen Dielektrika. Annalen der Physik. 1913;40:817-55.
136. Guo Y, Kakimoto K-i, Ohsato H. Phase transitional behavior and piezoelectric properties of (Na0.5K0.5)NbO3–LiNbO3 ceramics. Applied Physics Letters. 2004;85(18):4121-3.
137. Matsubara M, Kikuta K, Hirano S. Piezoelectric properties of (K0.5Na0.5)(Nb1−xTax)O3−K5.4CuTa10O29 ceramics. Journal of Applied Physics. 2005;97(11):114105.
138. Matsubara M, Yamaguchi T, Sakamoto W, Kikuta K, Yogo T, Hirano S-i. Processing and Piezoelectric Properties of Lead-Free (K,Na) (Nb,Ta) O3 Ceramics. Journal of the American Ceramic Society. 2005;88(5):1190-6.

139. Cheng GY, Fu XH, Jin X, Tao WH, Qiang YQ. KNN-BF Lead-Free Piezoelectric Ceramics Synthesized by Sol-Gel Method. Applied Mechanics and Materials. 2015;740:3-6.
140. Wu X, Tian M, Guo Y, Zheng Q, Luo L, Lin D. Phase transition, dielectric, ferroelectric and ferromagnetic properties of La-doped BiFeO3–BaTiO3 multiferroic ceramics. Journal of Materials Science: Materials in Electronics. 2014;26:978-84.
141. Arora M, Kumar M. Structural, magnetic and optical properties of Ce substituted BiFeO3 nanoparticles. Ceramics International. 2015;41(4):5705-12.
142. Miyake S, Ueda R. On Phase Transformation of BaTiO₃. Journal of the Physical Society of Japan. 1947;2(5):93-7.
143. Al-Shakarchi EK, Mahmood NB. Three Techniques Used to Produce BaTiO3 Fine Powder. Journal of Modern Physics. 2011;2:1420-8.
144. Lu DY, Yue Y, Sun XY. Novel X7R BaTiO3 ceramics co-doped with La3+ and Ca2+ ions. Journal of Alloys and Compounds. 2014;586:136-41.
145. Yang F, Wu P, Sinclair DC. Enhanced bulk conductivity of A-site divalent acceptor-doped non-stoichiometric sodium bismuth titanate. Solid State Ionics. 2017;299:38-45.
146. Wodecka-Dus B, Goryczka T, Adamczyk-Habrajska M, Bara M, Dzik J, Szalbot D. Dielectric and Electrical Properties of BLT Ceramics Modified by Fe Ions. Materials. 2020;13(24).
147. Fan H, Liu L. Microstructure and electrical properties of the rare-earth doped 0.94Na0.5Bi0.5TiO3-0.06BaTiO3 piezoelectric ceramics. Journal of Electroceramics. 2008;21(1):300-4.
148. Ma J, Liu X, Li W. High Piezoelectric Coefficient and Temperature Stability of Ga2O3-Doped (Ba0.99Ca0.01)(Zr0.02Ti0.98)O3 Lead-Free Ceramics by Low-Temperature Sintering. Journal of Alloys and Compounds. 2013;581:642-5.
149. Idrees M, Nadeem M, Mehmood M, Atif M, Chae KH, Hassan MM. Impedance spectroscopic investigation of delocalization effects of disorder induced by Ni doping in LaFeO₃. Journal of Physics D: Applied Physics. 2011;44(10):105401.
150. Makhdoom AR, Akhtar MJ, Rafiq MA, Hassan MM. Investigation of transport behavior in Ba doped BiFeO3. Ceramics International. 2012;38(5):3829-34.
151. Selbach SM, Tybell T, Einarsrud M-A, Grande T. Structure and Properties of Multiferroic Oxygen Hyperstoichiometric BiFe1−xMnxO3+δ. Chemistry of Materials. 2009;21(21):5176-86.
152. Dorcet V, Marchet P, Peña O, Trolliard G. Properties of the solid solution (1−x)Na0.5Bi0.5TiO3–(x)BiFeO3. Journal of Magnetism and Magnetic Materials. 2009;321(11):1762-6.
153. Katlakunta S, Raju P, Meena SS, Srinath S, Sandhya R, Kuruva P, et al. Multiferroic properties of microwave sintered BaTiO3–SrFe12O19 composites. Physica B: Condensed Matter. 2014;448:323-6.